A COMPREHENSIVE ANALYSIS OF THE EVOLUTION OF

COASTAL FLOODING IN TEXAS AND LOUISIANA

FOR APPLICATION IN RISK ASSESSMENT

A Dissertation

Presented to the Faculty of the Graduate School of

The University of Texas at Arlington in Partial Fulfillment

of the Requirements for the Degree of

Doctor of Philosophy

by

Joshua A. Pulcinella

University of Texas at Arlington

Department of Earth and Environmental Science

December, 2022

Acknowledgments

Abstract
A COMPREHENSIVE ANALYSIS OF THE EVOLUTION OF

COASTAL FLOODING IN TEXAS AND LOUISIANA

FOR APPLICATION IN RISK ASSESSMENT

Joshua Pulcinella

University of Texas at Arlington, 2022

Supervising Professor: Dr. Arne Winguth

Coastal communities of the northern Gulf of Mexico have historically been at risk of flooding from tropical cyclone induced storm surge and extreme precipitation. Relative sea level rise resulting from a combination of increasing global mean sea level and regional subsidence presents an escalating threat that requires a comprehensive assessment of changing flood risks for the area. This study examines how coastal flooding events are changing and focuses on the future risks to communities and infrastructure in Texas and Louisiana. Utilizing historic tide gauge observations, tropical cyclone records, and associated storm tide data, the frequency, duration, and magnitude of events exceeding existing flood threshold levels are quantified, return periods estimated, correlations with climate oscillations tested, and trends analyzed.

To assess forecasting relative sea level rise, a seasonal autoregressive integrated moving average (SARIMA) model based on raw tide gauge observations is compared to probabilistic projections based on background subsidence rates, global climate models and anthropogenic emissions scenarios. Projections are utilized to map inundation under a range of future scenarios for mean high tide and added to SLOSH storm surge model output under current sea level to map future storm tide inundation under multiple hurricane categories. Probabilistic projections appear to be more suitable for use in risk assessments than SARIMA modeling as they forecast a range of possible sea level rise acceleration scenarios that address the uncertainties inherent in the climate system, climate models, and anthropogenic emissions, while SARIMA lacks the ability to model acceleration.

Inundation mapping using probabilistic scenarios revealed the impacts from relative sea level on mean high tide flooding risk will be seen in the lowest elevations as early as 2040 under all scenarios and the addition of sea level rise to modeled storm surge increases the area of inundation farther inland effecting populations and infrastructure not previously threatened. Additionally, non-tidal residuals associated with storms were found to be the primary influence on flood threshold exceedance over the last 40 years. Estimated peak surge return periods based on 30-year averages from 1900-2020 suggest an increase to the 100-year peak surge of ~2.5 meters. This study found relative sea level rise, rather than changes in tropical cyclone climatology or climate oscillations, is the key factor contributing to more frequent, longer lasting, and greater magnitude coastal flooding events observed in the record and will continue to present an increasing risk as global temperature rises. Moreover, relative sea level rise is increasing the probability of high tide, or nuisance, flooding not associated with storms and impacts that were historically rare are becoming more common and lasting longer, particularly at locations with higher tidal ranges.

Results suggest that coastal flood risk assessments can be improved to include the enhanced risks associated with accelerating relative sea level rise rather than relying on historic observations. These improvements include using localized sea level projections that reflect varying subsidence rates, estimating future surge return periods based on observed changes, accounting for previously rare events such as high tide flooding and inland storm surge inundation, and recognizing social vulnerability as an additional risk.

Table of Contents

List of Figures

List of Tables

List of Abbreviations

ACF	Autocorrelation Function
ADCIRC	Advanced Circulation Model
AHPS	Advanced Hydrological Prediction Systems
AIC	Akaike Information Criterion
AMO	Atlantic Multidecadal Oscillation
AR5	Fifth Assessment Report of the Intergovernmental Panel on Climate Change
AR6	Sixth Assessment Report of the Intergovernmental Panel on Climate Change
ARIMA	Autoregressive Integrated Moving Average
BIC	Bayesian Information Criterion
CDC	Centers for Disease Control and Prevention
CESM3	Community Earth System Model Phase 3
CMIP5	Coupled Model Intercomparison Project Phase 5
CMIP6	Coupled Model Intercomparison Project Phase 6
CTEDD	Center for Transportation Equity, Decisions and Dollars
CVI	Coastal Vulnerability Index
DEM	Digital Elevation Model
ENSO	El Niño Southern Oscillation
ESM	Exponential Smoothing State Space Model
FEMA	Federal Emergency Management Agency
FIRM	Flood Insurance Rate Map
GCM	Global Climate Model
GDP	Gross Domestic Product
GEV	Generalized Extreme Value
GHG	Green House Gas(es)
GIC	Glaciers and Icecaps
GIS	Geographical Information Systems
GMSL	Global Mean Sea Level
GOM	Gulf of Mexico
GPS	Global Positioning System
HAT	Highest Astronomical Tide
HTF	High Tide Flooding
HURDAT2	Atlantic Hurricane Database
IPCC	Intergovernmental Panel on Climate Change
LAT	Lowest Astronomical Tide
LiDAR	Light Detection and Ranging
MEI	Multivariant ENSO Index
MEOW	Maximum Envelope of Water
MHHW	Mean Higher-High Water
MHW	Mean High Water
MLLW	Mean Lower-Low Water
MLW	Mean Low Water
MOM	Maximum of MEOWs
MSL	Mean Sea Level
NAO	North Atlantic Oscillation

NAVD88	North American Vertical Datum
NED	National Elevation Dataset
NFHL	National Flood Hazard Layer
NFIP	National Flood Insurance Program
NHC	National Hurricane Center
NOAA	National Oceanic and Atmospheric Administration
NTR	Nontidal Residual
NWS	National Weather Service
OGCM	Ocean General Circulation Model
PACF	Partial Autocorrelation Function
PDF	Probability Density Function
PDO	Pacific Decadal Oscillation
PSMSL	Permanent Service for Mean Sea Level
PSL	Physical Science Laboratory (NOAA)
RCP	Representative Concentration Pathway
RSL	Relative Sea Level
RSLR	Relative Sea Level Rise
TxDOT	Texas Department of Transportation
THI	Tropical Hazard Index
SA	Solar Annual Tidal Constituent
SARIMA	Seasonal Autoregressive Integrated Moving Average
SLOSH	Sea, Lake, Overland Surges from Hurricanes
SLR	Sea Level Rise
SMB	Surface Mass Balance
SSA	Solar Semi-Annual Tidal Constituent
SSH	Sea Surface Height
SST	Sea Surface Temperature
SURGEDAT	Gulf of Mexico Peak Surge Database
SVI	Social Vulnerability Index
SWAN	Simulating Waves Nearshore Model
USACE	United States Army Corps of Engineers
USGS	United States Geological Survey
VLM	Vertical Land Movement
WFO	Weather Forecasting Office

Chapter 1: General Introduction and Objectives

1.1 General Introduction

Coastal communities have historically experienced occasional flooding events from storm surges and anomalously high astronomical tides. Sea level, which remained stable for ~2000 years prior to the industrial revolution, has been rising in the past century with acceleration from anthropogenic perturbation of the climate since the 1990s. This has a direct effect on the frequency and severity of coastal flooding by decreasing the gap between mean sea level and fixed coastal infrastructure. The rise in global sea level is attributed to rising ocean heat content causing thermal expansion and the melting of glaciers, ice caps, and the large ice sheets of Antarctica and Greenland. Rising global temperature related to increased anthropogenic greenhouse gas emissions is responsible for these effects and the impact on sea level rise will continue into the coming centuries regardless of efforts to reduce emissions. Sea level rise observed at a specific coastal location can differ significantly from the global average depending on regional ocean dynamics, changes in gravity caused by melting ice sheets, and localized vertical land movement. This study focuses on the risk associated with this relative sea level rise (RSLR) to communities and infrastructure on the coast of Texas and Louisiana where rates of RSLR are faster than the global average.

Located in the northern Gulf of Mexico, the Texas and Louisiana coasts are characterized by deltaic environments, barrier islands, and low sloping beaches. The area is home to nearly 10 million residents and supports major industrial, commercial, fishing, and tourism practices. While rates vary by location, subsidence caused by sediment compaction, glacial isostatic adjustment, and subsurface water and hydrocarbon extraction, is causing the land to sink while the sea level rises. This represents an increasing risk of flooding in the area that has historically observed some of the most devastating impacts from tropical cyclones including the Great Galveston Hurricane of 1900, Hurricane Katrina (New Orleans, 2005), and Hurricane Harvey (Houston, 2017). Because of this history, and the fact that many communities and industry are situated at low elevations or below sea level, flood defenses such as sea walls and levees have been engineered to protect from historic extreme water levels. However, RSLR, and the uncertain rate of acceleration of global sea level rise requires an assessment of future risk to ensure communities located in areas of historic risk will be protected and that areas that have not previously been considered vulnerable are accounted for. Additionally, RSLR may lead to the emergence of hazards associated with coastal flooding events not previously observed in the record.

Coastal flood risk assessments often use historical observations to derive statistics that inform decision making and design criteria. This frequently includes return periods that estimate how often a major hurricane can be expected to make landfall (in number of years), and the 100-year peak surge recurrence interval. Storm surge is frequently assessed based on models that simulate surge under current sea level and sea level rise is considered separately. When sea level is considered, global sea level rise scenarios, often from the IPCC, are utilized to project future risk. However, the IPCC bases its projections on a *likely* range (67% probability) while the highest 17% of possible effects are not accounted for, nor is subsidence. Relying solely on historical data and changes in global sea level leaves unanswered questions associated with future risk to Texas and Louisiana coastal communities. This study seeks a comprehensive assessment of future flood risks that addresses these questions, such as, what are the dominant factors contributing to coastal flooding under future relative sea level rise projections? What is

the coastal risk in response to the combined natural and anthropogenic induced sea level extremes for the future? And how can coastal flood risk assessments be improved upon to communicate the increasing risk of more frequent and severe flooding?

This study utilizes a combination of historical data, statistical analysis, trend analysis, and future projections to assess the risks of coastal flooding in Texas and Louisiana to 2100. The data include but are not limited to observations recorded by tide gauges operated by the National Oceanic and Atmospheric Administration (NOAA) at various fixed locations, the Gulf of Mexico Peak Surge Database, the Atlantic Hurricane Database (HURDAT2), vertical land movement rates derived from published literature, and modeled storm surge (SLOSH) output. How this data is used to produce results used in this analysis is detailed in the Methodology sections for each chapter of the dissertation.

Chapter 2 presents a future flood vulnerability assessment for Harris County, Texas, in the wake of devasting flooding from Hurricane Harvey in 2017. The storm made landfall as a category 4 hurricane and produced over 1000 mm (~40 inches) of rain over five days in the Houston metro area as the storm stalled and continued to draw in tropical rainfall from the Gulf of Mexico. This led to inundation of major roadways in one of the most auto-dependent regions of the US. The study focuses on identifying areas susceptible to flooding from extreme precipitation and storm surge and assesses the transit demand and availability within these vulnerable neighborhoods. The assessment uses geographic information system (GIS) overlay analysis of the FEMA 100- and 500-year floodplains, SLOSH modeled storm surge maps, transit maps, and US Census demographics to locate transit-dependent populations within flood hazard zones. A sea level rise scenario of ~2.5 meters by 2100, based on representative concentration pathway (RCP) 8.5 consistent with the highest emissions scenarios in the literature, is added to the modeled storm surge. Combining a future sea level rise scenario with the modeled category 5 storm tide allows for identification of populations that may be susceptible to flooding from the maximum storm tide by 2100.

While the study presented in Chapter 2 is adequate to assess maximum possible risk by 2100 using the high-end scenario of global sea level rise, local officials and city planners desire site-specific projections of sea level rise over varying time horizons. For this purpose, Chapter 3 focuses on RSLR (defined as the sum of global sea level rise, regional non-linear processes, and local vertical land movement) and future projections. First, RSLR rates (mm/year) derived from monthly mean sea level observations at nine tide gauges in Texas and Louisiana with adequate records are analyzed. Varying rates of RSLR, all higher than the global average, reflect the site-specific subsidence rates at different locations within the study area. Second, RSLR projections using a seasonal autoregressive integrated moving average (SARIMA) model are compared to a probabilistic methodology previously developed and utilized by NOAA in national assessments. Forecasts using SARIMA can be derived solely from raw (unsmoothed) tide gauge data with low computational costs and incorporate the long-term linear trend as well as the annual seasonal cycle. Unfortunately, unless acceleration is inherent in the data (i.e., the long-term trend is non-linear) SARIMA does not forecast acceleration that is likely over the coming decades. Probabilistic projections utilize the Coupled Model Intercomparison Project 5 (CMIP5) global climate models under varying RCP acceleration scenarios imposed on the background vertical land movement rates to derive projections by decade to 2100. While this method does include acceleration, the complex nature of the global climate and uncertainty inherent in global climate modeling need to be addressed for proper use of the projections.

The greatest uncertainties related to sea level rise attributed to anthropogenic-induced climate change are associated with the dynamics of the melting cryosphere, specifically the Greenland and Antarctic ice sheets. Tipping points of the collapse of Greenland and West Antarctic Icesheets in response to accelerated anthropogenic-induced global warming are not well understood. Although advances are being made in this field to incorporate new knowledge of ice sheet dynamics into global climate models, the topic remains uncertain from a risk assessment standpoint. Additionally, the output from global climate models can vary greatly from small changes in the initial conditions, boundary conditions, and parameters used. Another source of uncertainty is the future of anthropogenic emissions of greenhouse gases. The anthropogenic uncertainty is addressed by using multiple RCPs derived from population projections, gross domestic product, energy efficiency, land use, and other factors that contribute to anthropogenic radiative forcing. Thus, probabilistic projections provide a range of possible outcomes in the form of multiple scenarios (i.e., "Intermediate", "High", "Extreme") that relate to global sea level rise while incorporating the subsidence rate unique to each location. The best use of the RSLR scenarios in risk assessment to account for uncertainty is to select two scenarios that have less than 50% probability of exceedance by 2100 whose envelope of outcomes defines the design range, and a scientifically plausible extreme scenario. This method has broad applications in risk assessments as inundation maps utilizing projections can provide temporal and geospatial results of high tide water levels under each scenario. This is most useful for engineers, designers, and planners making key decisions about how much RSLR will impact new or existing infrastructure. For infrastructure where flooding represents a particular danger to the public (e.g., nuclear power plants; wastewater treatment facilities; etc.), projects with long planning horizons, or infrastructure with limited adaptability, failure to include low-probability, high-risk scenarios in decision making may result in higher future risk.

This methodology using probabilistic projections of RSLR is applied in a case study of New Orleans, LA, and Galveston, TX. The intermediate, intermediate-high, and extreme scenarios are considered for mapping the inundated areas over time (20-year periods) and for mapping height above ground by 2100. Thus, populations and infrastructure within the predicted area of inundation can be identified and the timing and severity of impacts analyzed. For example, results indicate that under the intermediate scenario, the lowest elevations located on the back bay side of Galveston Island will begin to experience impacts from RSLR at high tide by 2060, and by 2100 the inundation at high tide will be 1.2-1.5 meters above ground in that location.

RSLR reduces the gap between mean high tide and existing flood threshold levels set at each tide gauge location. Coastal flooding events are defined as any exceedance of the flood threshold elevation whether it be one hour from a high tide or 24 hours from a hurricane. Generally, a coastal flooding event can be caused by several phenomena including perigean spring tides, seasonally higher water levels resulting from El Niño southern oscillation (ENSO), surge from tropical and extratropical storms, tsunamis, changes in currents, swells from distant storms, and others. In Chapter 4, hourly tide gauge data from six locations in Texas and Louisiana is examined for flood threshold exceedance from 1980-2019 and the various factors contributing to said exceedances is determined along with the seasonality of the occurrences. In this way, all possible coastal flood risks that impact the study area will be accounted for and those that do not can be eliminated from risk analysis. For example, extratropical storms do not occur in the Gulf of Mexico, and this is confirmed by the lack of a wintertime peak in maximum daily water levels observed in the record. For this purpose, spectral analysis is employed to decompose the 40-year

hourly tide gauge data into the seasonal mean sea level cycle, the astronomical tide without the solar annual and semiannual components, and the remaining non-tidal residuals.

Analysis reveals that high tide flooding events are increasing in frequency and duration as relative sea levels have risen over the past 40 years. Results from all locations show peaks in flood threshold exceedance coinciding with the seasonal sea level maxima during September and October superimposed with peaks in non-tidal residuals associated with hurricane season. The analysis indicates the solar tidal constituents influence the seasonal sea level cycle with no direct effects from ENSO in the Gulf of Mexico, and no peaks above threshold coincided with perigean spring tides. It should be noted that a 30-day smoothing is applied to the data to emphasize patterns rather than individual events, and the overall pattern shows that peaks over flood threshold are primarily driven by the non-tidal residual component associated with storms. Thus, trends in tropical cyclone activity and associated storm surge are examined to determine if changes in tropical cyclone climatology and associated climate oscillations represent an additional increasing risk to coastal Texas and Louisiana.

From an extensive history of tropical cyclones and storm surges it is determined that Atlantic basin tropical cyclone frequency is increasing and that half of the largest storm surges over the Texas and Louisiana record are observed in the past two decades. The analysis does not find any trends or patterns in landfalling storms within the study area, nor does it indicate any correlations between landfalls and peak surge with the Atlantic Multidecadal Oscillation or ENSO, both of which are correlated with total Atlantic basin activity. However, peak surge return periods estimated from changes in 30-year averages from the baseline (1930-1960) in surge frequency and magnitude suggest an increase of the 100-year peak surge of ~2.5 meters. Additionally, probability density functions of annual hourly tide gauge data show an increase in the probability of exceeding flood thresholds over past decades, particularly in the upper tails of the densities. The analysis in Chapter 4 confirms that RSLR is the primary factor leading to increased risk of coastal flooding in Texas and Louisiana. This risk arises from RSLR-enhanced storm tides by increasing the surge magnitude relative to the storm strength so that lower category storms produce surges equal to a higher category hurricane. An additional risk from high tide, or "nuisance" flooding, is also identified in locations with higher tide ranges (Port Isabel and Corpus Christi, TX) and has increased significantly at all locations so that as RSLR continues, all locations may experience the compounding risk in the future.

To determine the combined natural and anthropogenic sea level extremes for the future, a case study of RSLR-enhanced storm tide inundation in the Baton Rouge, LA, and Houston-Galveston, TX, areas is presented. Utilizing the site-specific RSLR probabilistic projections of Chapter 3, projections are added to SLOSH modeled storm tides similarly to Chapter 2. Following the methodology laid out in Chapter 3 to account for deep uncertainty and to address the needs of planners and policy makers, the "Intermediate", "Intermediate-High", and "Extreme" RSLR scenarios are added to the category 1, 3, and 5 storm tides to identify areas and populations vulnerable to flooding by 2100. The study includes an additional social risk by identifying populations within inundated areas that, according to the Center for Disease Control's Social Vulnerability Index, are in the top 90th percentile for (1) poverty, (2) disabilities, (3) age 65 and older, (4) age 17 and younger, (5) mobile homes, and/or (6) no access to vehicle. Inundation mapping is used to identify total population affected, the increase in inundated area, and the change in the number of particularly vulnerable populations affected by each category storm tide under the three RSLR scenarios.

In summary, the results of this dissertation offer some answers to the questions previously mentioned above. Coastal flooding events in Texas and Louisiana are dominated by tropical cyclone induced storm tides enhanced by the seasonal mean sea level cycle of the northern Gulf of Mexico. Relative sea level rise represents an increasing risk by reducing the gap between the mean high tide and the flood threshold level. The probability of flood threshold exceedance is increasing and will continue to increase as sea levels rise. Therefore, high tide flooding that in the past occurred rarely will become a regular hazard in the coming decades. Non-tidal residuals associated with storms are the main driver of flood threshold exceedances observed from 1980-2019. This study finds that relative sea level rise, rather than changes in tropical cyclone climatology or climate oscillations, is the primary factor contributing to flood threshold exceedance and will continue to present an increasing risk of more frequent, longer lasting, and greater magnitude coastal flood events.

1.2 Hypothesis and Objectives
This dissertation seeks to test the following hypothesis:

Sea level rise is increasing the frequency, magnitude, and duration of coastal flooding events in Texas and Louisiana representing an increasing risk to currently vulnerable locations and a future risk expanding to areas not historically affected.

In this study, the causes of coastal flooding in Texas and Louisiana were examined utilizing historical observations, future sea level projections, and storm surge model output. The focus is primarily on the risk of flooding to populations and infrastructure as well as the future outlook of said risk with climate change induced sea level rise. The goals of this study were to analyze the following:

I. What are the dominant factors contributing to coastal flooding under future sea level rise projections?

Global mean sea level rise has accelerated since the preindustrial era with projections of increased acceleration into the future. Due to increasing global mean temperature, thermal expansion of sea water and melting of land ice, projections of up to 2.5 meters of sea level rise relative to 1991-2009 may be expected by 2100. In Texas and Louisiana, subsidence exacerbates the rise in global sea level making the rate of relative sea level rise faster than the global average. Coastal flooding can occur from tropical cyclone induced storm surge, swells from distant storms, spring tides, tsunamis, and anomalies attributed to oceanic processes. The objective in this study is to identify which of these factors contribute most to coastal flooding events in Texas and Louisiana and analyze potential changes to the frequency and magnitude of these events under future sea level projections. This is achieved by addressing the following:
I.1 Is the probability of exceeding flood thresholds leading to high tide flooding increasing over time as relative sea level rises and is this consistent at all locations in Texas and Louisiana?
I.2 How do astronomical tides, seasonal sea level cycles, and non-tidal residuals contribute to exceedance of flood thresholds?
I.3 How have frequency and magnitude of storm tides changed over the historical record and what changes are projected for the future?

I.4 Are climate oscillations and historical changes in tropical cyclone climatology correlated to increased flooding via non-tidal residuals?

II. What is the coastal risk in response to the combined natural and anthropogenic induced sea level extremes for the future?

Communities along the coast of Texas and Louisiana have been under risk of coastal flooding since people began residing there. Records indicate that at least 135 storm surge events have been recorded over the last 140 years (1880-2020) in these locations. Thus, infrastructure has been designed with this historic risk in mind and includes built flood defenses such as levees and seawalls. A consequence of rising sea levels relative to the fixed elevations of current infrastructure include increased inundation during extreme events. Another observation in the historical record is an increase in exceedance of minor flood thresholds leading to high tide flooding. These lesser extreme events have historically occurred occasionally but have become much more frequent since 2010. The objective in this study is to define the natural and anthropogenic factors influencing the increase in high tide flooding risk and identify areas, populations, and infrastructure at future risk from storm surge enhanced by relative sea level rise. This is achieved by addressing the following:

II.1 What is the primary factor contributing to an increased risk of flood threshold exceedance?
II.2 How do different relative sea level rise scenarios affect inundation risk from modeled storm tides of varying magnitude?

III. How can coastal flood risk assessments be improved upon to communicate the increasing risk of more frequent and severe flooding?

Risk assessments of coastal flooding commonly use historic observations and statistics to inform decision making and design criteria, such as the 100-year flood return period and historic storm surge heights. Changes in frequency and magnitude of coastal flood events over the past twenty years and projected increases into the future are under accounted for. Due to compounding uncertainties in the climate system, climate models, and anthropogenic emissions, projections of future coastal flood risks are complex. The objective in this study is to develop a methodology to effectively communicate the increasing risks while accounting for uncertainty in future projections. This is achieved by addressing the following:

III.1 What method of projecting future relative sea level can provide an appropriate range of possible outcomes for use in risk assessment?
III.2 How do return periods change when accounting for changes in frequency and magnitude of storm tides?

For the case that coastal flood risk assessments are extended beyond the historical data to include future projections of relative sea level, changes in probability and duration of high tide flooding, and projected changes in tropical cyclone activity with storm surges enhanced by relative sea level rise, then the evolution of future flood hazards in the region will be fully captured. Due to varying subsidence rates within the study area, localized projections provide a more accurate forecast for risk assessors and policymakers.

Chapter 2: Analysis of Flood Vulnerability and Transit Availability with a Changing Climate in Harris County, Texas

Abstract

Hurricanes and other extreme precipitation events can have devastating effects on population and infrastructure that can create problems for emergency responses and evacuation. Projected climate change and associated global warming may lead to an increase in extreme weather events that results in greater inundation from storm surges or massive precipitation. For example, record flooding during Hurricane Katrina or more recently, during Hurricane Harvey in 2017, led to many people being cut off from aid and unable to evacuate. This study focuses on the combined impact of storm tides and extreme rainfall under climate change for areas of Harris County, TX, and evaluates the transit demand and availability in those areas. Future risk of flooding in Harris County will be assessed by GIS mapping of the 100-year and 500-year FEMA floodplains and most extreme category 5 storm tide and global sea level rise. The flood maps have been overlaid with population demographics and transit accessibility to determine vulnerable populations in need of transit during a disaster. It was calculated that 70% of densely populated census block groups are located within the floodplains including a disproportional amount of low-income block groups. The results also show a lack of transit availability in many areas susceptible to extreme storm surge exaggerated with sea level rise. Further study of these areas to improve transit infrastructure and evacuation strategies will improve the outcomes of extreme weather events in the future.

2.1 Introduction

Extreme weather events such as hurricanes have had devastating impacts on communities and infrastructure and affected the most vulnerable populations in flooded areas. For example, category four Hurricane Harvey, generated 103 storm-related deaths, widespread flooding of more than 50,000 homes and over 500,000 vehicles, more than 17,000 water rescues, and 126 billion dollars of economic damages in Texas (Blake and Zelinsky, 2018). Rainfall of over 1000 mm (~40 in) in the Houston metropolitan area, in particular in Harris County led to extreme flooding because of slow movement of the storm system. The effect of this storm on the Houston metropolitan area is unique because ~91% of the commuters in the Houston Metro area travel alone by car, making it one of the most auto-dependent places in the United States. Inundation of major roadways require evacuation strategies that adapt to these conditions. The projected extreme weather events amplified by climate change require a risk assessment of how vulnerable populations and infrastructure are affected by flooding from sea level rise, storm surge, and extreme rainfall events.

2.1.1 Sea Level Rise

Assessing global and regional sea level rise (SLR) due to global warming is of great interest to coastal populations, such as those along the Gulf of Mexico, due to increased tidal flooding and storm surges (Hellgatte et al., 2013). Global mean temperature is expected to increase over 3℃ by 2100 due to anthropogenic-induced greenhouse gas emissions into the atmosphere (Stocker et al., 2014) that lead to an increase in global mean sea level (GMSL) by melting of ice sheets, in particular the Greenland ice sheets and associated ice shelves, glaciers, and thermal expansion by increased global sea temperatures (Wuebbles et al., 2017). The geologic record of the last million years suggests that during ice ages, GMSL is low due to build-up of ice sheets and glaciers, and thermal contraction (Dutton et al., 2015).

Vertical land movement is a significant factor in regional sea level change. Subsidence resulting from extraction of groundwater or other resources can effectively raise the sea level by lowering the land elevation. In addition, sediment deposition in the Gulf of Mexico originating from the Mississippi River runoff enhances this subsidence.

Projected SLR is characterized by substantial uncertainties, because of the range of future changes in radiative forcings as defined by representative concentration pathways (RCP), and because of the uncertain rate of melting of ice sheets and mountain glaciers. In the most extreme scenario, the RCP 8.5 "business as usual" scenario, sea level is predicted to change by 2.4 m or ~8 feet due to massive melting of the Greenland ice sheet, glaciers, and thermal expansion (Wuebbles et al., 2017).

2.1.2 Storm Surge and Storm Tide

In the past decades, low sloping beaches and near-coastal areas of the Gulf Coast of the U.S. have been affected by an increase in intense tropical storms with associated storm tides and heavy precipitation (Wahl et al., 2015). Storm surges, and associated erosion and landscape changes, threaten critical infrastructure such as roads and bridges and can cause wide-scale flooding. Understanding storm surge and storm tide and how it will increase with climate change is essential to protecting vulnerable areas into the future.

A storm surge is a rise in water produced by a storm above the normal tide level, while a storm tide is that storm-generated surge on top of the astronomical high tide. While coastal locations are particularly vulnerable, storm surge inundation from hurricanes can move inland significantly. The magnitude of the storm surge depends on a variety of factors including the wind stress from the storm, slope of the beach, water depth, bottom friction, wave height, precipitation, atmospheric pressure, and other factors (Harris, 1963).

Water masses in the Gulf of Mexico are pushed onshore in a multifaceted process that is dependent on intensity, speed, size of the storm, angle of approach, and central pressure as well as the shape and topography of the basin (NHC, 2018). Surface waves generated by winds move in the direction of the winds and can be a source of significant transport of water masses to the shore (Harris, 1963). The buildup of water masses on the downwind side of a basin known as "wind set-up" effectively raises the sea level on the coast if the wind is directed toward the coast, and water penetrates the basin comparable to the tides. Separate from wind set-up, "wave set-up" can also occur when water carried toward the shore by breaking waves piles up near the shore and contributes to an overall higher surge (Longuet-Higgins, 1983).

The atmospheric pressure of a hurricane is a major contributing factor in the intensity of the storm. A deeper low pressure center results in a significant pressure gradient force which, combined with the Coriolis force, leads to higher geostrophic winds and tighter counterclockwise rotation. Sea level rise due to atmospheric pressure plays a less significant role in storm surge than wind, but nonetheless contributes to the height of the storm surge. In theory, the sea level rises directly under the low-pressure center 1 foot for every 1-inch drop in mercury reading. Hurricane Katrina had a central pressure of 27 inches of mercury, with 30 being average. This means that the sea level under the hurricane was elevated approximately 3 feet simply due to the low-pressure system (Anderson and Battjes, 2007).

The significant precipitation that occurs with tropical cyclones is also a contributing factor to coastal flooding. Heavy precipitation reaching 1500 mm (60 in) in a short period has been observed with Hurricane Harvey and led to rapid flooding of rivers, reservoirs, and low-elevated

areas. Reducing or reversing the drainage of rivers by the storm surge can amplify the flooding (Harris, 1963).

2.1.3 Storm Surge Modeling

In order to model hurricane storm surge to predict inundation heights and locations, the National Weather Service (NWS) developed the Sea, Lake, Overland Surges from Hurricanes (SLOSH) model. The model integrates terrain, bathymetry, and physical barriers along with the physics equations of motion to show how surge waters flow inland with landfall of a hurricane (Jelesnianski et al., 1992). SLOSH incorporates specific data from hurricanes such as atmospheric pressure, direction, and speed to model the winds and storm surge along the coasts. Geographically specific polar grids are applied to basins, and there are SLOSH basins to cover the entire coast from Maine to Texas. Each basin represents inland topography; waterways such as bays, lakes, and rivers; and a section of continental shelf (Jelesnianski et al., 1992). SLOSH is capable to simulate hurricane maximum envelopes of water (MEOWs) based on input parameters (pressure, speed, direction, size), or maximum of MEOWs (MOMs) that represent a worst-case scenario. MEOWs and MOMs are generated through computing the maximum surge for thousands of theoretical storms with varying parameters within each basin (Zachry et al., 2015). MOMs are available as a mean-tide product or a high-tide product where high tide values are added to the storm surge height. SLOSH can also simulate historical models of past hurricane storm surges that compare well to the historical data.

SLOSH uses the equations of motion as developed for wind tide (eq. 2.1-2.3) by Platzman (1963) and modified by Jelesnianski (1967) for storm surge to include bottom stress. The equations are:

$$\frac{\partial U}{\partial t} = -g(D + h)\left[B_r \frac{\partial(h - h_0)}{\partial x} - B_i \frac{\partial(h - h_0)}{\partial y}\right] + f(A_r V + A_i U) + C_r x_\tau - C_i y_\tau \qquad (2.1)$$

$$\frac{\partial V}{\partial t} = -g(D + h)\left[B_r \frac{\partial(h - h_0)}{\partial y} - B_i \frac{\partial(h - h_0)}{\partial x}\right] - f(A_r V + A_i U) + C_r y_\tau - C_i x_\tau \qquad (2.2)$$

$$\frac{\partial h}{\partial t} = \frac{\partial U}{\partial x} - \frac{\partial V}{\partial y} \qquad (2.3)$$

where U,V denotes the meridional transport of water masses, g is the gravitational acceleration constant, D is the depth of quiescent water relative to a common datum, h denotes the height of water above datum, h_0 is the hydrostatic water height, f denotes the Coriolis parameter, x_τ, y_τ are surface stresses, and $A_r, ..., C_i$ are bottom stresses. The surface stress (τ) represents meteorological data with many variables, and the bottom stress term represents frictional forces with many variables. Coefficients for these terms are derived using empirical data from past storms and surges. There are some coefficients such as surface drag and vertical eddy viscosity coefficients that cannot be empirically determined and must be specified (Jelesnianski et al., 1992). Topographic data are acquired from U.S. Geological Survey (USGS) three-dimensional elevation program in 1 arc second segments and incorporated into SLOSH for inundation modeling.

2.1.4 Storm Surge Measurement

Storm surge data have been collected by utilizing a combination of tide gauges, high water marks, and pressure sensors. Tide gauges operated by the National Oceanic and Atmospheric Administration (NOAA) that measure water levels at 175 locations along the coast can be used

to recover storm surge height data (NHC, 2018). The United States Geological Survey (USGS) measures high water marks after a storm surge event. The marks indicate the maximum water level of the surge and are used to determine inundation height. Trained personnel are disbursed in the area following a storm surge to identify and measure mud lines, seed lines, foams lines and other indications of high water (Koenig et al., 2016). Prior to a predicted storm, USGS deploys temporary sensors to the area expected to be inundated that collect data on water level and barometric pressure. Some of these sensors use water pressure to determine the water level while others measure water level directly while also recording the barometric pressure (McCallum et al., 2012).

As noted in the National Hurricane Center Tropical Cyclone Report on Hurricane Harvey, the storm tide produced inundation levels of 6 to 10 feet during landfall. Tide gauge data indicated a maximum of 6.7 feet above mean high water at Port Lavaca, Texas, while temporarily installed sensors at Hynes Bay indicated a water level of 8.7 feet above mean high water. Surveys of high-water marks conducted in the area indicated inundation of 11-12 feet but were likely influenced by waves (Blake and Zelinsky, 2018).

2.1.5 Floodplains

Flood risks from extreme rainfall include riverine flooding, coastal flooding, and shallow flooding. Floodplains have been developed to assess the risk of potential flooding in riverine and watershed areas, coastal areas, and other topographically low-lying areas. Riverine flooding occurs in watershed areas and is defined as any event when water rises over the banks of a channel and flows into a floodplain. Overbank flooding is the most common form of riverine flooding and occurs when the downstream channels receive more water from the watershed than normal (O'Connor and Costa, 2003). The topography of the region plays a large role in the extent, depth, and velocity of the flood. Flash flooding occurs when a particularly large amount of rain falls in a short period of time that overwhelms the banks of the channels. Urban areas with little permeable surfaces are particularly vulnerable to flash flooding. In addition to channels being inundated with water masses, the increased velocity of water masses during a flood promotes erosion of the riverbanks that can enhance flooding. In depressed areas, shallow area flooding can be enhanced by holding-up, slow permeation of soil, or damming of water masses referred to as ponding.

The Federal Emergency Management Agency (FEMA) utilizes the National Flood Insurance Program (NFIP) classifications of floodplains to develop Flood Insurance Rate Maps (FIRMs) for almost every community in the nation (FEMA, 2018). These maps typically show floodways, a 100-year floodplain, a 500-year floodplain, as well as any other flood hazard areas such as coastal flood zones. Riverine flooding, shallow flooding, and coastal flooding are all considered when assessing floodplain classification.

A floodway is a river or stream channel that carries most floodwaters where building is limited. The 100-year floodplain refers to a probability of one percent that a flood of that magnitude will occur in any given year and is also referred to as the one-percent annual chance flood. Similarly, the 500-year floodplain is the 0.2% probability that a flood of that magnitude will occur in any given year. The different types of flooding are studied in detail by FEMA scientists and engineers to generate FIRMs that show the locations of the floodplains and floodways. Floodplains are derived by combining elevation mapping with hydrology studies to determine the floodwater elevation above ground. These FEMA floodplain maps are useful tools to determine flood risk, but extreme weather events such as Hurricane Harvey produced a flood

that exceeded the 500-year flood and was in fact a 0.1% probability flood or 1000-year flood (Blake and Zelinsky, 2018). A study conducted for FEMA to analyze the effects of climate change and population growth on floodplain classification predicted an average increase in the 100-year floodplain area of up to 45% by 2100, with 70% of that change attributed to climate change alone (AECOM, 2013).

2.1.6 Transit Availability

Flooding makes roads impassable therefore complicating evacuation efforts during disasters. Many people reliant on public transit may be stranded in the case of a flooding emergency due to lack of transit availability, or a lack of knowledge that their home is in a floodplain. Low-income neighborhoods rely the most on public transit and these neighborhoods are most likely to be located within a floodplain.

Research indicates limited transportation options exist in low-income, sprawling areas, and this restricts employment opportunity and upward mobility as well as access to medical care. Low-income households are less likely to own a vehicle or enough vehicles to transport all members of the household. Addressing transit deserts is important for engaging broader social issues such as inequity and welfare dependence (Jiao and Dilivan, 2013). A transit desert is similar to the widely studied topic of a "food desert" which has had great influence on planning and policy. Transit dependent populations require transit service more than others and include individuals who are too young, too old, or physically unable to drive as well as individuals who cannot afford to (Jiao and Dilivan, 2013).

Demographic changes that occur in metropolitan regions are geographic, shifting between urban and suburban. Many middle class and affluent families are moving to the urban centers with access to services, amenities, and public transportation. The poor are moving to the outlying areas where services and transportation are lacking. Services in the outer urban neighborhoods are limited due to the false assumption that people who choose to live in those areas own vehicles. Transit deserts, therefore, are locations of inequity where those who own cars are not affected by the inadequacy of transit while those who have no vehicle are disadvantaged (Allen, 2017).

Transit desert communities present dilemmas that fall outside of existing demand forecasting parameters. Catalytic forecasting operates dynamically in the opposite realm of demand forecasting, evaluating areas based on the full potential of urban dwellings. Numbers based upon the maximum frequency of use force communities to plan for accurate and meaningful efforts towards accessible public transportation. Catalytic forecasting can be deemed a subjective method in that it puts demand at every parcel in a transit shed, although traditional transportation planning requires objective forecasting to be useful. Transit deserts are the results of subjective policy and market forces which created areas that lack transit access and hold an invisible population. Demand forecasting privileges a certain population and catalytic forecasting is a way to more accurately reflect the kinds of systems that should be produced to create equity (Allen, 2017).

2.2 Objectives

To increase efficient evacuation during extreme weather events, areas of vulnerability will be identified through analysis of the impacts of flooding from hurricane storm surge in a rising sea and increasing rainfall events in a warming climate. The area of focus for this project is Harris County, Texas, which was devastated by floods during Hurricane Harvey in 2017. The overall

aims of the research are to identify areas prone to flooding from storm surge or extreme precipitation and evaluate the transit availability of those areas. The results of this project will be used for future studies involving FEMA and NWC to evaluate the evacuation response to disasters and how the transportation infrastructure is affected by flooding.

2.3 Methods

A Geographic Information System (GIS) was employed, and several map layers were utilized including a Digital Elevation Model (DEM), FEMA National Flood Hazard Layer (NFHL), and storm tide inundation (SLOSH) with SLR along with demographic and transit data to focus on vulnerable populations and infrastructure of Harris County, Texas.

The DEM layer was compiled from tiles of the USGS national elevation data set (NED) in 1/3 arc-second n31w096 1 x 1-degree ArcGrid 2018 and NED n30w096 1/3 arc-second 2013 1 x 1-degree ArcGrid resolution. The tiles were then combined using the mosaic to new raster function of ArcGIS and the final DEM was clipped to include only Harris County. The layer was then converted from meters to feet and values expressed in increments to better visualize the low elevation areas.

The floodplain map obtained through the FEMA map service center was from the 2015 NFHL that included the latest updates and modern floodplain classifications. The layer combined all the areas of 1% chance annual flood, 0.2% chance annual flood, floodways, and coastal flood hazard areas as well as areas of minimal flood risk. The map layer's symbology was altered to remove areas of minimal flood risk and visualize the 1% and 0.2% chance annual flood or 100-year and 500-year floodplains. A new layer was created after removal of areas of minimal flood risk so the layer could be used to join and relate data from demographics and infrastructure such as population and roads.

Storm surge inundation data, not including SLR, was obtained through NOAA and the National Hurricane Center (NHC) and was originally published in the American Meteorological Society Journal of Weather, Climate, and Society in 2014. NHC used the SLOSH model output for MOM at high tide along with the latest elevation model from USGS to create a seamless inundation layer for use in GIS that covers the Atlantic coast from Maine to Texas. The category five high tide scenario was chosen to show the maximum possible inundation in the area and the category three high tide was displayed to demonstrate that significant risk exists with weaker hurricanes as well.

Sea level rise of 8 feet in response to climate change was chosen to add to the category 5 storm tide layer to visualize the storm surge potential into the future. The highest elevation inundated by the storm tide layer was identified using the identify tool of ArcGIS. Raster calculations were used to select the elevations from the DEM that corresponded with the addition of 8 feet to the highest elevation inundated by the storm tide. These layers were then overlaid on the storm tide layer and symbolized to emphasize the change in the inundation area with climate change by 2100.

Data on roads were obtained through Texas Department of Transportation (TxDOT) and overlaid on the floodplain and storm tide layers for spatial analysis. Public transit routes including light rail lines, bus routes, bus stops, and transit centers were mapped in GIS in order to evaluate the transit availability and vulnerability to flooding. Population density and mean household income data obtained from U.S. Census were also mapped in GIS by census block group and overlaid on the floodplain and storm tide layers. ArcGIS was utilized to create a new layer of low-income populated areas from selecting block groups that had population density

over 3000 per square mile and had median household income of less than $30,000. To highlight the low-income block groups susceptible to flooding, a selection was made of any low-income block groups that were within the FEMA 100-year and 500-year floodplains. To assess risk due to storm surge, populated areas that overlaid the storm surge layer, as well a low-income block groups were selected to form a layer that represented that risk. That layer was then overlaid with the Houston Metro and TxDOT data layers to assess transit availability.

A transit desert map of Harris County, TX, was compiled in GIS to determine walking times from each parcel to the nearest transit center, park and ride, or bus stop. These data were then displayed as a map layer showing walking times of 5, 10, and 15 minutes to determine the locations of transit desert neighborhoods and evaluate those locations for flood vulnerability.

2.4 Results

The elevation map overlaid with the FEMA floodplain map displays a correlation between areas of low elevation and areas within the 100-year and 500-year floodplains (Figure 2-1). The floodways are in the river channels and the floodplains are in areas of low elevation adjacent to the river channels. The map demonstrates which areas would be flooded by an extreme rainfall event that represents a 1% chance annual flood or a 0.2% chance annual flood.

The FEMA floodplain map was overlaid on the population density map to analyze block groups within the floodplains (Figure 2-2). The map indicates that the floodplains exist in many densely populated areas demonstrating the need to assess the demographics and transit infrastructure of these areas. Densely populated block groups of Harris County within the floodplains are identified and mapped with the population density. Although the entire block group may not be within the floodplain, the entire block groups are selected if the floodplain exists within that block group.

The transit map of Houston shows the available bus routes and stops, transit centers, and the light rail lines along with the low-income block groups of Harris County (Figure 2-3). According to Houston Metro data, the system covers approximately 2/3 of the county and offers approximately 370,000 services per day including 1,236 active buses and 76 light rail vehicles. The most used light rail line, the northern route, carries 55,000 passengers daily. Low-income block groups that contain either the 100-year or 500-year floodplains are highlighted to demonstrate the most vulnerable populations in need of transit.

The storm tide map shows the area of inundation from a category 5 and category 3 hurricane making landfall during high tide (Figure 2-4). The inundation layer corresponds well with the elevation map to demonstrate the vulnerability to storm surge in low-lying areas. As the map shows, areas of low elevation have higher inundation levels and the opposite is true for higher elevation areas. The figure also shows how the storm tide flows up the river channels that can compound riverine flooding during a hurricane. Sea level rise was added to the category 5 storm tide to display the expansion of the inundation under RCP 8.5 SLR scenario (Figure 2-4). The map shows that areas that are not currently susceptible to the maximum storm surge may be so in the future.
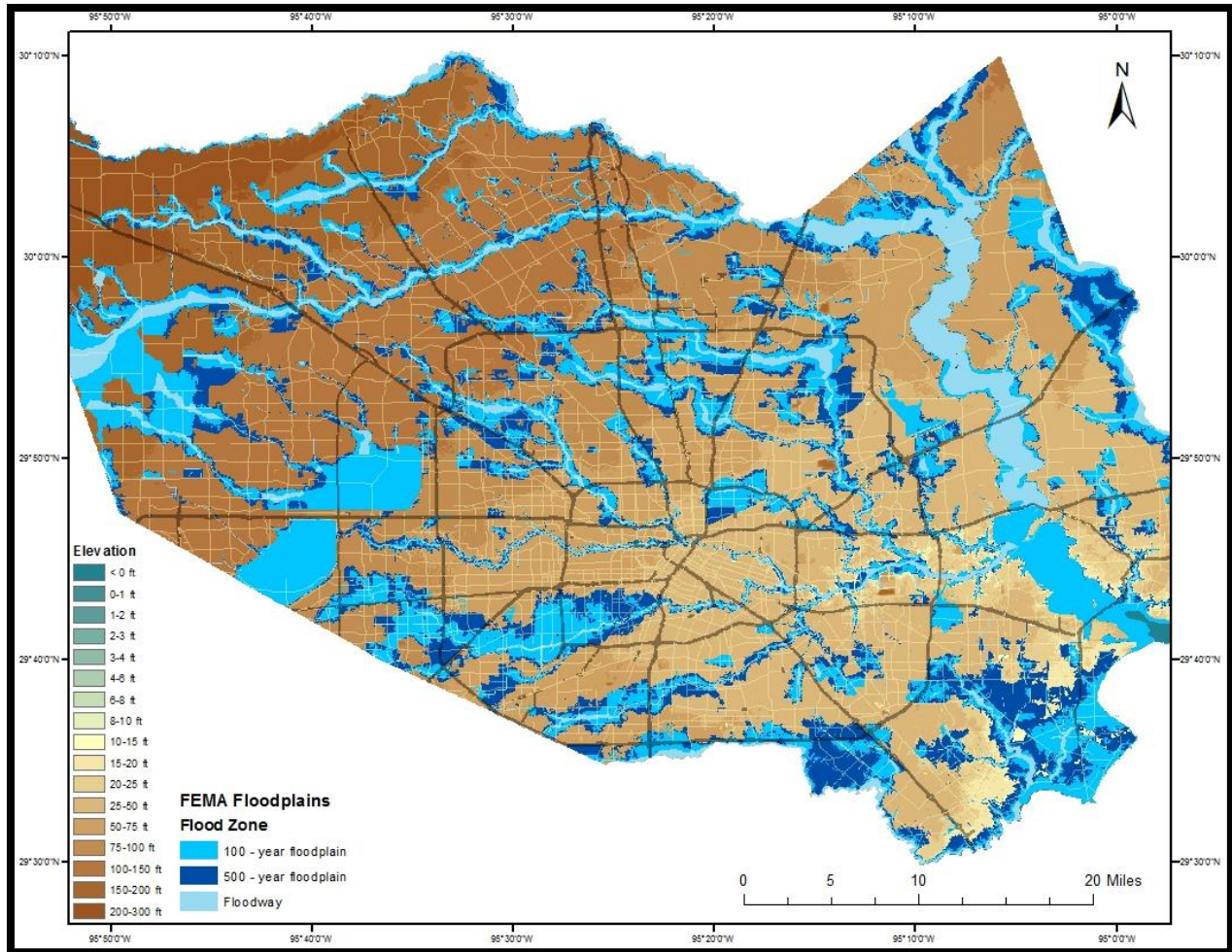
Figure 2-1. The elevation map, in feet, of Harris County, Texas, showing the FEMA 100-year and 500-year floodplains. The National Flood Hazard Layer (NFHL) 2015 was accessed through the FEMA Map Service Center. The Digital Elevation Model (DEM) was accessed through the USGS national map and includes two 1 x 1-degree grids.

Densely populated block groups affected by the category 5 storm tide as well as low-income block groups are mapped along with the transit map to evaluate areas exposed to surge (Figure 2-5). Although the storm tide layer may not inundate the entire area within each block group highlighted, the entire block groups affected in some way by the surge were chosen for evaluation. Selections of block groups within flood hazard regions of Harris County were overlaid on the transit map to display areas that have dense populations and low income (Figure 2-5). The map shows several densely populated areas within the 100-year or 500-year floodplains as well as many densely populated areas within the storm tide that have no transit availability. The figure also identifies low-income block groups in the flood hazard zones.

The transit desert map of Harris County, Texas, demonstrates the great need for transit availability in areas prone to flooding and/or storm surge (Figure 2-6). Locations that are more than ½ mile away from a transit stop should be considered for transit desert classification when overlaid with demographic data.

14
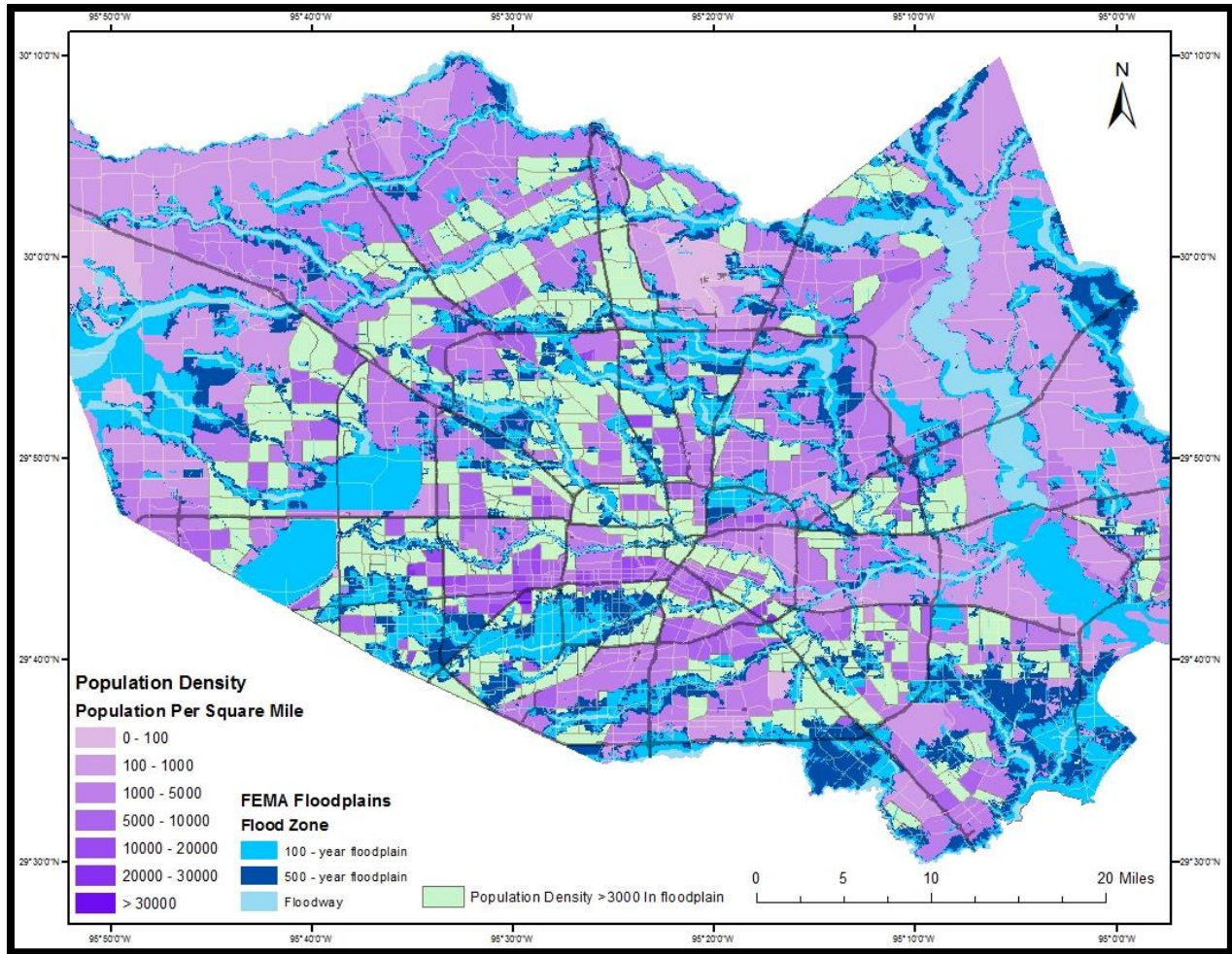
Figure 2- 2. The FEMA floodplain map of Harris County, Texas, overlaid on the population density map highlighting block groups with dense populations that are within the 100-year and 500-year floodplains.

2.5 Discussion

The strategy of detecting flood hazards through identification of vulnerable areas prone to flooding has been used in many studies. A GIS-based analysis of Harris County, TX, utilized a weighted overlay of elevation, slope, land cover/land use, normalized difference vegetation index, rainfall, flow accumulation, rivers, and roads to identify flood prone areas. While, in this case, flood risk from storm tide was neglected, the study was able to identify areas susceptible to flooding from rainfall, that indeed did flood during Hurricane Harvey, that were outside of the FEMA flood hazard zones such as downtown Houston and others (Mukherjee and Singh, 2020). As results of our study suggest, the analysis presented by Mukherjee and Singh (2020) highlights the need for updated FEMA flood hazard maps and the importance of discouraging development in flood zones.

The SLOSH model output was used along with GIS methods to identify areas vulnerable to storm tide with SLR because these resources are commonly used, available at no cost, and have low computational requirements.

15
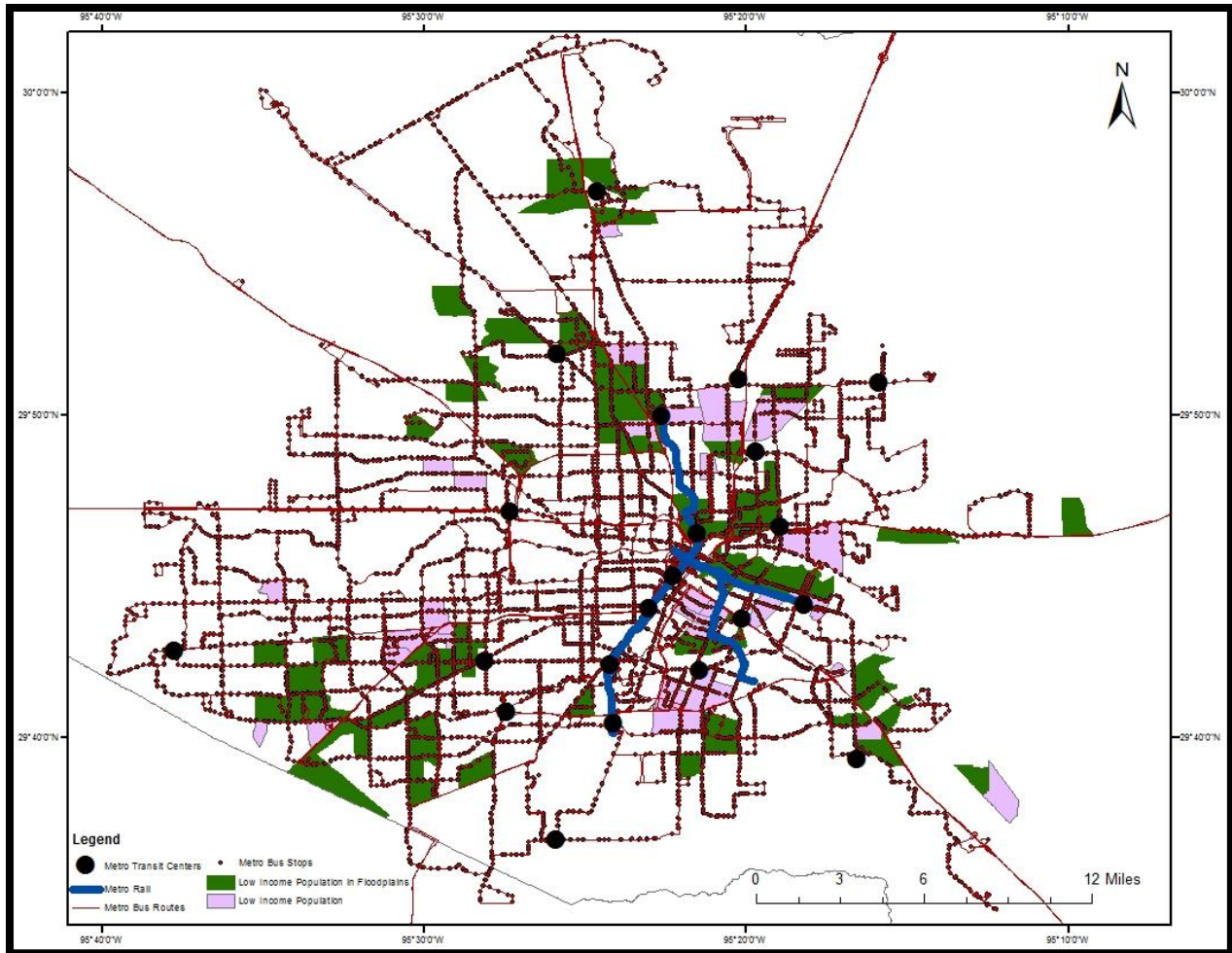
Figure 2- 3. The transit map of Houston Metro area highlighting low-income block groups and low-income block groups located in the 100 and 500-year floodplains. Median annual household income data acquired from U.S. census and displayed in block groups. The dark green colored block groups are areas with low income located within the floodplains.

However, there are limitations to using SLOSH output and GIS in this application. First, SLOSH output defines inundation area with no depth component making DEM raster calculations necessary to describe depth of inundation. This method may result in deriving inundation in areas that are not hydrologically connected and outside of what SLOSH represents as likely. The resolution of the DEM limits the scale at which analysis can be conducted. For instance, a higher-resolution LiDAR elevation model, if available for the particular study area, could resolve analysis of individual structures, roads, etc. As more LiDAR data is made available, more precise analysis can be conducted. Second, the SLOSH output does not incorporate SLR scenarios. Researchers would prefer to incorporate SLR scenarios to create custom MEOWs and MOMs, but custom SLOSH runs require software and resources not widely available to the public. For this reason, GIS is often employed to "add" SLR to the storm tide inundation layer through raster calculations (Frazier et al., 2010; Shepard et al., 2012; Tate and Frazier, 2013) assuming a linear relationship.

16
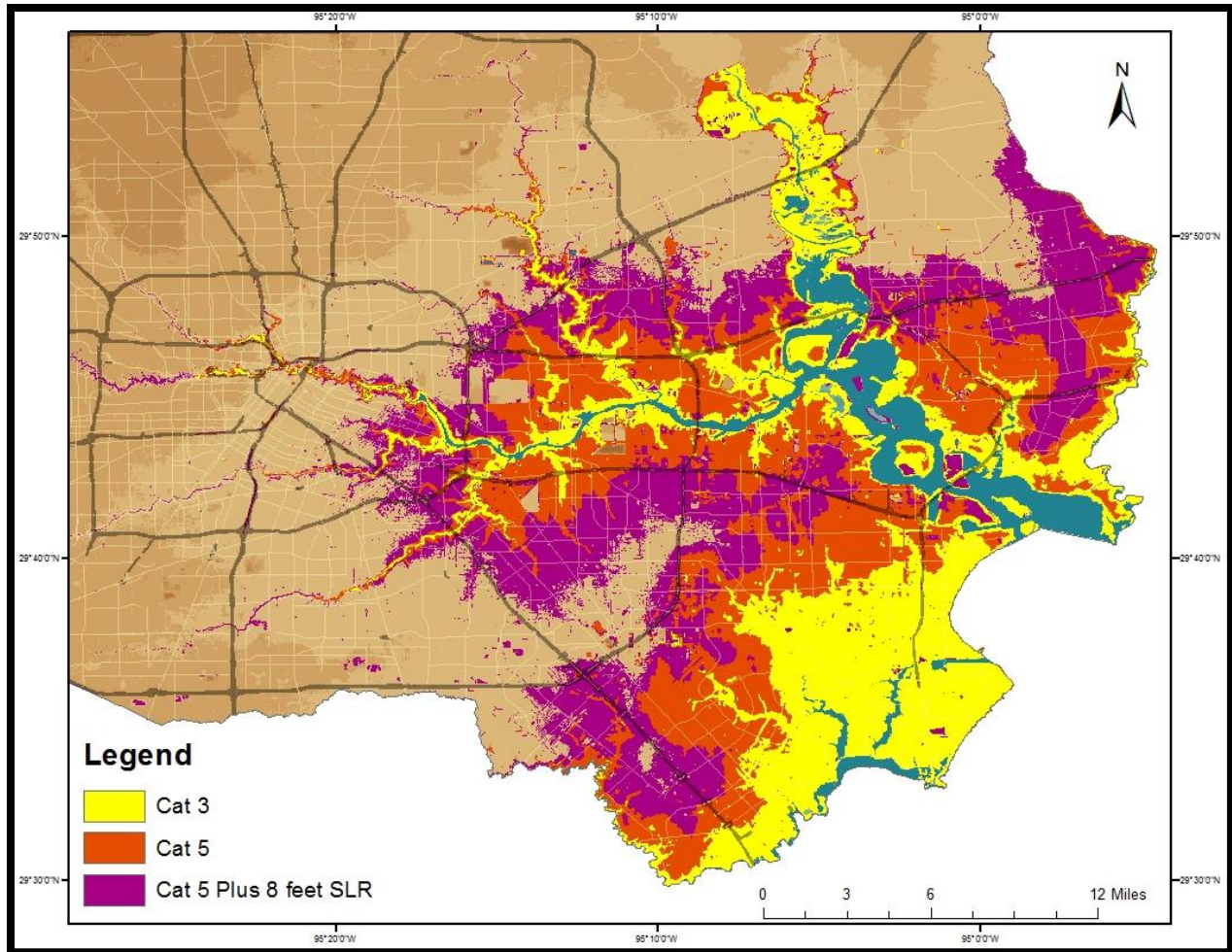
Figure 2- 4. The storm tide map of Harris County, TX, displaying inundation area for Cat 3 and Cat 5 hurricanes. The National Storm Surge Hazard Map was accessed through the National Hurricane Center and clipped to Harris County. SLR scenario of 8 feet displayed to demonstrate how the storm tide area increases with the rising sea.

This method may also result in identifying hydrologically disconnected inundation areas requiring further classification and removal from analysis and may lead to errors in the estimation of effects of SLR on inundation area and depth (Smith et al., 2010).

Efforts to protect vulnerable coastal cities with levees and seawalls may reduce the frequency of nuisance tidal flooding, but considerations should be taken to be sure these barriers can safeguard the population into the future. The effectiveness of levees in a warming climate will mostly depend on SLR, storm tide, and wave action. As seen in New Orleans in 2006 during Hurricane Katrina, storm tides can lead to levee breach with disastrous outcomes. When levees are overtopped by waves or storm surge, the landward side of the levee experiences a highly turbulent flow of water that leads to erosion. If the overtopping event is prolonged, the levee may decrease in height or fail altogether (Hughes 2009). In the aftermath of Hurricane Katrina, it was found that most of the earthen-levee destruction could be attributed to wave overtopping and storm surge overflow, and most of the damages were to the levee crest and the landward-side slopes (Anderson and Battjes, 2007).

17
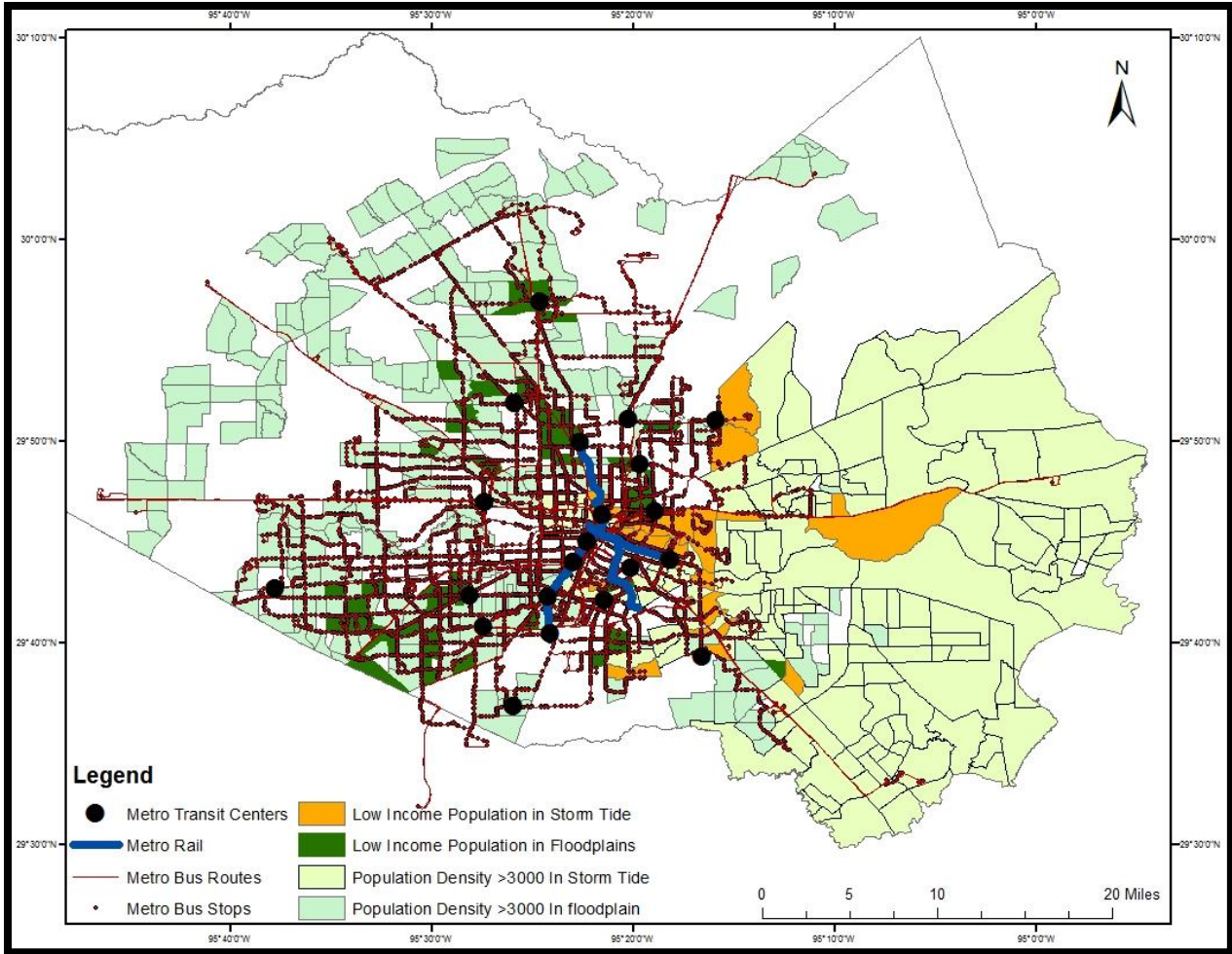
Figure 2- 5. The transit map of Harris County displaying the areas at risk of flooding and storm tide inundation along with highlighted areas of Median Household Income of less than $30,000.

With sea level rise predictions of up to 2.5 meters (Wuebbles et al., 2017) with the expectations of an increased proportion of major hurricanes (Emanuel et al., 2008), coastal communities are wise to reassess levee construction to prepare for the changing climate. Hurricanes pose a particular threat of flooding from the combination of high winds and rain with storm surge and low pressure. Levees constructed in the past may need to be raised higher or reassessed for durability and areas currently not leveed may need to be reevaluated for construction.

This study connects transit deserts with difficulties in evacuating transit-dependent populations. The following discusses the use of public transit in evacuation planning and how public transit operates during an emergency. Those who rely on public transport, notably those who have no vehicle, the elderly, and individuals with disabilities present a challenge for municipalities and emergency managers in the event of an evacuation. Busing has been used most commonly with emergency management agencies contracting local transit operators, school districts, and charter buses to provide transport and activating National Guard vehicles to supplement (Wolshon et al., 2005). These operations take place prior to the storm strike as roads

become inaccessible during the storm. Reviewing the evacuation procedures from Hurricanes Katrina and Rita in 2005, Litman (2006) found, with Katrina, a failure to plan to evacuate the ~200,000 transit-dependent residents with buses led to many being unable to evacuate while during Rita, one month after Katrina, a large number of buses were utilized to evacuate residents, but severe traffic congestion and heat led to ~90 deaths (Zachria and Patel, 2006). The poor outcomes of these evacuation strategies reveal a need to focus future plans on non-automobile evacuation and prioritize critical transportation assets during emergency procedures. The key to hurricane evacuation using public transportation is planning. Evacuation zones, pick-up and shelter locations, and routes (including number of trips) must be pre-planned and congestion reducing procedures such as contraflow need to be accounted for (Swamy et al., 2017). Although local transit authorities often do not have enough capacity to account for all transit-dependent residents, having a pre-existing transit grid that has been designed placing demand at all parcels represents a first step in planning to use public transit in equitable evacuation strategies (Allen, 2017).

2.6 Conclusion

Of the total population block groups in Harris County, 30.5% are densely populated, and among these block groups, 70% are within the FEMA 100-year and/or 500-year floodplain (Figure 2-2). The total number of income block groups with median annual household income of less than $30,000 represents only 5.3%. However, 66% of low-income block groups are within the FEMA 100-year and/or 500-year floodplain (Figure 2-3). This indicates many of the low-income population of Harris County live in areas that are susceptible to flooding during extreme rainfall events. People living in low-income communities rely on public transit in the case of an evacuation, and of the 1970 bus stops within these communities 66.4% are in the floodplain and will be unusable in the case of flooding.

Within the category 5 storm tide, 171 population block groups represent 8.8% of block groups in Harris County that are affected by maximum surge inundation. About half that number, 4.1%, are at risk from a category 3 storm tide (Figure 2-4). Of the 103 low-income block groups, 24 are within the inundation area. This represents 23.3% of the low-income block groups located within the storm tide. Of the 171 block groups affected by inundation, less than half, or 46.2% do not have any bus stops, light rail, or metro centers. This represents a high risk of being stranded by floodwaters in the event of a hurricane in those regions of Harris County. With future SLR scenarios included in the storm tide, the inundation area increases by 21% to cover an additional 36 high density population block groups in the worst-case scenario of 8 feet of SLR.

The transit desert map shows the supply of transit and demand by parcel with walking times to transit stops. The need for public transit is greater in low-income neighborhoods and many of these areas seen in Figure 2-5 are within the transit desert. Many areas in southwest Harris County have no transit access at all which leaves the population with little options for evacuation prior to a hurricane, and limits accessibility by responders due to lack of an existing transit grid.

The results establish the locations most exposed to flood risk from storm surge or extreme precipitation in Harris County and reveal that many low-income neighborhoods reliant on public transit are located within those flood hazard zones (Figure 2-5). Southeastern Harris County is particularly susceptible to storm surge inundation while possessing little in the means of public transit. Areas east and southeast of downtown Houston are prone to flooding by extreme rainfall events, while containing many low-income neighborhoods in need of public transit. Further study

of these areas, as well as any areas currently adjacent to the 100-year or 500-year floodplains will be considered to improve evacuation efforts to get residents to safety in the event of flooding.
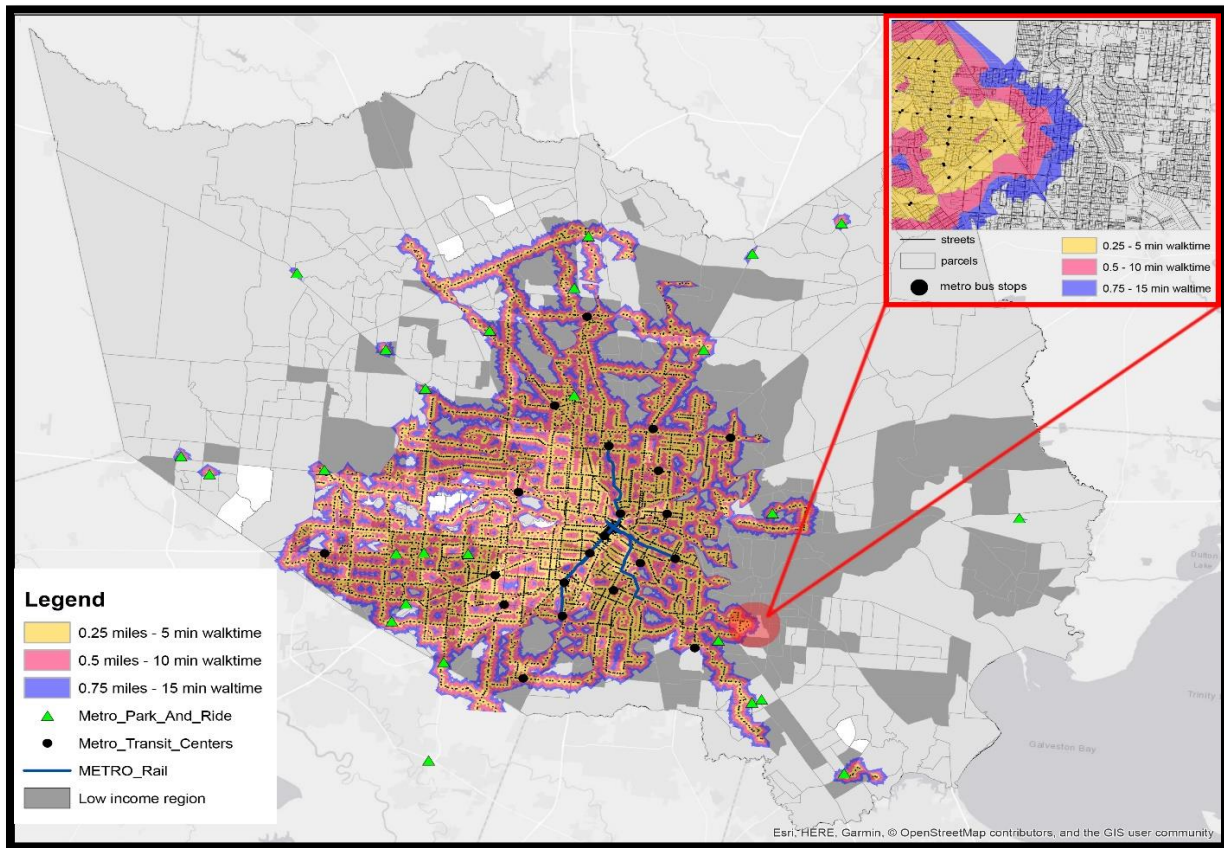
Figure 2- 6. The transit desert map of Harris County, TX, displays Houston Metro Transit information with walking times to available transit in minutes.

2.7 Future Outlook

To address transit availability and flooding susceptibility, communities should plan transit-oriented development, including affordable housing with multimodality of green infrastructure to build sustainability of the area. Efforts should be made to provide equitable access to transportation options including connected pedestrian, bicycle, and transit routes. Communities should develop guidelines and provide signage to follow during evacuation to help people reach transit. New technologies including electric vehicles should be supported and applied to design strategies to achieve lower carbon emissions. Municipalities and regions should develop climate resistance plans and require climate change analysis of existing laws and regulations. To address public health impacts of climate change in vulnerable communities, transit access to health care centers should be provided before, during, and after a disaster. Building in floodplains should be limited or prohibited to protect life, property, and floodplain function, and natural vegetative buffers should be protected and enhanced. Cities should promote mixed-income housing and mixed-use development that provides access to essential services and promotes green, permeable spaces. Buildings that exist in floodplains should have codes updated to require every first floor to be built of concrete to retain the structure when flooded.

References

AECOM, Michael Baker Jr., Inc., and Deloitte Consulting, LLP. (2013). The impact of climate change and population growth on the national flood insurance program through 2100. Federal Insurance and Mitigation Administration and Federal Emergency Management Agency. 6-1.

Allen, D. J. (2017). *Lost in the transit desert: Race, transit access and suburban form*. Routledge Press, 196 pp.

Anderson, C. F., and Battjes, J. A. (2007). The New Orleans Hurricane Protection System: What Went Wrong and Why: A Report by the American Society of Civil Engineers Hurricane Katrina External Review Panel. *Reston, American Society of Civil Engineers*.

Blake, E. S., and Zelinsky, D. A. (2018). National Hurricane Center Tropical Cyclone Report Hurricane Harvey. Publication AL092017. National Hurricane Center, Miami, FL, 3 – 12.

Dutton, A., Carlson, A. E., Long, A. J., Milne, G. A., Clark, P. U., DeConto, R., Horton, B. P., Rahmstorf, S., and Raymo, M. E. (2015). Sea-level rise due to polar ice-sheet mass loss during past warm periods. *Science, 349*(6244), aaa4019. 1 – 9.

Emanuel, K., Sundararajan, R., and Williams, J. (2008). Hurricanes and global warming: Results from downscaling IPCC AR4 simulations. *Bulletin of the American Meteorological Society*, *89*(3), 347-368.

Floodplain Management. Federal Emergency Management Agency. https://www.fema.gov/floodplain-management. Accessed June 28, 2018.

Frazier, T. G., Wood, N., Yarnal, B., and Bauer, D. H. (2010). Influence of potential sea level rise on societal vulnerability to hurricane storm-surge hazards, Sarasota County, Florida. *Applied Geography*, *30*(4), 490-505.

Harris, D. L. (1963). *Characteristics of the hurricane storm surge* (No. 48). Department of Commerce, Weather Bureau. 1-19.

Hallegatte, S., Green, C., Nicholls, R. J., and Corfee-Morlot, J. (2013). Future flood losses in major coastal cities. *Nature climate change, 3*(9), 802-806.

Hughes, S. A., and Nadal, N. C. (2009). Laboratory study of combined wave overtopping and storm surge overflow of a levee. *Coastal Engineering*, *56*(3), 244-259.

Jelesnianski, C. P. (1967). Numerical computations of storm surges with bottom stress. *Monthly Weather Review, 95*(11), 740-756.

Jelesnianski, C. P., Chen, J., and Shaffer, W. A. (1992). *SLOSH: Sea, lake, and overland surges from hurricanes*. NOAA Technical Report NWS 48, National Oceanic and Atmospheric Administration, U. S. Department of Commerce.

Jiao, J., and Dillivan, M. (2013). Transit deserts: The gap between demand and supply. *Journal of Public Transportation, 16*(3), 2.

Koenig, T. A., Bruce, J. L., O'Connor, J., McGee, B. D., Holmes Jr, R. R., Hollins, R., Forbes, B. T., Kohn, M. S., Schellekens, M. F., Martin, Z. W., and Peppler, M. C. (2016). Identifying and preserving high-water mark data (No. 3-A24). U.S. Geological Survey. 1-24.

Litman, T. (2006). Lessons From Katrina and Rita-What Major Disasters Can Teach Transportation Planners. *Journal of Transportation Engineering, 132*(1), 11-18.

Longuet-Higgins, M. S. (1983). Wave set-up, percolation and undertow in the surf zone. *Proceedings of the Royal Society of London. A. Mathematical and Physical Sciences, 390*(1799), 283-291.

McCallum, B. E., McGee, B. D., Kimbrow, D. R., Runner, M. S., Painter, J. A., Frantz, E. R., and Gotvald, A. J. (2012). *Monitoring storm tide and flooding from Hurricane Isaac along the Gulf Coast of the United States, August 2012*. US Department of the Interior, US Geological Survey.

Mukherjee, F., and Singh, D. (2020). Detecting flood prone areas in Harris County: A GIS based analysis. *GeoJournal*, *85*(3), 647-663.

O'Connor, J. E., and Costa, J. E. (2003). *Large floods in the United States: Where they happen and why*. U.S. Geological Survey Circular 1245. U.S. Geological Survey. 1 – 13.

Platzman, G. W. (1963). The dynamical prediction of wind tides on Lake Erie. In *The Dynamical Prediction of Wind Tides on Lake Erie* (pp. 1-44). American Meteorological Society, Boston, MA.

Shepard, C. C., Agostini, V. N., Gilmer, B., Allen, T., Stone, J., Brooks, W., and Beck, M. W. (2012). Assessing future risk: quantifying the effects of sea level rise on storm surge risk for the southern shores of Long Island, New York. *Natural hazards*, *60*(2), 727-745.

Smith, J. M., Cialone, M. A., Wamsley, T. V., and McAlpin, T. O. (2010). Potential impact of sea level rise on coastal surges in southeast Louisiana. *Ocean Engineering*, *37*(1), 37-47.

Stocker, T. F., Qin, D., Plattner, G. K., Tignor, M. M., Allen, S. K., Boschung, J., Nauels, A., Xia, Y., Bex, V., and Midgley, P. M. (2014). Climate Change 2013: The physical science basis. contribution of working group I to the fifth assessment report of IPCC the intergovernmental panel on climate change. 1034-1101.

Swamy, R., Kang, J. E., Batta, R., and Chung, Y. (2017). Hurricane evacuation planning using public transportation. *Socio-Economic Planning Sciences*, *59*, 43-55.

Tate, C., and Frazier, T. (2013). A GIS methodology to assess exposure of coastal infrastructure to storm surge & sea-level rise: a case study of Sarasota County, Florida. *Journal of Geography & Natural Disasters*, *1*, 2167-0587.

Wahl, T., Jain, S., Bender, J., Meyers, S. D., and Luther, M. E. (2015). Increasing risk of compound flooding from storm surge and rainfall for major US cities. *Nature Climate Change, 5(*12), 1093-1097.

What Impacts Storm Surge and How are These Impacts Generalized. National Hurricane Center. https://www.nhc.noaa.gov/surge/faq.php#2. Accessed June 28, 2018.

Wolshon, B., Urbina, E., Wilmot, C., and Levitan, M. (2005). Review of policies and practices for hurricane evacuation. I: Transportation planning, preparedness, and response. *Natural hazards review*, *6*(3), 129-142.

Wuebbles, D. J., Fahey, D. W., Hibbard, K. A., Dokken, D. J., Stewart, B. C., and Maycock, T. K. (2017) Climate Science Special Report: Fourth National Climate Assessment, Volume I. U.S. Global Change Research Program. 333 – 349.

Zachria, A., and Patel, B. (2006). Deaths related to Hurricane Rita and mass evacuation. *Chest, 130*(4), 124S.

Zachry, B. C., Booth, W. J., Rhome, J. R., and Sharon, T. M. (2015). A national view of storm surge risk and inundation. *Weather, climate, and society, 7*(2), 109-117.

Chapter 3: Assessing Relative Sea Level Rise in the Northern Gulf of Mexico for Effective Risk-Based Planning

Abstract
Communities along the Gulf coast of Texas and Louisiana face an increasing risk of flooding due to sea level rise associated with global warming that is expected to accelerate throughout the remainder of the century. Analysis of tide gauge observations between 1904 and 2021 indicate that the relative sea level rise rates at these locations exceed the sea level rise rate through regional subsidence. Therefore, it is necessary to include projections of relative sea level rise over time when assessing risk to lives, infrastructure, and ecosystems in this northern Gulf of Mexico. Many mathematical and statistical methods have been used to estimate trends and forecast relative sea level. In this study, Seasonal Autoregressive Integrated Moving Average (SARIMA) and Probabilistic Projections based on Monte-Carlo analysis, are applied to assess the utility of these methods in risk assessment. While SARIMA modeling provides a detailed forecast fit to the seasonality and linear trend of the observations in the short-term (10 years), it does not project acceleration. Additionally, this study finds Probabilistic Projections based on global climate model projections imposed on a background vertical land movement rate can include acceleration scenarios, but multiple scenarios must be included in risk assessment to account for various contributors to uncertainty. A case study in the region found Probabilistic Projections useful in producing flood maps that predict how much inundation will occur at a location decade by decade to 2100 under multiple acceleration scenarios.

3.1 Introduction
3.1.1 Relative Sea Level in the Gulf of Mexico
Global mean sea level (GMSL) has risen substantially since pre-industrial times with an increasing rate that, since 1900, has been faster than any other time over the past 2800 years (Kopp et al., 2016). The rate of sea level rise (SLR) at a particular coastal location can either increase or decrease relative to the global SLR rate based on non-climactic regional effects and vertical land movement. While the global trend of rising oceans is driven primarily by thermal expansion and melting of ice sheets and glaciers due to increasing global mean temperature, regional sea surface height (SSH) may be influenced by ocean circulation oscillations such as the Pacific Decadal Oscillation (PDO) and El Nino Southern Oscillation (ENSO; Sweet et al., 2017). Additionally, relative sea level (RSL) changes result from localized vertical land movement resulting from natural processes such as sediment compaction or glacial isostatic adjustment, as well as from anthropogenic influences on subsidence such as groundwater and hydrocarbon extraction (Sweet et al., 2017).

In the northern Gulf of Mexico (GOM), (Figure 3-1) RSL rise rate is greater than GMSL rise rate at all tide gauge locations. The gradual collapse of the forebulge of the Laurentide Ice Sheet contributes to subsidence through glacial isostatic adjustment, while depression of the lithosphere due to sediment loading from the Mississippi, Atchafalaya, and Brazos Rivers also contributes to the sinking land surface (Gonzales et al., 2006). Compaction of Holocene sediments in the northern GOM is another factor in the vertical land movement of the region (Ivins et al., 2007). Hydrocarbon and groundwater extraction, particularly during peak production rates from 1970-1979, contributes to subsidence along the Texas and Louisiana coasts (Gonzales et al., 2006).

Subsidence rates in the northern GOM were derived by Kolker et al. (2011) by using the tide gauge records of Grand Isle, LA, and Galveston, TX, located in sedimentary environments and comparing them to the Pensacola, FL, tide gauge located on a stable carbonate platform with little vertical land movement. The long-term subsidence rates (1947-2006) were determined to be 7.59 ± 0.23 mm/yr at Grand Isle and 4.71 ± 0.21 mm/yr at Galveston, while breaking the rates into short terms reveals that subsidence rates at both locations were highest during the period of 1959-1974 when subsurface fluid withdrawal was at its peak, suggesting a strong anthropogenic influence in the region (Kolker et al., 2011).
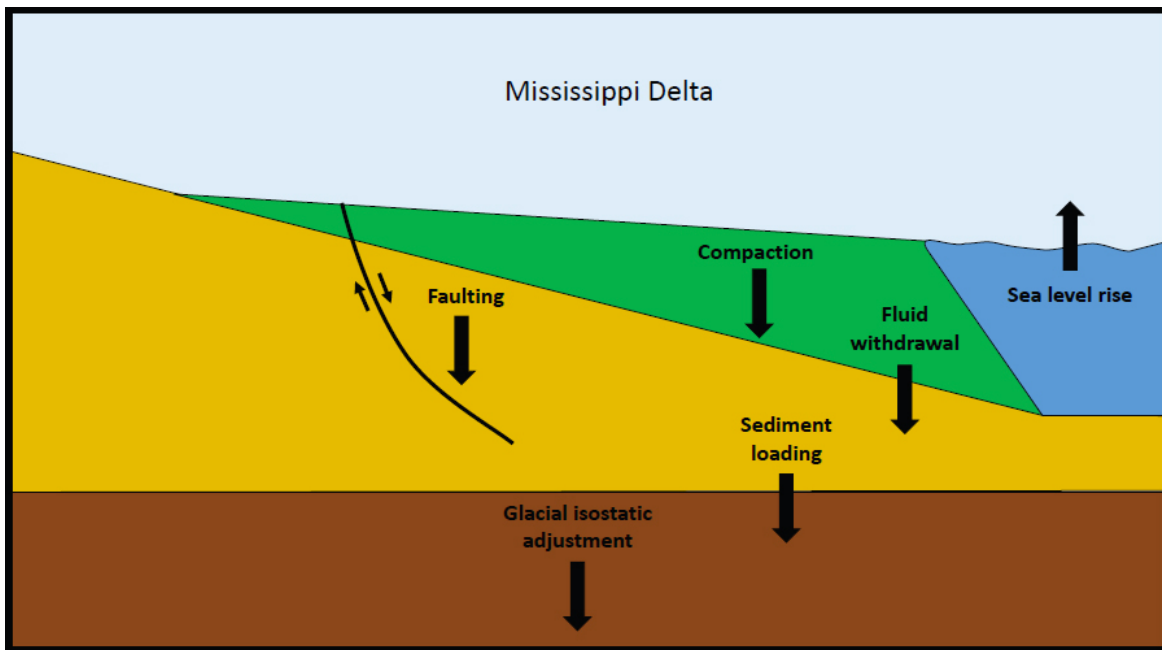
Figure 3- 1. Processes driving subsidence in the Mississippi Delta region of the GOM. (Figure from National Academic Press 2018).

Although riverine sediment loading can contribute to subsidence, studies indicate these sediments are necessary to sustain and build the coastal wetlands. In the Mississippi delta, sediment loads have been reduced up to 50% over the past few centuries due to building of dams and levees which leaves the area vulnerable to submersion from SLR (Blum and Roberts, 2009).

3.1.2 Modeling and Forecasting of Relative Sea Level Rise

Accurate forecasts of RSL rise for selected locations have been desired by planners and policy makers and is an important topic of research that has been explored in several ways. However, due to uncertainties in ice sheet melting dynamics and future greenhouse gas emission rates, forecasts of RSL must be presented as a range of probable results. For risk mitigation and adaptation in coastal communities, it is important to include these uncertainties to ensure that high-risk, low probability events are not underestimated.

The first approach discussed here is based on derived location-specific RSL scenarios by using Monte-Carlo resampling of gridded climate data from Perrette et al. (2013) and Kopp et al. (2014) and applied vertical land movement rates derived from GPS and tide gauge platforms (Hall et al., 2016; Sweet et al., 2017; Figure 3-3). The processes explored by these studies include ice sheet mass changes, glacier mass changes, thermal expansion, atmosphere-ocean

dynamics, steric and dynamic oceanographic processes, land-water storage, glacial isostatic adjustment, tectonics, and sediment compaction (Sweet et al., 2017). The non-climatic background rate is analyzed as the sum of three processes. Kopp et al. (2013) defines the three processes as: (1) a globally uniform sea level rise, (2) regional linear processes, and (3) regionally non-linear processes. Since vertical land movements are considered linear processes, the background RSL rate is determined from that process using a Gaussian process regression method (Kopp et al., 2014 supplementary information) to separate the three components. Other climatic processes included in the determination of RSL are land water storage, ice sheet melting, glaciers, and icecaps (GIC), surface mass balance (SMB), static-equilibrium, and oceanographic processes, all of which are derived from global climate (GCM) and other models or literature. A schematic of the processes adapted from Kopp et al. (2014) is shown in Figure 3-2.
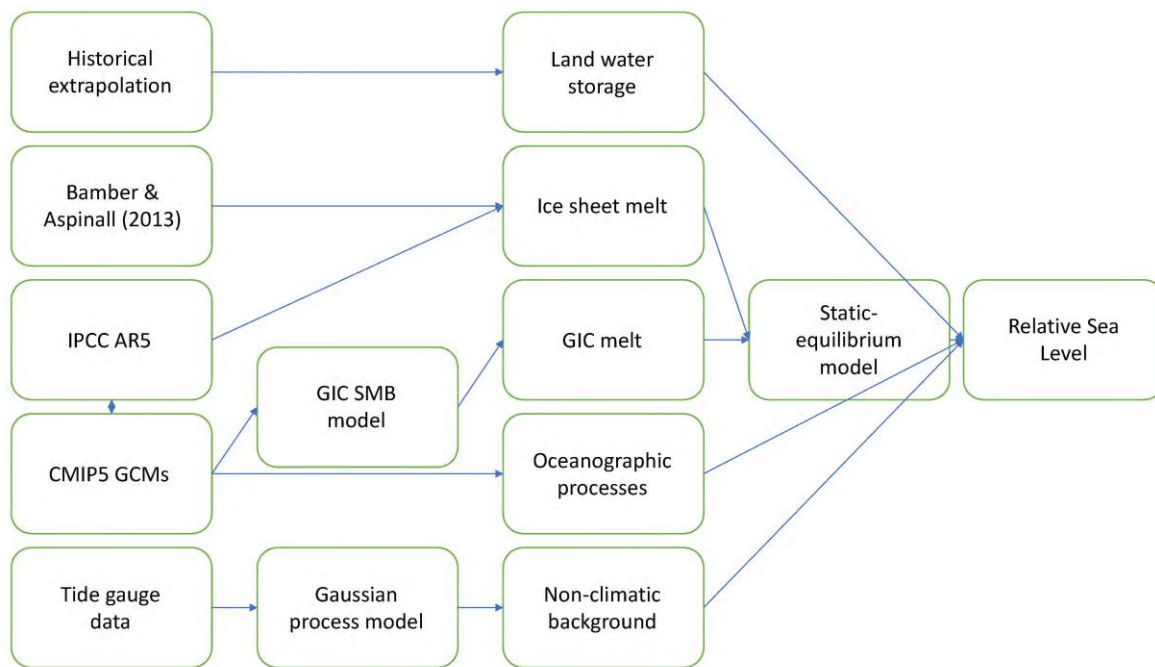
Figure 3- 2. Flow-chart schematic for processes used to derive localized RSL projections. Adapted from Kopp et al. (2014).

Probabilities of the different scenarios are useful for planning for the future with uncertain magnitude of sea level rise. Since satellite altimetry measures the current global rate of sea level change at 3mm/year, 0.3 meters by 2100 is used for the "Low" scenario while Intermediate-Low (0.5 m), Intermediate (1.0 m), Intermediate-High (1.5 m), High (2.0 m), and Extreme (2.5 m) are consistent with 0.5-meter increments used by Hall et al. (2016), Kopp et al. (2016), and Sweet et al. (2017). Radiative forcing from greenhouse gas concentrations is represented by Representative Concentration Pathways (RCPs) adopted by the Intergovernmental Panel on Climate Change (IPCC) for the fifth Assessment Report (AR5). Although the scenarios are placed at simple intervals, they do relate different likelihoods of RCP2.6, RCP4.5, and RCP8.5 as modeled by Coupled Model Intercomparison Project Phase 5 (CMIP5) global climate model. The RSL changes that arise locally under each GMSL scenario occur due to climate-related processes as well as non-climatic vertical land movement processes and can be expressed as

$$\Delta RSL\ (x,t) = Climatic\ \Delta RSL\ (x,t) + Background\ RSL\ rate\ (x)(t-t_0)$$

where ΔRSL, the RSL change relative to RSL at time t_0 in the scenario, is defined for locations x and times t, and background (non-climatic) rate is assumed to be linear with time (Sweet et al., 2017). The rates of GMSL rise derived from the 2100 scenario heights used for projections (Figure 3-3) can be seen in Table 3-1 with interpretations of the scenarios in Table 3-2 explaining the connections between the scenarios and the RCP experiments.

Table 3-1. GMSL rise rates relative to scenario heights by 2100 (Sweet et al., 2017).

GMSL Scenario Rise Rates (mm/year)	2010	2020	2030	2040	2050	2060	2070	2080	2090
Low	3	3	3	3	3	3	3	3	3
Intermediate-Low	4	5	5	5	5	5	5	5	5
Intermediate	5	6	7	9	10	12	13	14	15
Intermediate-High	5	7	10	13	15	18	20	22	24
High	6	8	13	16	20	24	28	31	35
Extreme	6	10	15	20	25	30	35	40	44

Table 3-2. Interpretations of GMSL rise scenarios from U.S. Interagency Sea Level Rise Task Force (Sweet et al. 2017a). Probabilistic projections of GMSL for RCP2.6, RCP4.5, and RCP8.5 scenarios were applied to the site-specific RSL (Figure 3-2). Note that relative uncertainties used in risk assessment of Sweet et al. (2017).

Scenario	Interpretation
Low	Continuing current rate of GMSL rise, as calculated since 1993 from satellite altimetry. Low end of *very likely* range under RCP2.6
Intermediate-Low	Modest increase in rate. Middle of *likely* range under RCP2.6 Low end of *likely* range under RCP4.5 Low end of *very likely* range under RCP8.5
Intermediate	High end of *very likely* range under RCP4.5 High end of *likely* range under RCP8.5 Middle of *likely* range under RCP4.5 when accounting for ice cliff instability
Intermediate-High	Slightly above high end of *very likely* range under RCP8.5 Middle of *likely* range under RCP8.5 when accounting for ice cliff instability
High	High end of *very likely* range under RCP8.5 when accounting for ice cliff instability
Extreme	Consistent with estimates of physically possible "worst case"
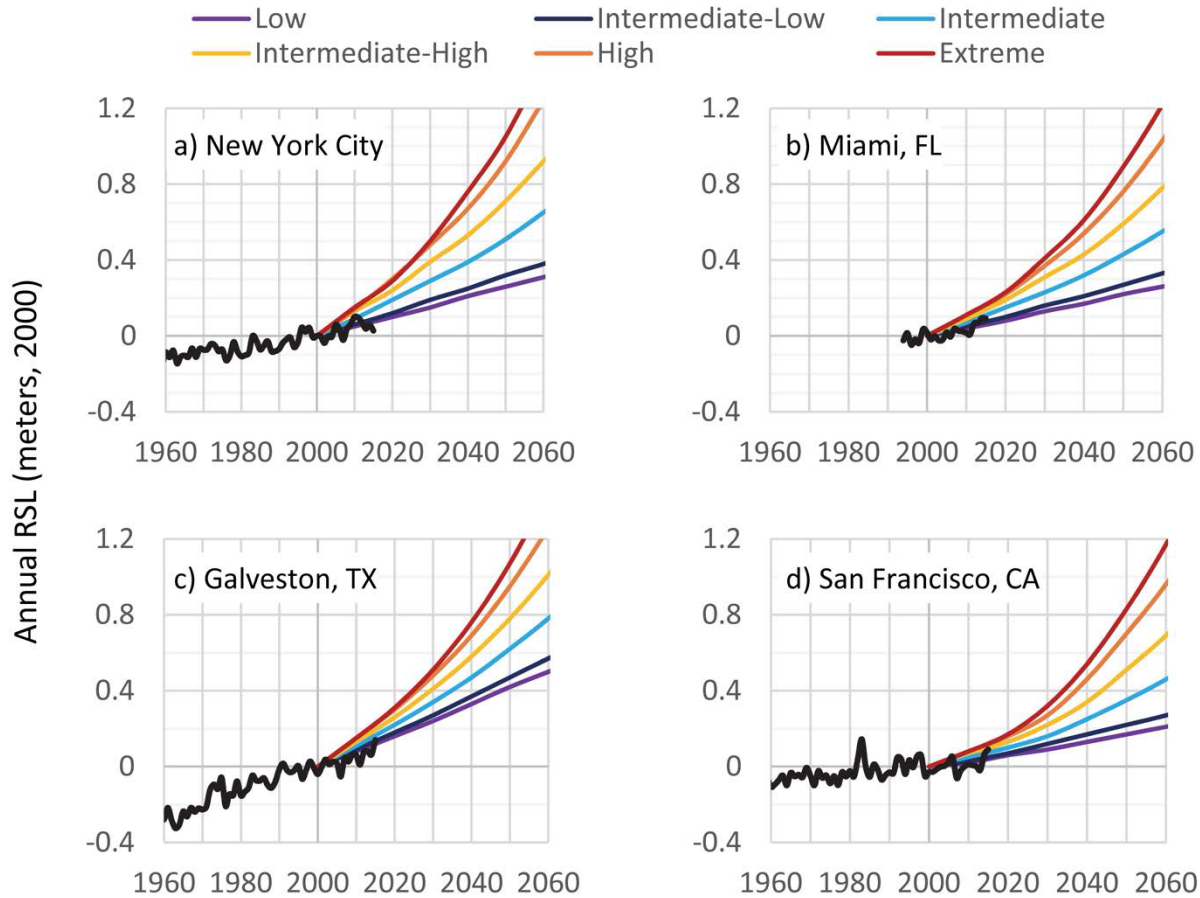
Figure 3- 3. The RSL rise scenarios for locations by Sweet et al. (2017) with the median-value RSL under the six scenarios (Low, Intermediate-Low, Intermediate, Intermediate-High, High, and Extreme). Tide gauge observations are shown (in black) relative to the year 2000.

The second approach used in this study follows the approach of Srivastava et al. (2016) who combined satellite altimetry datasets with exponential smoothing state space models (ESMs) and seasonal autoregressive integrated moving average (SARIMA) to forecast SLR in the Arabian Sea (Figure 3-4). The SARIMA model has been applied to the South China Sea also using satellite altimetry datasets (Fernandez et al., 2017) as well as Manila South Harbor using tide gauge datasets (Fernandez et al., 2018). These methods have been shown to be statistically significant for short-term RSL forecasts but lack the ability to predict future acceleration of RSL rise rates.

Nonlinear smoothing methods have been applied to SLR using Monte Carlo singular spectrum analysis (MC-SSA) (Jevrejeva et al., 2008) and modified Lowess smoothing (Foster and Brown, 2014) with a 30-year window. These methods can estimate the rate of sea level change and indicate an acceleration of said rate in the 21st century. The 30-year window fitted model using Lowess smoothing was compared by Foster and Brown (2014) to the previous sea level reconstruction of Church and White (2011) that indicates a good model fit for global SLR (Figure 3-5).
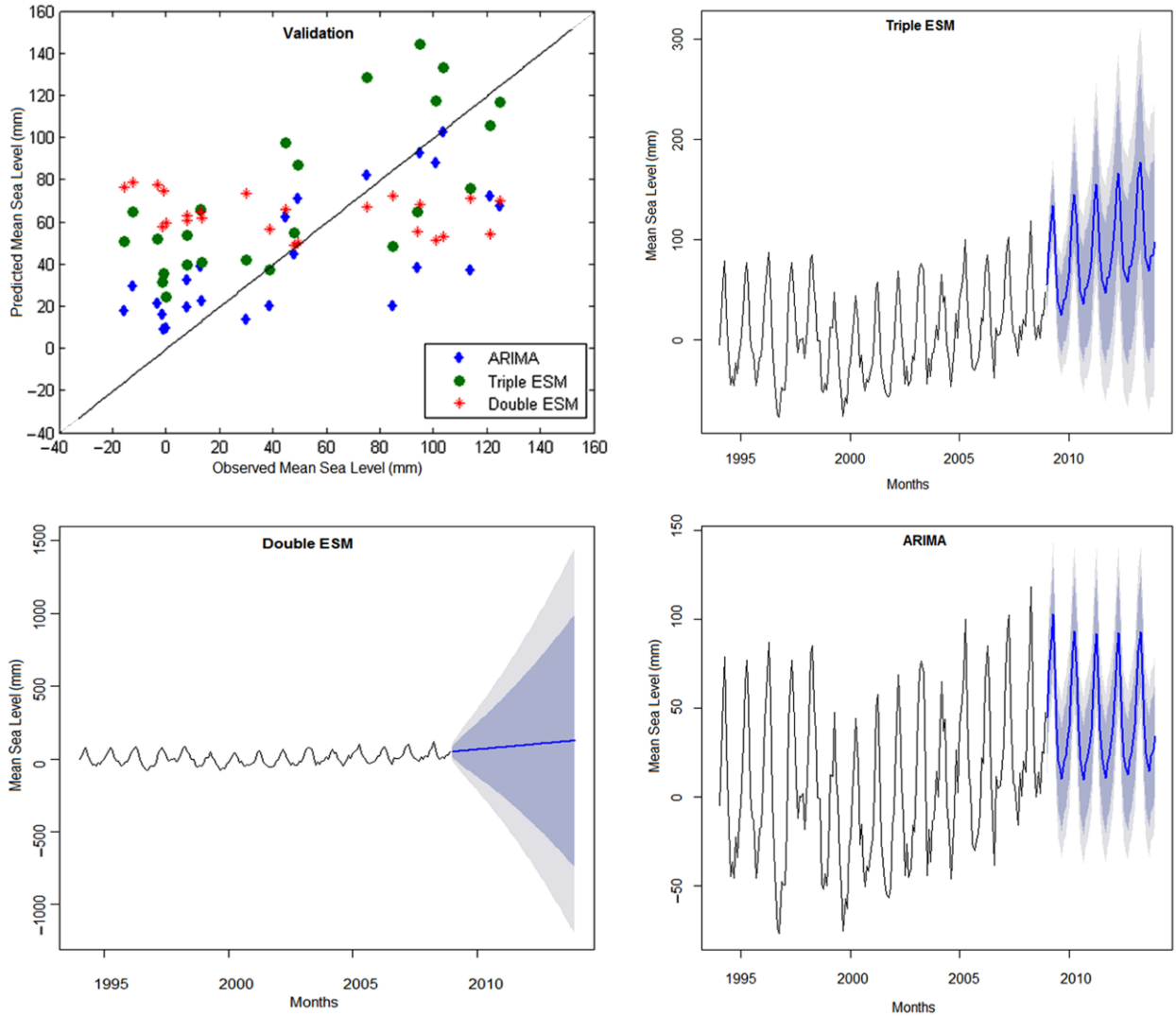
Figure 3- 4. Scatter plot and forecast results for Arabian Sea level rise 1994–2010 from three modelling approaches with prediction intervals. (a) Scatter plot for validation datasets; (b) double exponential smoothing state space model (ESM); (c) triple ESM; and (d) autoregressive integrated moving average (ARIMA). Figure from Srivastava et al. (2016).

Estimating projected SSH for a specific region can be useful to those planning infrastructure improvements on the city or state level in areas at risk of coastal flooding and storm surges. Based on tide gauge data, Galveston, as well as other locations along the northern GOM, has a RSL rise rate (~6.51 mm/ year) of more than twice the rate of GMSL rise (~3.00 mm/ year). Consequently, projecting RSL is more appropriate for this area than projections of GMSL that may underestimate the impacts of SLR locally. For planning purposes, it may be necessary to assess multiple scenarios of RSL projections as there is great uncertainty in SLR rates into the future involving the dynamics of the Greenland and Antarctic ice sheets that are not yet fully understood.
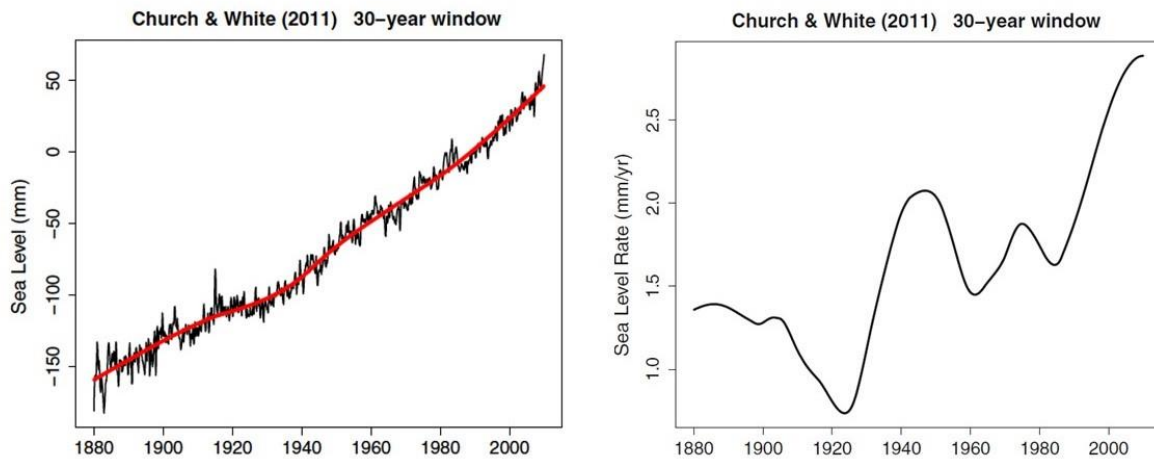
Figure 3- 5. Modified Lowess smooth (red line) with a 30-year window fit to the global sea level reconstruction of Church and White (2011) and the estimated rate of change ("velocity") from Foster and Brown indicating an acceleration of GMSL rise (2014).

3.2 Hypothesis and Objective

Due to local geologic processes of subsidence and the acceleration of global sea level rise, coastal flood risk assessments on the Texas and Louisiana Gulf coast can be improved by analyzing relative, rather than global, sea level forecasts that capture the acceleration of sea level rise. Because future acceleration scenarios are uncertain due to climate variability and anthropogenic influences on radiative forcing (e.g., greenhouse gas emissions), a forecasting methodology is required that provides a range of possible outcomes for use in risk assessment.

The goal of this study is to assess coastal flood risks on the Texas and Louisiana Gulf coast caused by local geologic processes (e.g., subsidence by sedimentary load from rivers) and accelerating rates of global sea level rise. Northern GOM relative SLR appears to be substantially faster than the globally averaged rate based on tide gauge measurements and previous publication. For this purpose, we utilize SARIMA and probabilistic RSL projections to provide a flood planning and risk assessment for communities along the northern GOM. Results from the analysis of these two methodologies at the specific locations of tide gauge station will be compared and provide a case study in assessing coastal flood risks. A range of possible future flood risks will be spatially and temporally mapped by the overlay analysis. Thus, regional SLR projections provide a more effective assessment of coastal flood risk compared to the global SLR estimates. This research contributes to better understanding of regional and temporal differences and uncertainties in future RSL that could be practical guiding tools for stakeholders and decision makers.

3.3 Methodology
3.3.1 Data

Monthly mean sea level (MSL) data with seasonality removed was collected from the National Oceanic and Atmospheric Administration (NOAA) tides and currents (https://tidesandcurrents.noaa.gov/sltrends/) for all Texas tide gauge locations as well as for Grand Isle, Louisiana for use in the probabilistic projections. For SARIMA modeling, monthly MSL data including seasonality was collected from the Permanent Service for Mean Sea Level

(PSMSL) for all tide gauge locations in Texas as well as Grand Isle, Louisiana. Satellite altimetry measurements of mean sea level of the GOM were gathered from the NOAA Laboratory for Satellite Altimetry and consist of measurements initiated by TOPEX and Poseidon in 1993 and continued to the present with the JASON project.

3.3.2 Probabilistic Projections

Global positioning system (GPS) data interpolated to 1° x 1° horizontal geographic grid derived by Sweet et al. (2017) were combined with NOAA tide gauge data to provide RSL trends for the northern GOM at specific tide gauge locations. The background SLR scenarios based on the work of Kopp et al. (2016) and Sweet et al. (2017) that improved upon previous projections by Parris et al. (2012) were incorporated with yearly averaged tide gauge data trends that include vertical land movement to provide RSL rise scenarios beyond the global average. Relative sea level rise (RSLR) scenarios for the future were derived from background GMSL changes based upon greenhouse-gas emissions represented by RCPs (Table 3-1). RSLR scenarios were calculated by decade based on the acceleration by decade determined by previous studies (Perrette et al., 2013; Kopp et al., 2014; Hall et al., 2016; Sweet et al., 2017) Using the NOAA tide gauge observations relative to the 1991-2009 datum epoch (centered at 2000), scenarios were applied for all stations along the northern GOM.

3.3.3 ARIMA and its seasonal version SARIMA

ARIMA models are used to forecast time series data based on correlation of observed values in the series. ARIMA is made up of two terms, the autoregressive (AR) term represents the lags of the differenced series, and the moving average (MA) term represents the lags of the forecast errors (Srivastava et al., 2016). ARIMA models typically utilize three terms notated as p, d, q where p is the number of autoregressive terms, d is the number of differences, and q is the number of forecast error lags. The non-seasonal ARIMA (p, d, q) prediction is represented by the following equation (eq. 3.1; Box et al., 2015):

$$\phi(L)(1-L)^D y_t = c + \theta(L)\varepsilon_t \tag{3.1}$$

where ε_t is a white noise process with variance σ^2 and zero mean, c is a function representing random walk with drift, L is the backshift operator, and ϕ and θ are polynomials of order p and q, respectively (Srivastava et al., 2016). Equation (2.1) is modified to a seasonal version named SARIMA (eq. 3.2), when seasonality is detected in the time series, otherwise known as multiplicative ARIMA (p, d, q)(P, D, Q)$_m$,

$$\Phi(L)^m \phi(L)(1-L^m)^D (1-B)^d y_t = c + \Theta(L^m)\theta(L)\varepsilon_t \tag{3.2}$$

where Φ and Θ are polynomials of orders P and Q, respectively. P and Q refer to the autoregressive and moving average terms for the seasonal part of the ARIMA model. D represents the order of seasonal-differencing and m is the period of seasonality (Srivastava et al., 2016; Box et al., 2015).

The Box-Jenkins method for time series forecasting was followed utilizing tools in MATLAB (2019a) to generate a SARIMA model of tide gauge data for forecasting RSL. Assessing the parameters, (p, d, q)(P, D, Q)$_m$, of the SARIMA model was executed through qualitative analysis of plots of the autocorrelation function (ACF) and partial autocorrelation function (PACF). The

ACF shows the correlation of sequential observations, i.e., the correlation between the first and second observation, while the PACF shows the correlation of ordered pairs and the observations between them, i.e., the correlation between the first and third observation while considering the second observation (Fernandez et al., 2017). In the case of monthly MSL used in this study, a seasonal first differencing of period 12 was applied to the data and a SARIMA $(1,0,0)(0,1,1)_{12}$ model was identified through plots of the ACF and PACF. Diagnostic statistics were used to determine the goodness of fit of the model and included the Akaike Information Criterion (AIC) and Bayesian Information Criterion (BIC), as well as residual diagnostics utilizing a residual histogram, quantile-quantile plot, ACF and PACF. A Ljung-Box Q-test was performed to determine if the model was fit for forecasting. The SARIMA model was used to produce 5 and 10-year forecasts that include the seasonal trends for all tide gauge locations analyzed in this study. All forecasts were modeled on the observed historical data excluding the most recent 24 month-period which was used to validate the model.

3.4 Results
3.4.1 RSL Rates and Probabilistic Projections

RSL rates obtained from long-term tide gauge data (Figure 3-6) are displayed in Table 3-3 and reveal that the rates along the northernmost locations of the GOM (Grand Isle, Sabine Pass, Galveston) are substantially higher than the GMSL rise rates measured by satellite altimetry, and all locations observe a rate at least slightly higher than the global rate.

Table 3-3. Relative Sea Level Rise Rates at Tide Gauge Locations of the Northern GOM.

Tide Gauge Station	Relative Sea Level Rise Rate (mm/yr)
Grand Isle, LA	9.08 ± 0.42
Sabine Pass, TX	5.86 ± 0.74
Galveston Pier 21, TX	6.51 ± 0.22
Galveston Pleasure Pier, TX	6.62 ± 0.69
Freeport, TX*	4.43 ± 1.05
Rockport, TX	5.62 ± 0.48
Corpus Christi, TX	4.65 ± 1.06
Port Mansfield, TX	3.19 ± 0.73
Port Isabel, TX	4.00 ± 0.33
Padre Island, TX	3.48 ± 0.75

*Data contains vertical datum inconsistencies and was not used for further study.

Background RSL rates derived from GPS and tide gauge observations used in probabilistic projections for all tide gauge locations along the Texas and Louisiana coasts are shown in Figure 3-7. Comparison with Table 3-3 indicates that the high rates of RSL observed at Grand Isle, Sabine Pass, and Galveston are due mostly to this background vertical land movement rate.
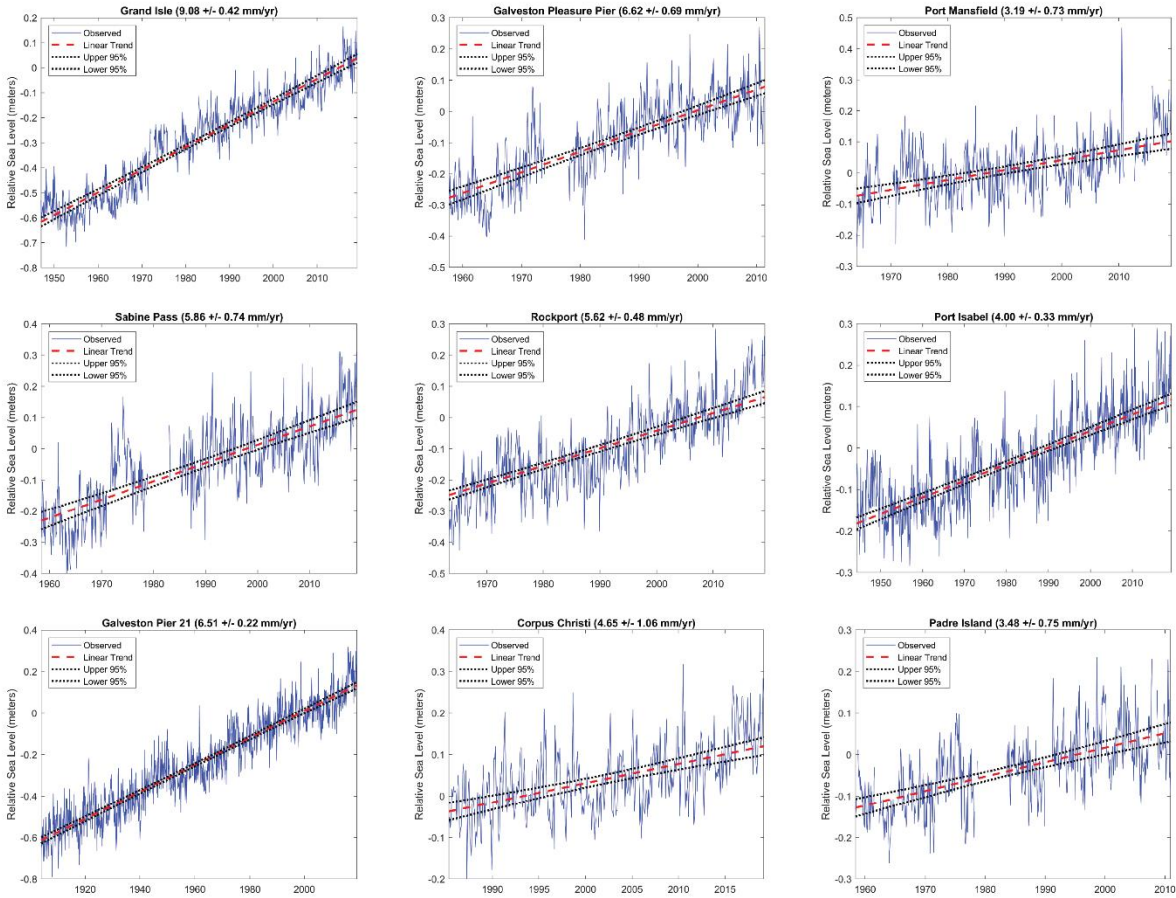
Figure 3- 6. Plots of NOAA tide gauge observations and RSL rates (linear trend) for stations along the Texas and Louisiana coasts.

The map of background RSL rates (Figure 3-8) interpolated for geospatial analysis highlights the locations in the GOM that have the highest vertical land movement rates. The locations that have the highest rates are areas that have historically received the most sediment load. Therefore, subsidence in these areas is dominated by lithospheric loading and sediment compaction. The tide gauge location with the highest RSL rates is Grand Isle, located near the Atchafalaya River delta, an area that has historically received a large sediment load (Ivins et al., 2007; Blum and Roberts, 2009).
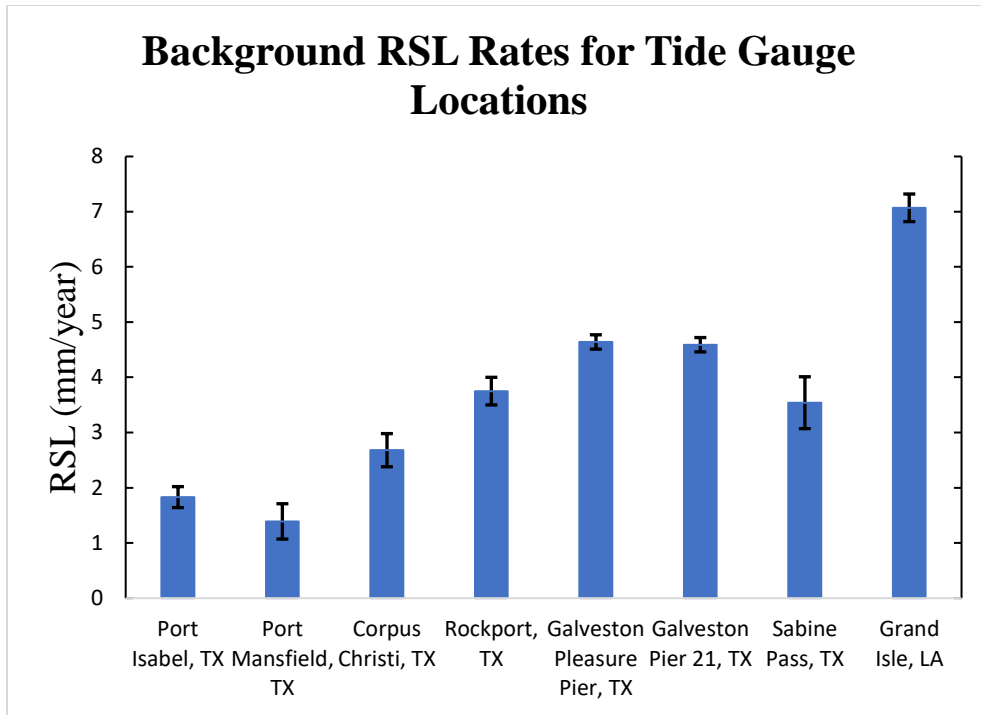
Figure 3- 7. Background RSL rates derived from tide gauge and vertical land movement data as reported by Sweet et al. 2017.
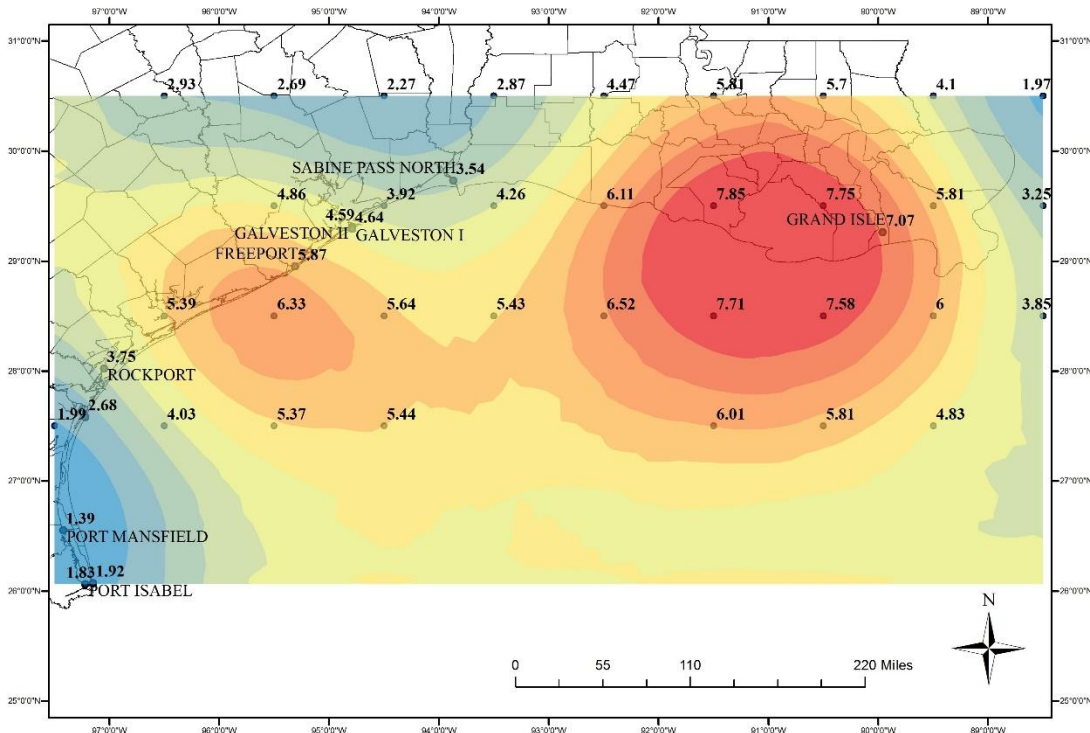
Figure 3- 8. Map displaying the combined GPS and tide gauge derived non-climatic background RSL rates (mm/year) interpolated to visualize areas of greatest downward vertical land movement.

Table 3-4. Relative Sea Level Projections at Tide Gauge Locations of the Northern GOM

Tide Gauge Location	Relative Sea Level (m) Projections for Low, Intermediate (Int) and Extreme (Ext) Scenarios											
	2040			2060			2080			2100		
	Low	Int	Ext	Low	Int	Ext	Low	Int	Ext	Low	Int	Ext
Grand Isle, LA	0.43	0.57	0.85	0.65	0.93	1.60	0.86	1.34	2.55	1.05	1.79	3.78
Sabine Pass, TX	0.29	0.43	0.71	0.44	0.71	1.39	0.57	1.05	2.27	0.69	1.43	3.41
Galveston Pier 21, TX	0.33	0.47	0.76	0.51	0.79	1.47	0.66	1.15	2.37	0.80	1.55	3.53
Galveston Pleasure Pier, TX	0.34	0.48	0.77	0.51	0.79	1.47	0.66	1.15	2.37	0.80	1.55	3.53
Rockport, TX	0.30	0.44	0.72	0.46	0.74	1.40	0.59	1.08	2.30	0.72	1.46	3.46
Corpus Christi, TX	0.26	0.40	0.68	0.39	0.67	1.34	0.50	0.99	2.20	0.61	1.37	3.35
Port Mansfield, TX	0.21	0.35	0.62	0.31	0.59	1.27	0.40	0.90	2.12	0.48	1.24	3.24
Port Isabel, TX	0.22	0.36	0.63	0.34	0.62	1.30	0.44	0.94	2.16	0.52	1.28	3.29
Padre Island, TX	0.23	0.37	0.61	0.35	0.63	1.16	0.44	0.94	1.90	0.53	1.29	2.82

Probabilistic projections results for all tide gauge locations are presented in Figure 3-9 showing the median values for all six scenarios seen in Table 3-2 and Table 3-4 presents the values for 20-year increments for the low, intermediate, and extreme scenarios.

3.4.2 Application of SARIMA to the northern GOM

The time series from tide gauge observations of monthly MSL at Galveston Pleasure Pier (Figure 3-10) was utilized to fit the SARIMA model by applying tools in MATLAB (2019a). A 12-month seasonal cycle can be observed in Figure 3-10 with sea level highest in September and lowest in January. The ACF of the monthly MSL time series (Figure 3-11) indicates the need for differencing of the time series to remove the seasonal trend to fit the data.

The autocorrelation, seen in Figure 3-11, repeats every twelfth lag which confirms the 12-month seasonality and the need for first seasonal differencing with a 12-month period. With the seasonal trend removed, the differenced time series ACF and PACF (Figure 3-12) suggests a 12-month seasonality with a moving average order of 1. Assessing the parameters, $(p, d, q)(P, D, Q)_m$, of the model, the need for a first seasonal differencing dictates $D = 1$ while the seasonality indicates the need for, $Q = 1$, and $m = 12$. Therefore, a SARIMA $(1,0,0)(0,1,1)_{12}$ was tested for goodness of fit to the original time series as seen in Figure 3-13.
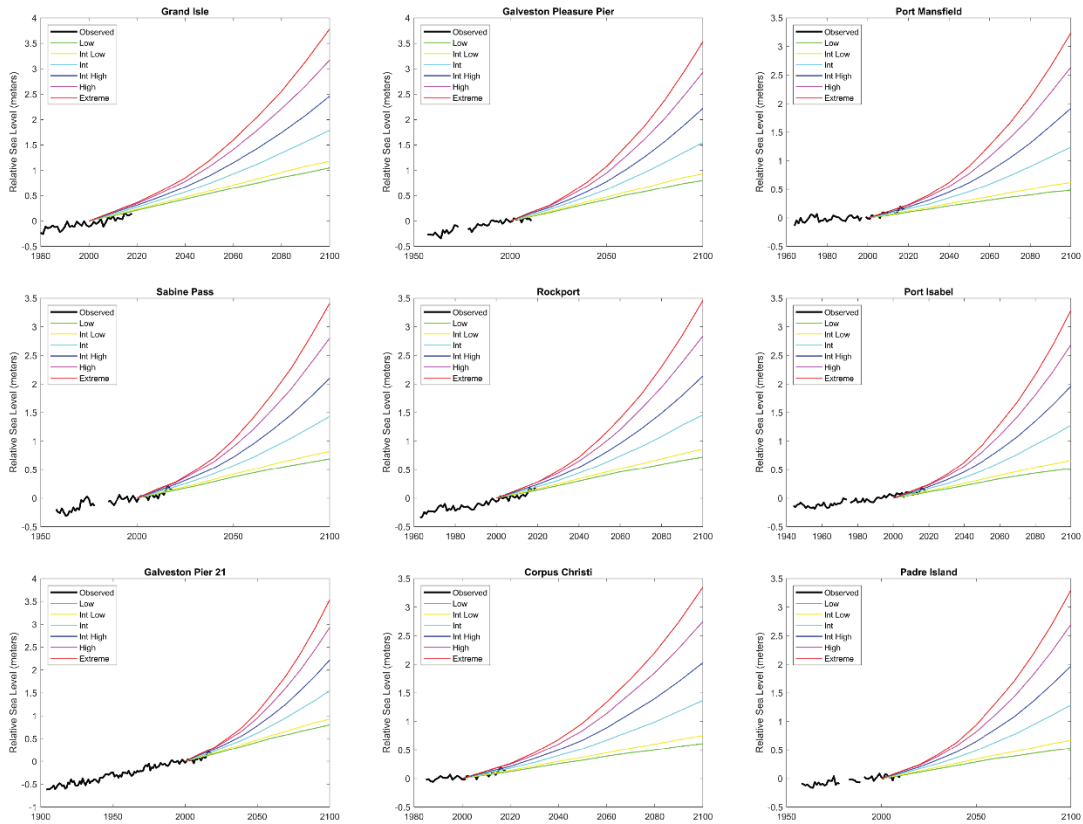
Figure 3- 9. Probabilistic RSL projections for tide gauge locations along the northern GOM for the six RCP-based scenarios as seen in Table 3-2.
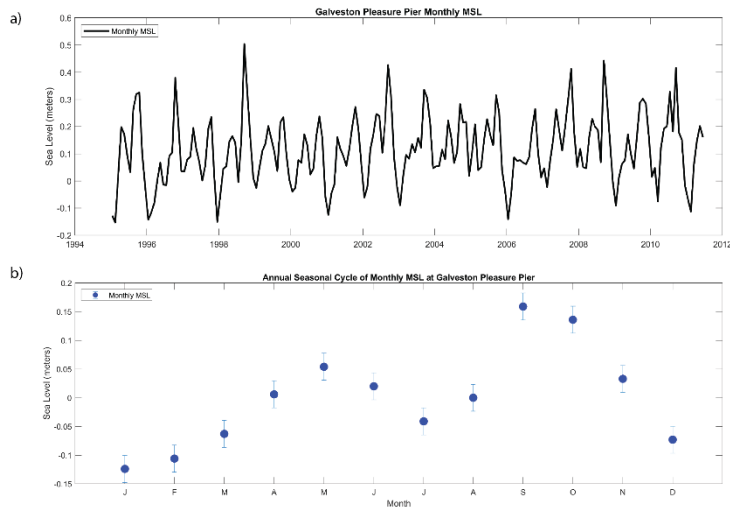
Figure 3- 10. (a) The tide gauge time series of monthly mean sea level observations from Galveston Pleasure Pier from 1995 to 2011. The time series was used to develop the SARIMA model for forecasting RSL for the northern GOM. (b) The annual seasonal cycle of monthly mean sea level at Galveston Pleasure Pier from NOAA is similar to other tide gauge locations in the northern GOM.

36
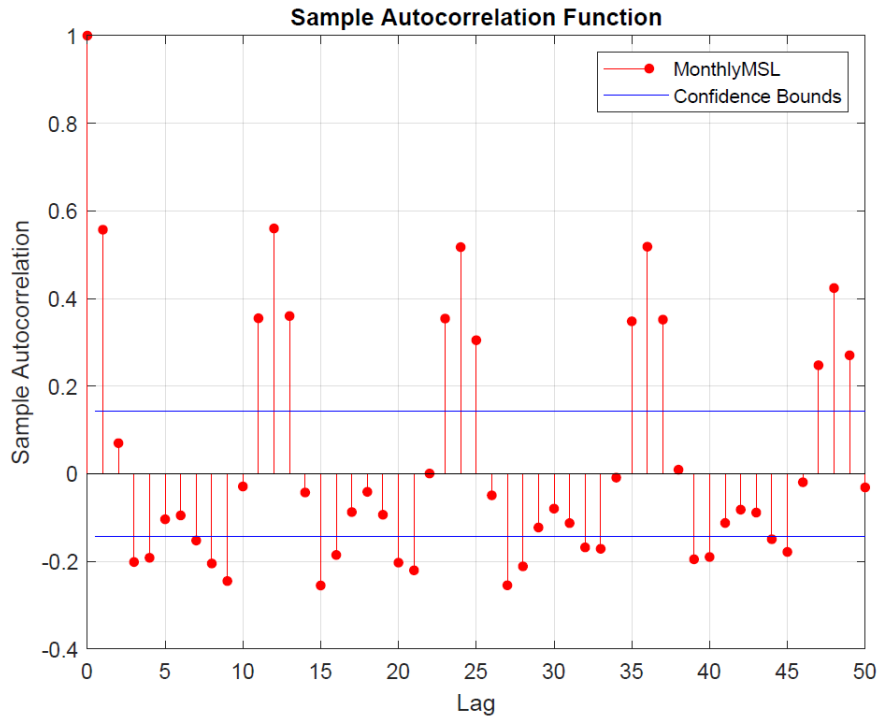
Figure 3- 11. The autocorrelation function (ACF) for the time series of monthly mean sea level before differencing to remove the seasonal trend. The ACF does not decay to zero, therefore, seasonal differencing is necessary to make the time series stationary.
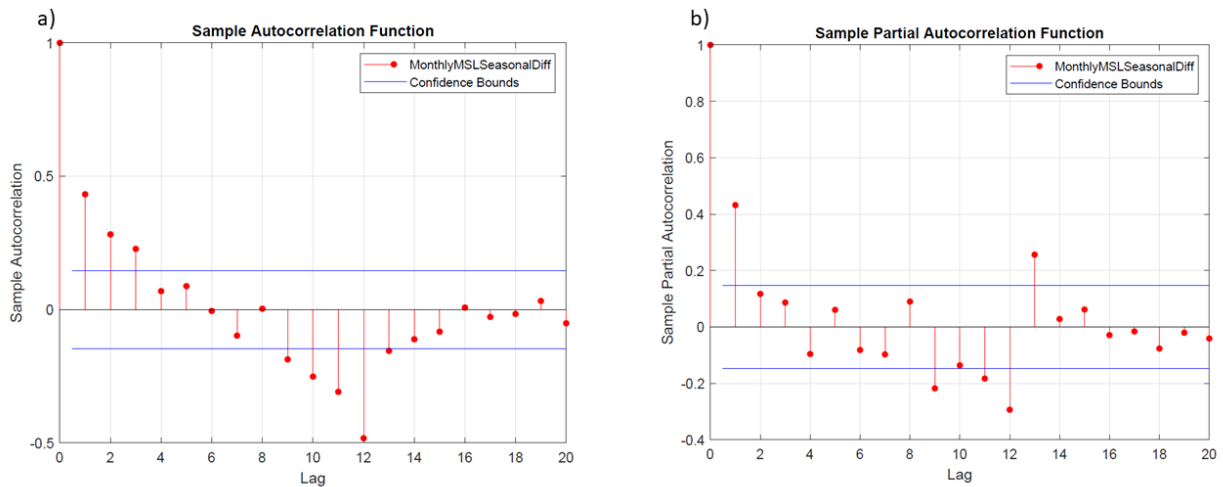
Figure 3- 12. The ACF (a) and partial auto correlation functions (PACF) (b) for the monthly mean sea level time series after seasonal differencing. The ACF indicates a 12-month seasonal cycle and the PACF decays after the first lag indicating a seasonal moving average of order 1 with a 12-month period.
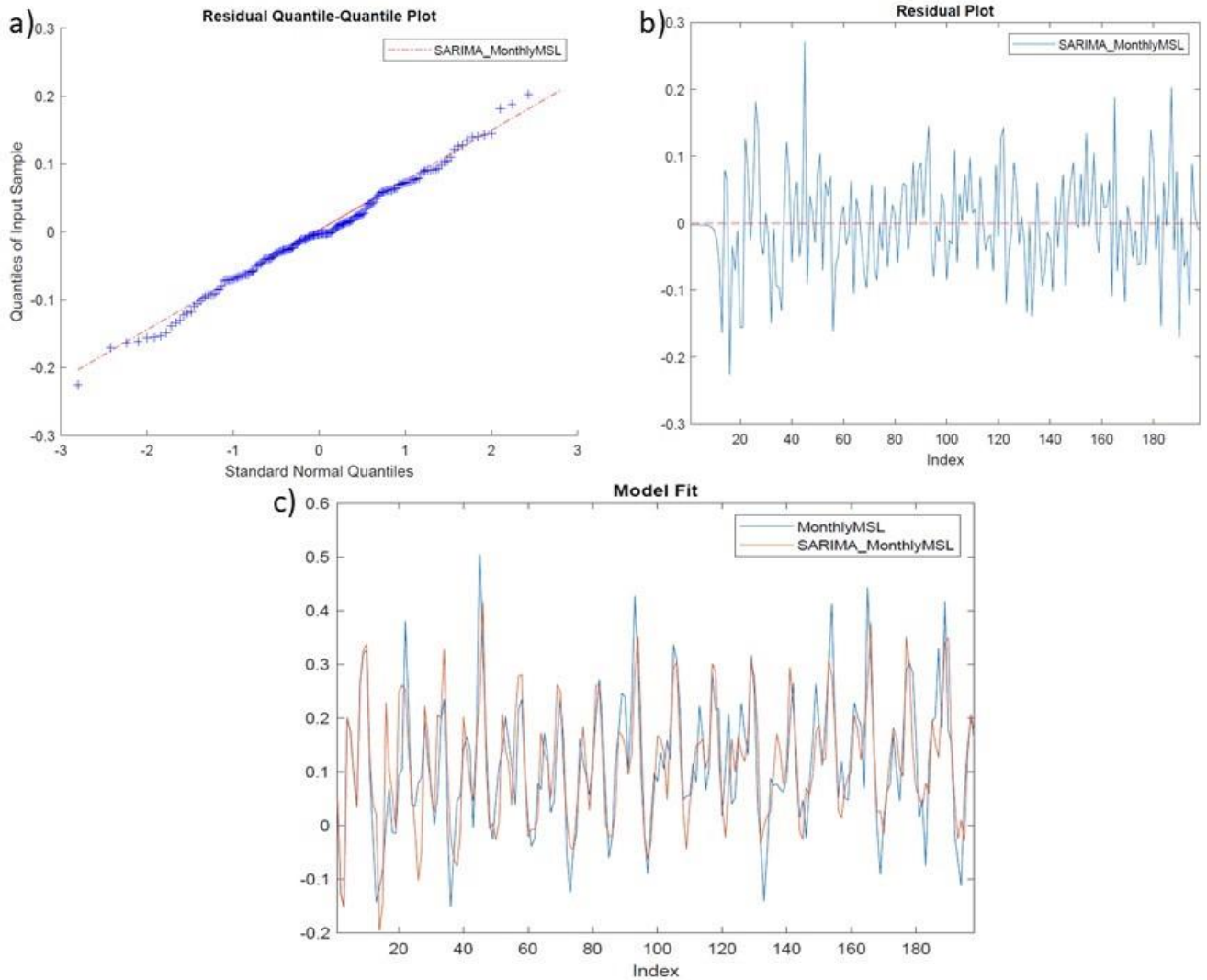
Figure 3- 13. Quantile-Quantile Plot (a), residual plot (b), and model-fit (c) of the SARIMA $(1,0,0)(0,1,1)_{12}$ model indicating a reasonable model fit for the SARIMA parameters.

Test statistics, seen in Table 3-5, test the null hypothesis that the modeled series is different from the original time series, and all tests show that the null hypothesis can be rejected and that the model if fit for forecasting.

Table 3-5. Statistical parameters for the SARIMA $(1,0,0)(0,1,1)_{12}$ model

Parameter	Value	Standard Error	t Statistic	P-Value
Constant	0.0012446	0.0018856	0.66007	0.50921
AR(1)	0.37863	0.062471	6.0609	1.3533e-09
SMA(12)	-0.68369	0.055955	-12.2185	2.4769e-34
Variance	0.0057187	0.00050396	11.3475	7.6294e-30
AIC	-452.5759			
BIC	-439.6945			

3.4.3 SARIMA Forecast Results

The 5- and 10-year forecast results demonstrate that autoregressive models such as SARIMA can be used to forecast RSL based on tide gauge data with accuracy for short periods of time. In the 24-month periods in which the forecasts overlap the observed data, all the observations fall within the 95% confidence interval of the forecasted model and validates the accuracy of the model. However, as the forecast length is increased, the uncertainty in the model increases, indicating this model is useful for short-term forecasts, but may not estimate long-term forecasts accurately. As seen in Figures 3-14 and 3-15, the SARIMA $(1,0,0)(0,1,1)_{12}$ model retains both the seasonal and linear trends of the modeled data providing a month by month forecast of RSL at each tide gauge location. Since the annual cycle of sea level is similar throughout the northern GOM, the same model parameters can be applied for each location in this study if the model is estimated on the observed data unique to each tide gauge station.
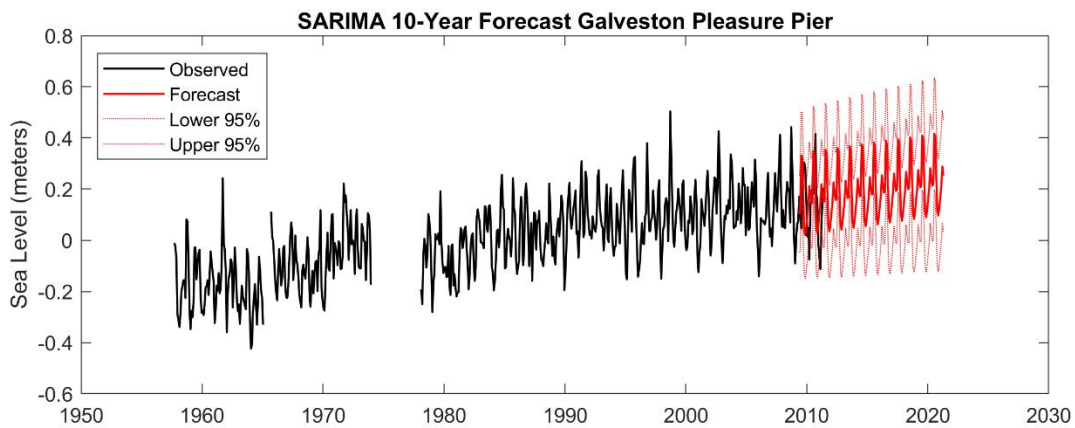
Figure 3- 14. SARIMA forecast results for Galveston Pleasure Pier, TX.
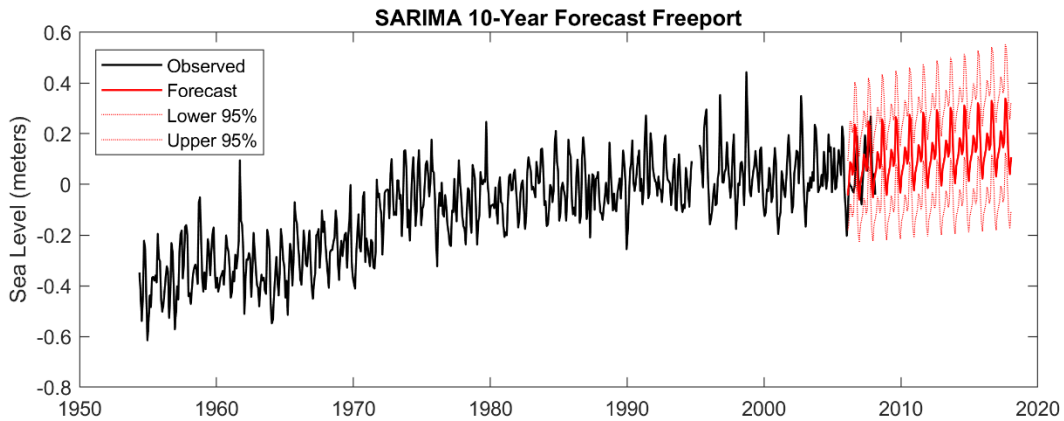
Figure 3- 15. SARIMA forecast results for Freeport, TX.

Results varied based on the length of the observed time series that the model is estimated from. For example, the Corpus Christi tide gauge record dates to 1998 and the results seen in Figure 3-16 demonstrate how the uncertainty increases more quickly than Galveston Pier 21, whose record dates to 1904 (Figure 3-17). Analysis of the forecast from Galveston Pier 21 (Figure 3-18) reveals the details of the model output validated by the 24-month observation period. As seen in Figure 3-18, the uncertainty does not increase as quickly over the forecasted timeframe as Corpus Christi and Sabine Pass. For Sabine Pass, Figure 3-19, uncertainty

increased with time as well suggesting that length of the time series as well as consistency in the record (Sabine Pass contains many months with missing data) affects both the accuracy and uncertainty of the model.
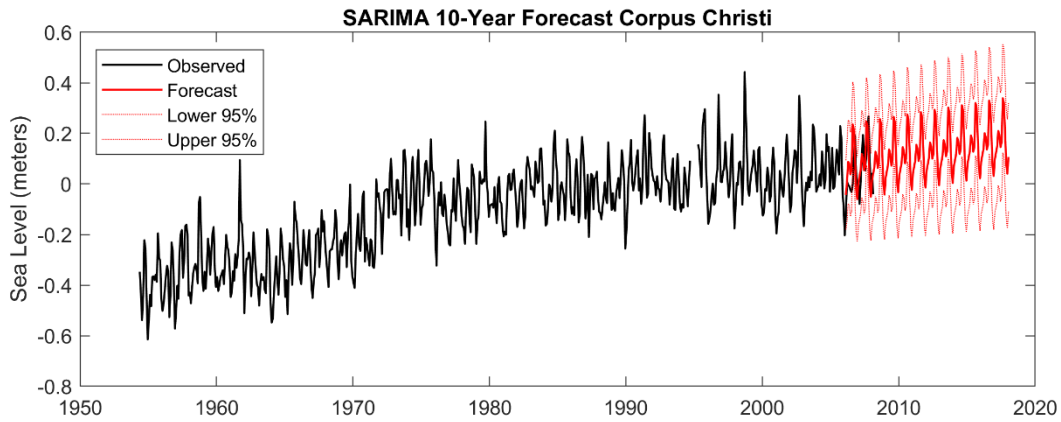
Figure 3- 16. SARIMA forecast results for Corpus Christi, TX.
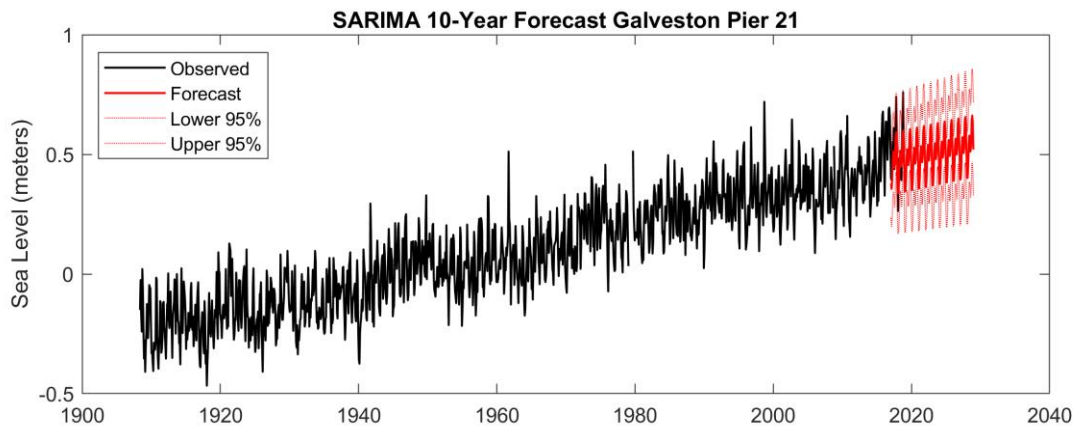
Figure 3- 17. SARIMA forecast results for Galveston Pier 21, TX.
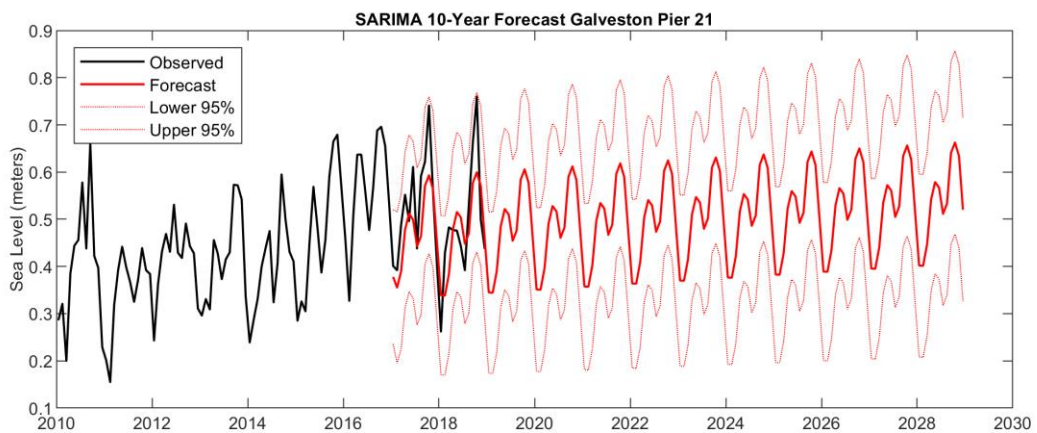
Figure 3- 18. Detailed results from Galveston Pier 21 from 2010.
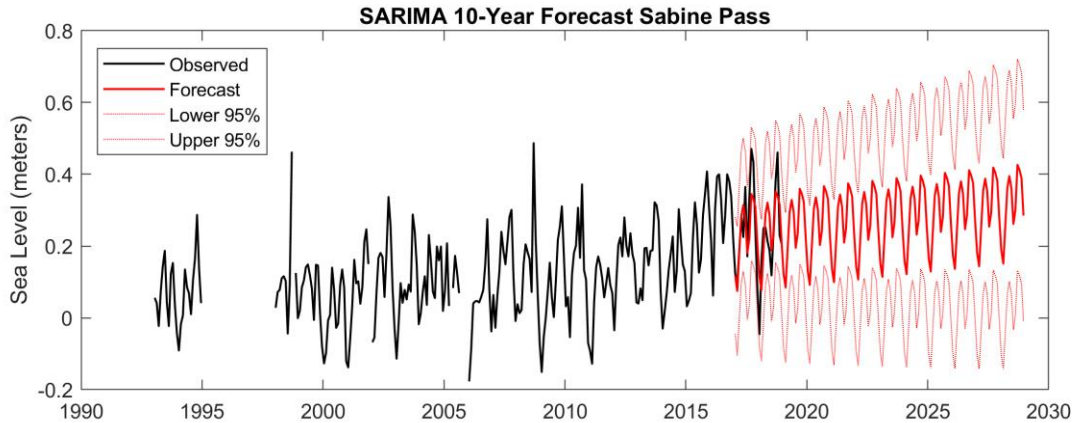
Figure 3- 19. SARIMA forecast results for Sabine Pass, TX.

3.5 Risk assessment of SLR: Case studies Galveston, Texas, and New Orleans, Louisiana

Uncertainties exist in sea level rise future estimates for planning purposes for example associated with earth system model's initial and boundary condition, e.g., associated with anthropogenic emissions results, and model parameterizations (Hall et al., 2016). Prediction of sea level estimates by extrapolation from linear regression models of tide gauge or satellite altimetry data is limited due to non-linear characteristics of future sea-level evolution. Thus, high-risk scenarios have been the most accepted method to manage deep uncertainty regarding the sea level forecast (Sweet et al., 2017; Hinkel et al., 2015; King et al., 2015; Ranger et al., 2013). Generally, this consists of using a plausible extreme scenario of low probability as the upper-bound scenario and defining two mid-range scenarios that consider future changes in climate and emissions that define the design range (Sweet et al., 2017; Hinkel et al., 2015).

Such a methodology has been applied for example in a coastal risk-management application for the cities adjacent to the Thames estuary for the year 2100 as described in the TE2100 Project for London, England (Ranger et al., 2013). The project established an upper bound of 2.7 meters of SLR by combining observations of rates of SLR from the last interglacial period from Rohling et al. (2008), glaciological arguments from Pfeffer et al. (2008), as well as regional and local factors. This high-end scenario was used along with a most likely range, with the most likely range informing the short-term (30 years) adaptation decisions, and the high-end scenario informing what further actions may be necessary into the future, as well as offering a motivation for monitoring. This combination of numerical models and expert judgement to develop SLR scenarios for the TE2100 project resulted in adaptation pathways for the worst-case scenario and alternative pathways if SLR was lower. This method allowed for a strategy of investing in near-term solutions while keeping longer-term options open, monitoring SLR, and based on monitoring, updating the assessment of the long-term, high-end scenario, and implementing alternative measures as needed.

The approach listed above and assuming a community along the Gulf of Mexico would desire a low level of risk, an example case study was conducted using GMSL rise scenarios with exceedance probabilities of less than 50% based on the probabilistic analysis of Kopp et al. (2014). Using Table 3-6 as a guide, the Intermediate and Intermediate-High scenarios were selected as the lower and upper bounds respectively for the design range. The extreme scenario was also chosen as a scientifically plausible worst-case scenario, or upper bound (Hinkel et al., 2015).

Table 3-6. Probability of exceeding GMSL scenarios in 2100 based on Kopp et al. (2014).

GMSL rise scenario	RCP 2.6	RCP 4.5	RCP 8.5
Low (0.3 m)	94%	98%	100%
Intermediate-Low (0.5 m)	49%	73%	96%
Intermediate (1.0 m)	2%	3%	17%
Intermediate-High (1.5 m)	0.4%	0.5%	1.3%
High (2.0 m)	0.1%	0.1%	0.3%
Extreme (2.5 m)	0.05%	0.05%	0.1%

Applying the scenarios to the northern GOM tide gauge locations' RSL projections and utilizing map layers developed by NOAA (tides and currents), a visualization of RSL in 2100, Figure 3-20, was created to explore the potential impacts to the region. In many areas, the extreme scenario results in increased depth of water rather than increased area of flooding due to topography, and in some areas, such as New Orleans, flood defense systems protect the area from inundation.
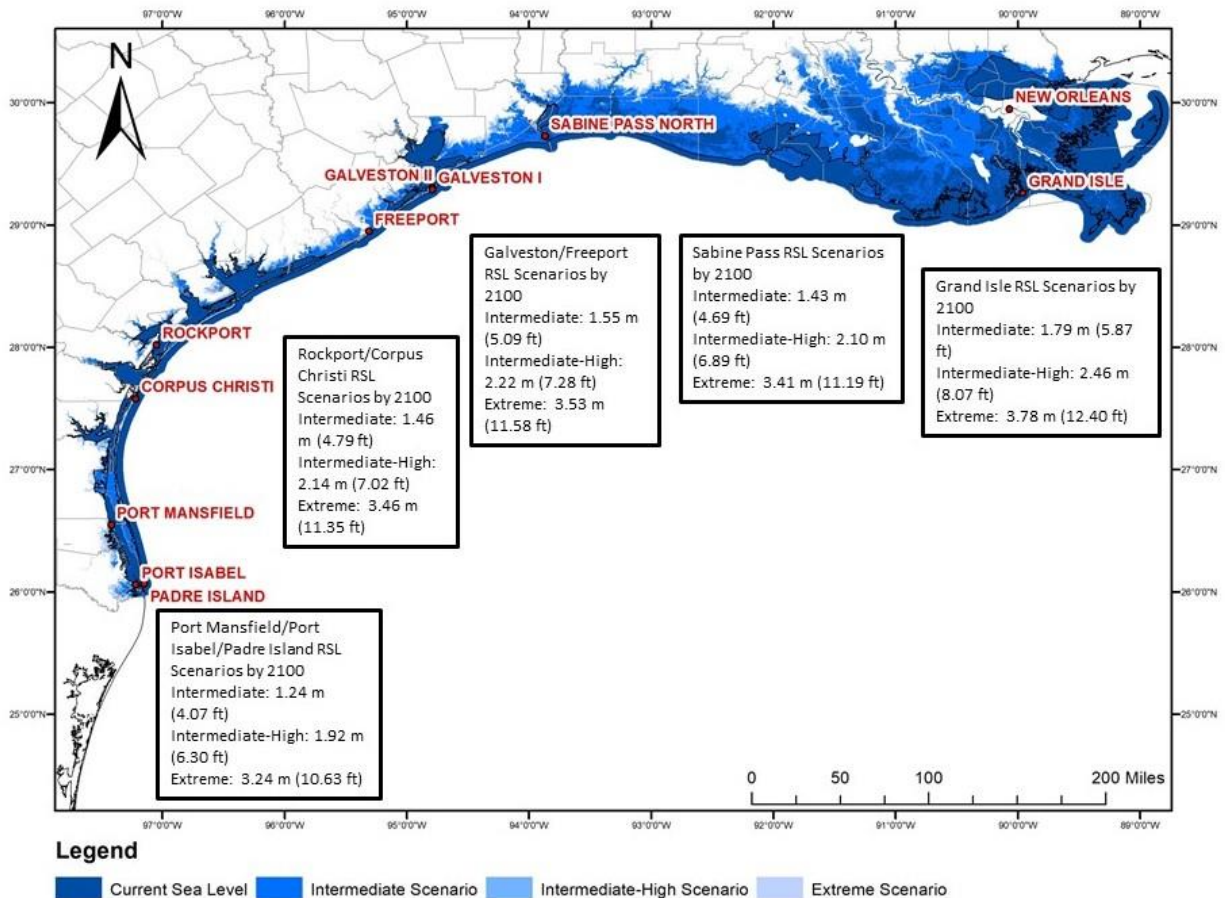
Figure 3- 20. A map of northern GOM RSL in 2100 based on the Intermediate, Intermediate-High, and Extreme scenarios. Projections of RSL by region broken down by scenarios are provided within the boxed areas.

Figure 3-21 demonstrates that the New Orleans East Bank Levee System, made up the Mississippi River Levees and the Hurricane and Storm Damage Risk Reduction System and updated post Hurricane Katrina, protects the area from SLR of 3 meters despite most of the area being below 3 meters elevation. According to the United States Army Corps of Engineers (USACE), the system has a maximum average height of 26 feet (~8 meters) and protects nearly 850,000 people who live within the levees (USACE, 2020).

Communities located directly on the GOM coast such as Freeport, Sabine Pass, and Galveston Island are impacted the most from the increased RSL. Forecasted RSL for the City of Galveston revealed that its 17-foot (~ 5 meter) seawall protects the most populated areas of the city from flooding along the beachfront, but the city has low elevation and a lack of flood protection on the back bay side. Despite attempts to increase Galveston's elevation (Figure 3-22) after it was devastated in the Great Galveston Hurricane of 1900, future RSL scenarios seem to cause at least, nuisance tidal flooding and, in the extreme scenario, almost total inundation from SLR by 2100 (Figure 3-23). Inundation mapping of RSL scenarios can help determine when, where, and how much flooding will occur if the model projections come about, and the maps can be
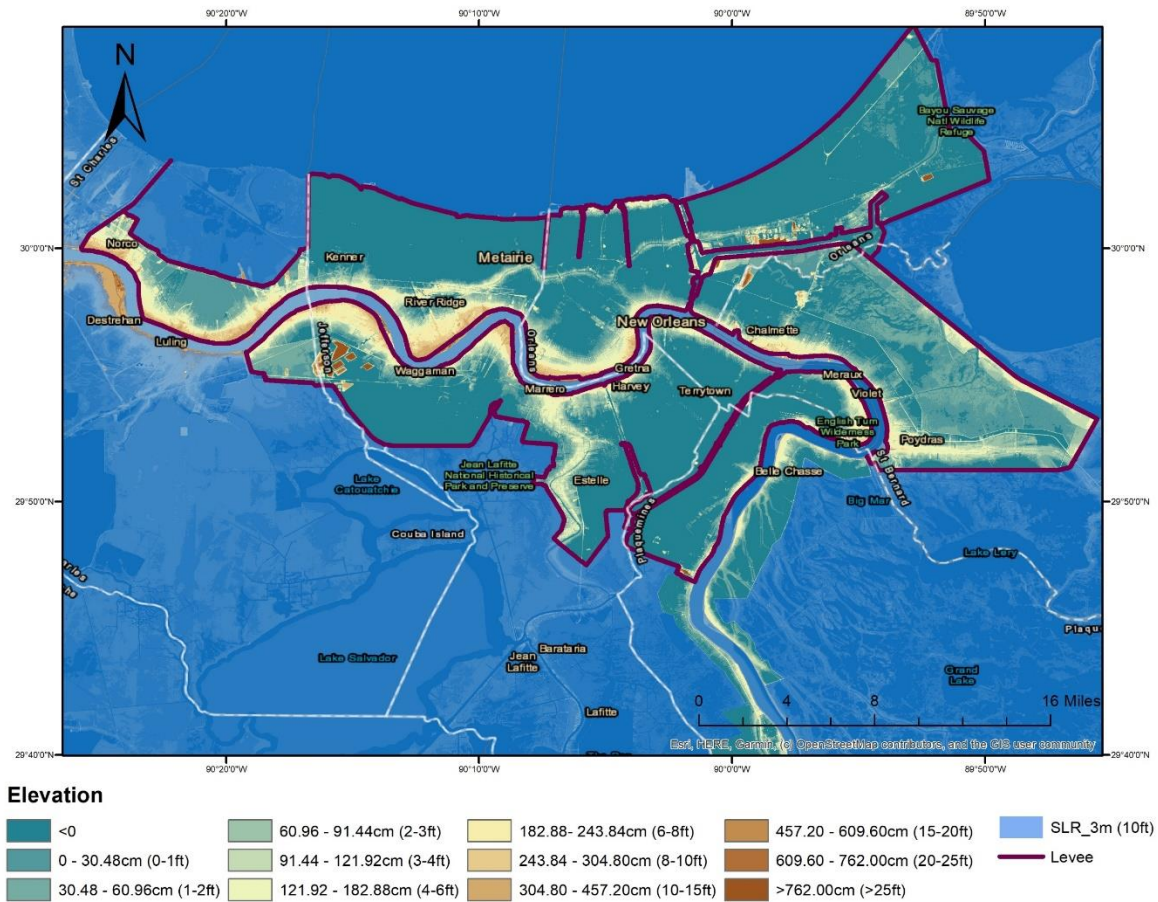
Figure 3- 21. New Orleans, Louisiana digital elevation model overlaid with ~3 meters (10 feet) SLR layer from NOAA tides and currents and the New Orleans East Bank Levee System from USACE demonstrating the system's ability to protect from the extreme RSL scenario despite most of the city being below 3 meters elevation.

overlaid with infrastructure and/or demographics for sea level rise risk assessments (Figure 3-24). This type of assessment can be useful in illustrating the height and locations of high-tide or nuisance flooding that would be expected to occur regularly under the RSL scenarios chosen rather than assessments of extreme water levels resulting from rare but devastating storm surges from hurricanes. While extreme water levels can and should be considered and will likely be enhanced by RSL rise, the regular occurrence of high tide and the robust evidence for sea level rise observed in the tide gauge records indicates locations within the study area will be most impacted by the effects of nuisance flooding due to RSL rise, especially when this flooding begins to occur on a regular basis.

Elevation

<0	
0 - 30.48cm (0-1ft)	
30.48 - 60.96cm (1-2ft)	
60.96 - 91.44cm (2-3ft)	
91.44 - 121.92cm (3-4ft)	
121.92 - 182.88cm (4-6ft)	
182.88 - 243.84cm (6-8ft)	
243.84 - 304.80cm (8-10ft)	
304.80 - 457.20cm (10-15ft)	
457.20 - 609.60cm (15-20ft)	
609.60 - 762.00cm (20-25ft)	
>762.00cm (>25ft)	
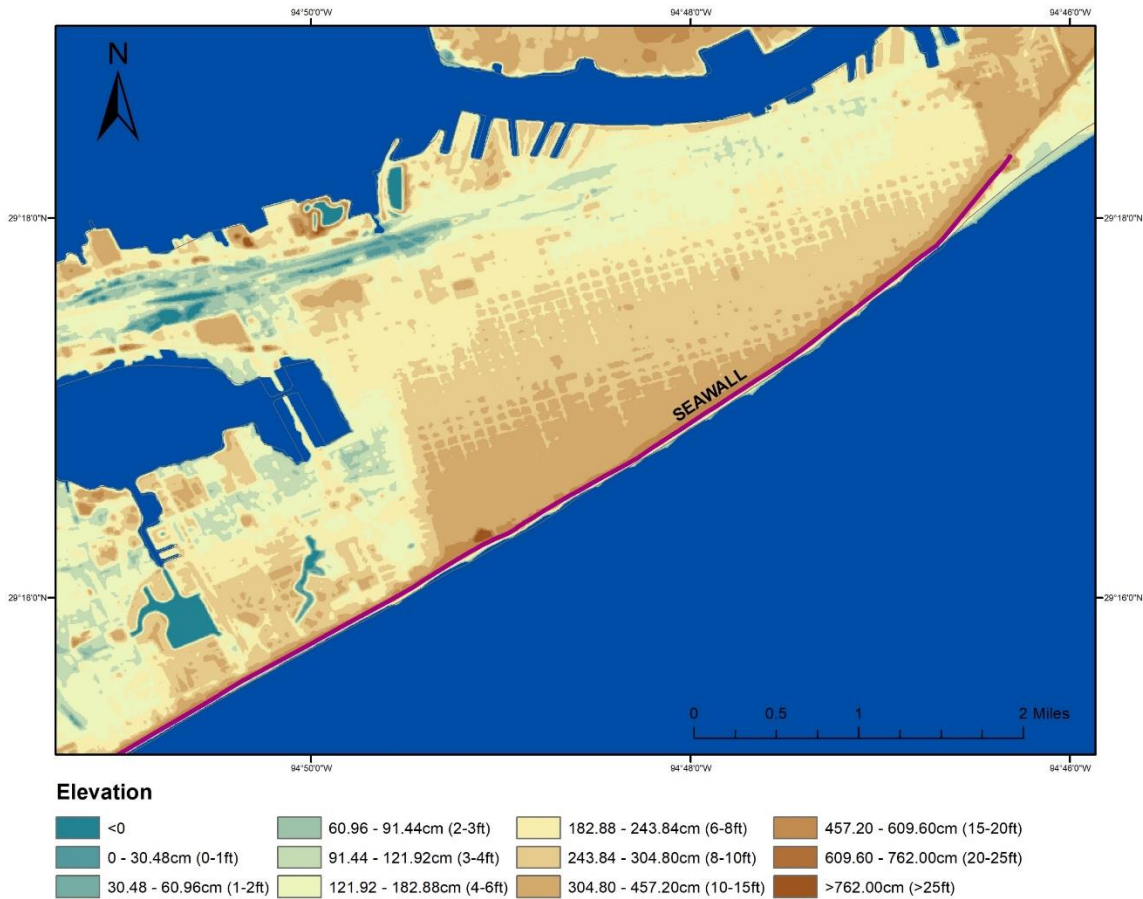
Figure 3- 22. Galveston, Texas digital elevation model with the Seawall (purple line) indicated.

Under the Intermediate scenario, Figure 3-23a shows the effects of RSLR will be experienced first in areas of lowest elevation on the back bay side of the island by 2060. By 2100, inundation from high tides (Figure 3-24a) will impact residential and commercial areas close to the harbor and in the southwest portion of the study area with a range of < 30.5 cm (1 ft) to 61 cm (2 ft) above ground. This is likely to cause temporary minor flooding of roads and low-lying topography, but unlikely to pose a risk to above-ground infrastructure. Under this scenario, most of the island's population and infrastructure will not be directly impacted by flooding due to RSLR. However, the lowest lying areas are projected to experience high tide inundation of ~122 cm-155 cm (4 ft-5 ft) by 2100.

Both the Intermediate-High and Extreme scenarios (Figures 3-23b and 3-23c) indicate the effects of RSLR in the lowest elevations will be seen earlier, by 2040, and will impact a larger area. By 2080, the medical district (two hospitals in Figure) will also begin to experience the effects. Under the Intermediate-High scenario, most of the residential and commercial area adjacent to the harbor which includes the main fire and police departments as well as two schools will experience up to ~122 cm (4 ft) of water above ground by 2100 (Figure 3-24b). The residents located in the southwest quadrant of the study area, including four schools, will experience up to ~153 cm (6 ft) of inundation by 2100. These inundation levels will cause roads to be temporarily inaccessible during the highest tides and may cause flooding of low-lying residential and commercial buildings. While the specifics of structural engineering are not the focus of this study, it is of note that many, but not all, residential buildings in the lowest elevations of Galveston are raised on piers.

The Extreme scenario impacts the entire study area by 2100 except for the highest ground located adjacent to the seawall (Figure 3-23c) and effects in the harbor area and the southwest quadrant will be seen by 2060 rather than 2080 in the previous scenarios. By 2100, up to ~244 cm (8 ft) of inundation is projected for these areas of great commercial and residential interest. Inundation in the medical district is projected at ~91.5 cm-183 cm (3 ft-6 ft) by 2100 and up to eight additional schools will be within the area of inundation of ~30.5 cm-122 cm (1 ft-4 ft). This scenario may result in impacts beyond a "nuisance" level including regular flooding of commercial and residential structures, road closures and damages, and flooding of sewage and drainage systems.

This case study demonstrates the application of Probabilistic Projections of RSL rise to flood inundation mapping to identify potential areas of concern over time in the study area. Although New Orleans and Galveston were used as examples, this method can be applied to any specific location along the northern GOM for use in risk assessment and planning. SARIMA modeling was not used in this case study due to the lack of accuracy in the long-term (beyond 10 years) forecast and the inability to include acceleration scenarios.
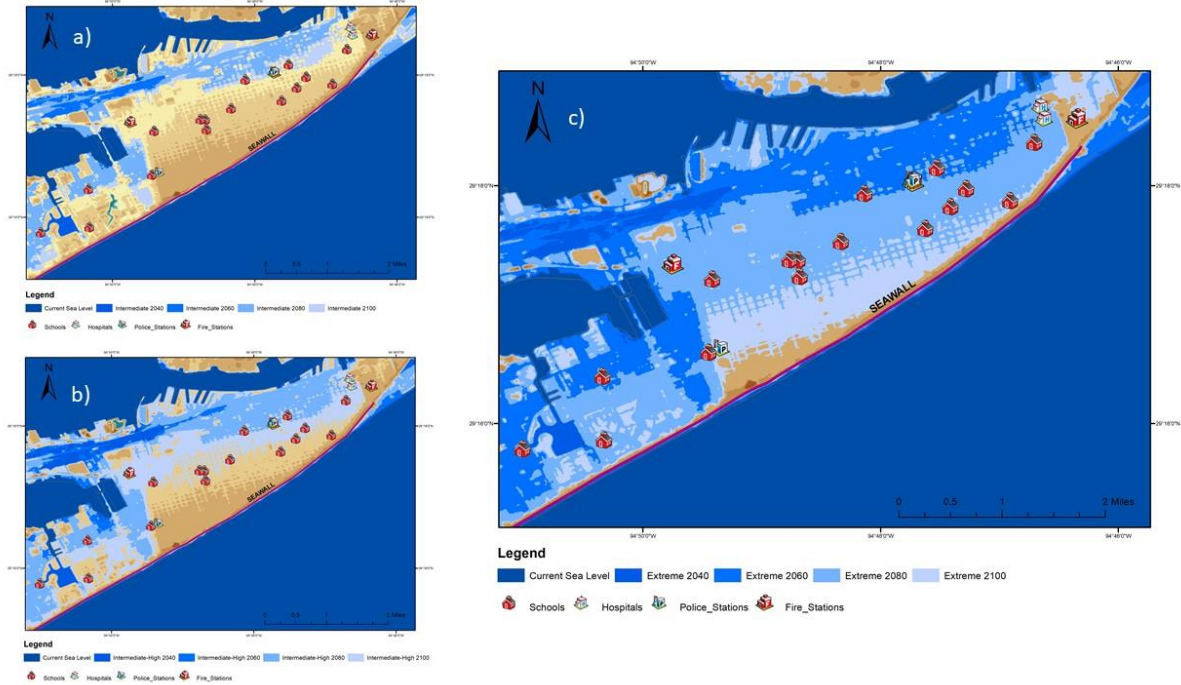
Figure 3- 23. (a) Intermediate, (b) intermediate-high, and (c) extreme RSL scenarios by 20-year increments for Galveston, Texas. Infrastructure included are schools, hospitals, police, and fire stations.
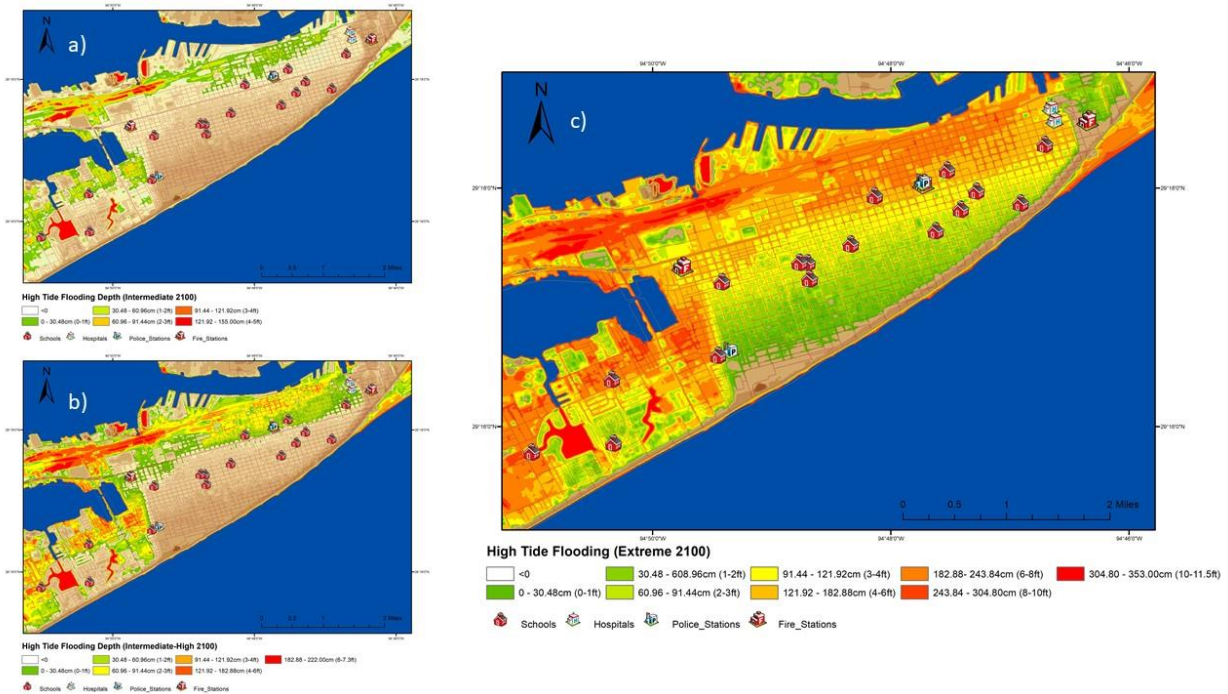
Figure 3- 24. (a) Intermediate, (b) intermediate-high, and (c) extreme RSL scenarios for high tide inundation in 2100 for Galveston, Texas.

3.6 Analysis and Discussion

In the following, differences between the two RSL projection methods, the SARIMA estimate and the probabilistic projection will be discussed. Forecasting RSL using a SARIMA model provides an autoregressive integrated approach that resolves seasonal fluctuations but does not account for any future acceleration of the RSL rise rate. This may have a reasonable forecast skill for predicting tidal flooding or forecasting RSL in the near future of up to 10 years (Srivastava et al., 2016), but does not include any processes that is not reflected in the historic record, such as sudden rapid climate changes. To account for possible acceleration of RSL in tide gauge records, exponential smoothing models, such as the Holt-Winters model, also known as exponential triple smoothing, have been utilized for short-term forecasting of RSL with statistical accuracy and computational efficiency (Imani et al., 2013). Parker et al. (2013) used linear, parabolic, and sinusoidal fitting methods to analyze trends in Australian tide gauge data but found no evidence of acceleration while noting that the length of the timeseries (100 years) was not adequate to detect acceleration. In Florida, a linear second order polynomial model was used to forecast accelerating RSL to 2080 with the parameters of the model being based solely on seasonally detrended monthly sea level (Walton, 2007).

Acceleration of GMSL rise can occur due to increases in radiative forcing from anthropogenic emissions, as projected in the RCPs chosen for this study, or from accelerated Greenland and Antarctic ice sheet melting. These two factors contribute to deep uncertainty in GMSL projections as do uncertainties of initial conditions, boundary conditions and model parameterizations inherent in global climate models used. The RCPs used in this study were developed for use in global climate models, including those utilized in CMIP5, using projections of population, gross domestic product (GDP), energy per unit income, emissions per unit energy, land use, aerosols, and other factors that contribute to radiative forcing (Vuuren et al., 2011). These variables include socio-economic, geo-political as well as technological uncertainties that include reducing emissions or going on with business as usual.

The freshwater input from Antarctic and Greenland ice sheets are also uncertain with projected contributions to SLR by 2100 complicated by incomplete knowledge of the forcings on surface mass balance, calving of icebergs, the dynamics of discharge, runoff, and percolation/basal lubrication, ocean warming effects, as well as the unknown possible tipping points that could lead to runaway melting (Pritchard et al., 2009; Rignot et al., 2011; Pattyn et al., 2018; Pattyn et al., 2020). While natural causes of subsidence are thought to be mostly constant or linear, anthropogenic influences on subsidence can contribute to acceleration or deceleration of RSL rise rates locally (Kolker et al., 2011). It is recommended that dynamic RSL predictions should consider such sea level rise accelerations for long-term risk-based planning efforts (e.g., Kopp et al., 2016; Foster and Brown, 2015; Church and White, 2011; Jevrejeva et al., 2008).

A case study of New Orleans suggests that efforts of an improved flood protection system increased the resilience the city's flooding by RSL rise inundation. However, groundwater flooding is expected to increase due to the water table being linked to the sea level in coastal locations (Rozell, 2021). Groundwater flooding can cause flooding of storm sewers and basements, corrosion of underground infrastructure, and minor street flooding that often requires pumping. While often overlooked in coastal climate vulnerability studies, modeled SLR-driven groundwater flooding was found to be significant and widespread in Northern California coastal plains under 1- and 2-meter SLR scenarios (Hoover et al., 2017). Groundwater flooding of properties can also occur with relatively low return period flood events of 10-25 years

(Macdonald et al., 2012). In New Orleans, groundwater flooding is generated by high groundwater tables in shallow sands that are recharged by surface water located in areas not adjacent to the Mississippi River including properties neighboring Lake Pontchartrain, the Lower Ninth Ward, and others near canals (Yang and Tsai, 2020). Groundwater flow modeling in 2018 indicated 40% of the metropolitan area may have groundwater levels above ground surface year-round and that areas of under-seepage of groundwater coincide with locations of breached levees during Hurricane Katrina (Yang and Tsai, 2020).

In the following, the community-level impacts of RSLR on transportation, property damage, and public health hazards are discussed. While the impacts of RSLR in coastal locations do not pose an acute threat to life and property, over time the cumulative effects of regular minor flooding can disrupt regular functions of an area, cause infrastructure problems with storm sewers and transportation networks, result in property damage, and can increase hazards related to human health. Regarding transportation, a minimal flood depth of 30 cm (~1 ft) is considered the "floating limit" for stationary small passenger cars at which point the vehicle may be washed away depending on the velocity of the water (Cox et al., 2010). Road closures due to flooding interrupt the regular flow of traffic resulting in loss of productivity and income, and decrease efficiency of emergency response (Moftakhari et al., 2018). Furthermore, flooding of roads, sidewalks, and crosswalks limits the ability of public transit, cyclists, and pedestrians, and disproportionately affects those with disabilities. Property damage from flooding is dependent on the depth of water above the first "finished floor" which vary and are regulated by local building codes (Scawthorn et al., 2006). Commercial areas are typically developed with buildings that have doorways at ground level leaving them susceptible to intrusion by floodwaters that overtop street curbs and residential buildings with the first floor at ground level are similarly vulnerable (Moftakhari et al., 2018). Although major structural damages result from forces and erosion associated with the combination of high-water depth and velocity not seen with flooding accompanying RSLR (Kelman and Spence, 2004), flood resilient construction can protect against damages caused by nuisance-level flooding such as to electrical components (Proverbs and Lamond, 2017). Regular flooding from RSLR poses a threat to public health by providing habitat for disease vectors, causing indoor mold, and possibly contaminating water supplies. When sewage systems are affected, flood waters have been found to contain toxic chemicals and bacteria that cause illness. The contaminated water can spread the effects well beyond the point of origin through runoff into waterbodies, and this flood water can contain fecal bacterial levels similar to raw sewage (ten Veldhuis et al., 2010).

3.7 Conclusion

This study aimed to provide a methodology for assessing RSLR beyond the observational record that incorporates subsidence and the acceleration of global SLR with the ability to provide a range of possible future outcomes over time at coastal locations in the northern GOM. Through literature review and tide gauge data analysis, it is shown that all tide gauge stations in the northern GOM measure rates of RSLR higher than the global average (~3.0 mm/yr) due to geologic and anthropogenic induced subsidence. Furthermore, results indicate that SARIMA modeling provides a short-term forecast ability with a 95% confidence interval that may be useful for risk assessment of high tide (nuisance) flooding over the next decade but lacks the ability to simulate likely acceleration of GMSL rise over time. Probabilistic Projections of RSL developed by Parris et al. (2012) and improved upon by Kopp et al. (2014) and Hall et al., (2016), however, provide a range of acceleration scenarios over time out to 2100. By selecting

scenarios based on probability of exceedance, uncertainty can be addressed by choosing low and high design-range scenarios as well as a scientifically plausible extreme scenario for analysis. This method has broad applications in risk assessments as inundation maps utilizing projections can provide temporal and geospatial results of high tide water levels under each scenario. This is most useful for engineers, designers, and planners making key decisions about how much RSLR will impact new or existing infrastructure. For infrastructure where flooding represents a particular danger to the public (e.g., power plants, refineries, chemical plants, wastewater treatment facilities, etc.), projects with long planning horizons, or infrastructure with limited adaptability, failure to include low-probability, high-risk scenarios in decision making may result in higher future risk. An inundation mapping case study shows that RSLR represents a risk to Galveston, TX, of up to ~1.55 m (5 ft), ~2.22 m (7.3 ft), and ~3.53 m (11.5 ft) under the intermediate, intermediate-high, and extreme scenarios respectively. While these projections do not include extreme water levels caused by storm surges or excessive precipitation, they do provide estimates of RSL over time that are beneficial to assessing risk of tidal flooding that may occur rarely today but will likely become a regular hazard in the future.

3.8 Future Work

Planners and policy makers in the northern GOM need to consider all the risks of flooding into the future with a changing climate and associated alteration of coastal morphology. Therefore, improvements on risk assessments should not only include locally significant RSL projections but other factors that may separately or synergistically affect flooding such as extreme precipitation or storm surge enhanced by RSL. The USGS utilizes the Coastal Vulnerability Index (CVI) to assign a risk value (Low to Very High) based on a matrix of both qualitative and quantitative parameters that include geomorphology, shoreline erosion/accretion rates, coastal slope, RSL rise rate, mean significant wave height, and tidal range (Pendleton et al., 2010). These types of matrices to assign an index value are excellent tools for planners and policy makers that can be improved to include RSL projections (assuming all other parameters are linear or static), hurricane return periods, and a quantitative probability of exceedance for nuisance flooding. Extreme precipitation also plays a role in flooding but is not unique to coastal locations and therefore should not be included in a coastal risk matrix, rather risk assessors should analyze this parameter separately. Many anthropogenic influences other than greenhouse gas emissions will affect flood hazards into the future such as population growth in flood prone areas, increased impervious surfaces (land-use changes), the building of flood protection barriers, and various socioeconomic and political factors. While consideration should be given to these parameters and possibly others by planners and policy makers, this future research will focus on enhancing flood risk assessment by including the climate factors of hurricanes and storm surge, quantifying the probability of minor flooding, and analyzing changes in precipitation (if any) in the northern GOM.

References

Blum, M. D., and Roberts, H. H. (2009). Drowning of the Mississippi Delta due to insufficient sediment supply and global sea-level rise. *Nature Geoscience*, *2*(7), 488.

Box, G.E.P., Jenkins, G.M., Reinsel, G.C., and Ljung, G.M. (2015). *Time Series Analysis: Forecasting and Control* 5th ed. Hoboken, NJ: John Wiley and Sons.

Church, J. A., and White, N. J. (2011). Sea-level rise from the late 19th to the early 21st century. *Surveys in geophysics*, *32*(4-5), 585-602.

Cox, R. J., Shand, T. D., and Blacka, M. J. (2010). Australian Rainfall and Runoff revision project 10: appropriate safety criteria for people. *Water Research*, *978*, 085825-9454.

Fernandez, F. R. Q., Montero, N. B., Po III, R. B., Addawe, R. C., and Diza, H. M. R. (2018). Forecasting manila south harbor mean sea level using seasonal ARIMA models. *Journal of Technology Management and Business*, *5*(1).

Fernandez, F. R. Q., Po III, R. B., Montero, N. B., and Addawe, R. C. (2017). Prediction of South China sea level using seasonal ARIMA models. In AIP Conference Proceedings (Vol. 1905, No. 1, p. 050018). AIP Publishing.

Foster, G., and Brown, P. T. (2015). Time and tide: analysis of sea level time series. *Climate Dynamics*, *45*(1-2), 291-308.

González, J. L., and Tornqvist, T. E. (2006). Coastal Louisiana in crisis: Subsidence or sea level rise?. *EOS, Transactions American Geophysical Union*, *87*(45), 493-498.

Hall, J.A., Gill, S., Obeysekera, J., Sweet, W., Knuuti, K., and Marburger, J. (2016). Regional sea level scenarios for coastal risk management: Managing the uncertainty of future sea level change and extreme water levels for department of defense coastal sites worldwide. U.S. Department of Defense, Strategic Environmental Research and Development Program. 224 pp.

Hinkel, J., Jaeger, C., Nicholls, R. J., Lowe, J., Renn, O., and Peijun, S. (2015). Sea-level rise scenarios and coastal risk management. *Nature Climate Change*, *5*(3), 188-190.

Hoover, D. J., Odigie, K. O., Swarzenski, P. W., and Barnard, P. (2017). Sea-level rise and coastal groundwater inundation and shoaling at select sites in California, USA. *Journal of Hydrology: Regional Studies*, *11*, 234-249.

Imani, M., You, R. J., and Chung-Yen, K. (2013). Accurate Forecasting of the satellite-derived seasonal Caspian Sea level anomaly using polynomial interpolation and holt-winters exponential smoothing. *Tao: terrestrial, atmospheric and oceanic sciences*, *24*(4), 521.

Ivins, E. R., Dokka, R.K., and Blom, R.G. (2007). Post-glacial sediment load and subsidence in coastal Louisiana, *Geophys. Res. Lett.*, 34, L16303, doi:10.1029/ 2007GL030003.

Jevrejeva, S., Moore, J. C., Grinsted, A., and Woodworth, P. L. (2008). Recent global sea level acceleration started over 200 years ago?. *Geophys. Res. Lett.*, *35*(8).

Kelman, I., and Spence, R. (2004). An overview of flood actions on buildings. *Engineering Geology*, *73*(3-4), 297-309.

King, D., Schrag, D., Dadi, Z., Ye, Q., and Ghosh, A. (2017). Climate change: a risk assessment. University of Cambridge Centre for Science and Policy, 154 pp.

Kolker, A. S., Allison, M.A., and Hameed, S. (2011). An evaluation of subsidence rates and sea level variability in the northern Gulf of Mexico, *Geophys. Res. Lett.*, 38, L21404, doi:10.1029/2011GL049458.

Kopp, R. E. (2013). Does the mid-Atlantic United States sea level acceleration hot spot reflect ocean dynamic variability?. *Geophys. Res. Lett.*, *40*(15), 3981-3985.

Kopp, R. E., Horton, R.M., Little, C.M., Mitrovica, J.X., Oppenheimer, M., Rasmussen, D.J., Strauss, B., and Tebaldi, C. (2014). Probabilistic 21st and 22nd century sea-level projections at a global network of tide-gauge sites. *Earth's Future*, 2(8), 383-406.

Kopp, R. E., Kemp, A.C., Bittermann, K., Horton, B.P., Donnelly, J.P., Gehrels, W.R., and Rahmstorf, S. (2016). Temperature-driven global sea-level variability in the Common Era. Proceedings of the National Academy of Sciences, 201517056.

Macdonald, D., Dixon, A., Newell, A., and Hallaways, A. (2012). Groundwater flooding within an urbanised flood plain. *Journal of Flood Risk Management*, *5*(1), 68-80.

Moftakhari, H. R., AghaKouchak, A., Sanders, B. F., Allaire, M., and Matthew, R. A. (2018). What is nuisance flooding? Defining and monitoring an emerging challenge. *Water Resources Research*, *54*(7), 4218-4227.

Parker, A., Saleem, M. S., and Lawson, M. (2013). Sea-level trend analysis for coastal management. *Ocean & coastal management*, *73*, 63-81.

Parris, A., Bromirski, P., Burkett, V., Cayan, D., Culver, M., Hall, J., Horton, R., Knuuti, K., Moss, R., Obeysekera, J., Sallenger, A., and Weiss, J. (2012). Global sea level rise scenarios for the US national climate assessment. NOAA Tech Memo OAR CPO-1. 37 pp.

Pattyn, F., Ritz, C., Hanna, E., Asay-Davis, X., DeConto, R., Durand, G., Favier, L., Fettweis, X., Goelzer, H., Golledge, N.R., Munneke, P.K., Lenaerts, J.T.M., Norwicki, S., Payne, A.J., Robinson, A., Seroussi, H., Trusel, L.D., and Van den Broeke, M. (2018). The Greenland and Antarctic ice sheets under 1.5 C global warming. *Nature Climate Change*, *8*(12), 1053-1061.
Pattyn, F., and Morlighem, M. (2020). The uncertain future of the Antarctic Ice Sheet. *Science, 367*(6484), 1331-1335.

Perrette, M., Landerer, F., Riva, R., Frieler, K., and Meinshausen, M. (2013). A Scaling Approach to Project Regional Sea Level Rise and Its Uncertainties. *Earth System Dynamics* 4:11–29.

Pfeffer, W. T., Harper, J. T., and O'Neel, S. (2008). Kinematic constraints on glacier contributions to 21st-century sea-level rise. *Science*, *321*(5894), 1340-1343.

Pritchard, H. D., Arthern, R. J., Vaughan, D. G., and Edwards, L. A. (2009). Extensive dynamic thinning on the margins of the Greenland and Antarctic ice sheets. *Nature*, *461*(7266), 971-975.

Proverbs, D., & Lamond, J. (2017). Flood resilient construction and adaptation of buildings. In *Oxford research encyclopedia of natural hazard science*. 1-34.

Ranger, N., Reeder, T., and Lowe, J. (2013). Addressing 'deep'uncertainty over long-term climate in major infrastructure projects: four innovations of the Thames Estuary 2100 Project. *EURO Journal on Decision Processes*, *1*(3-4), 233-262.

Rignot, E., Velicogna, I., van den Broeke, M. R., Monaghan, A., and Lenaerts, J. T. (2011). Acceleration of the contribution of the Greenland and Antarctic ice sheets to sea level rise. *Geophys. Res. Lett.*, *38*(5).

Rohling, E. J., Grant, K., Hemleben, C. H., Siddall, M., Hoogakker, B. A. A., Bolshaw, M., and Kucera, M. (2008). High rates of sea-level rise during the last interglacial period. *Nature geoscience*, *1*(1), 38-42.

Rozell, D. J. (2021). Overestimating coastal urban resilience: The groundwater problem. *Cities, 118*, 103369.

Scawthorn, C., Flores, P., Blais, N., Seligson, H., Tate, E., Chang, S., Mifflin, E., Thomas, W., Murphy, J., Jones, C., and Lawrence, M. (2006). HAZUS-MH flood loss estimation methodology. II. Damage and loss assessment. *Natural Hazards Review*, *7*(2), 72-81.

Srivastava, P. K., Islam, T., Singh, S. K., Petropoulos, G. P., Gupta, M., and Dai, Q. (2016). Forecasting Arabian Sea level rise using exponential smoothing state space models and ARIMA from TOPEX and Jason satellite radar altimeter data. *Meteorological Applications*, 23(4), 633-639.

Sweet, W.V., Kopp, R.E., Weaver, C.P., Obeysekera, J., Horton, R.M., Thieler, E.R., and Zervas, C. (2017). Global and regional sea level rise scenarios for the United States. NOAA Tech. Rep. NOS CO-OPS 083. National Oceanic and Atmospheric Administration, National Ocean Service, Silver Spring, MD. 75 pp.

Sweet, W.V., Horton, R., Kopp, R.E., LeGrande, A.N., and Romanou, A. (2017a): Sea level rise. In: *Climate Science Special Report: Fourth National Climate Assessment, Volume I* [Wuebbles, D.J., Fahey, D.W., Hibbard, K.A., Dokken, D.J., Stewart, B.C. and Maycock, T.K. (eds.)]. U.S. Global Change Research Program, Washington, DC, USA, pp. 333-363, doi:10.7930/J0VM49F2.

Van Vuuren, D. P., Edmonds, J., Kainuma, M., Riahi, K., Thomson, A., Hibbard, K.,

Hurtt, G.C., Kram, T., Krey, V., Lamarque, J., Masui, T., Meinshausen, M., Nakicenovic, N., Smith, S.J., and Rose, S. K. (2011). The representative concentration pathways: an overview. *Climatic change*, *109*(1), 5-31.

Walton Jr, T. L. (2007). Projected sea level rise in Florida. *Ocean Engineering*, *34*(13), 1832-1840.

Yang, S., and Tsai, F. T. C. (2020). Understanding impacts of groundwater dynamics on flooding and levees in Greater New Orleans. *Journal of Hydrology: Regional Studies*, *32*, 100740.

Appendix 3-A

Table 3-A-1. Background RSL rates derived from tide gauge and vertical land movement data.

Tide Gauge Location	Background RSL rate (mm/year)
Grand Isle, LA	7.07 ± 0.25
Sabine Pass, TX	3.54 ± 0.47
Galveston Pier 21, TX	4.59 ± 0.13
Galveston Pleasure Pier, TX	4.64 ± 0.13
Rockport, TX	3.75 ± 0.25
Corpus Christi, TX	2.68 ± 0.30
Port Mansfield, TX	1.39 ± 0.32
Port Isabel, TX	1.83 ± 0.19
Padre Island, TX	1.92 ± 0.20

Chapter 4: Sea Level Rise-Induced High Tide Flooding and Extreme Water Levels of the Northern Gulf of Mexico in Response to Climate Change

Abstract

Relative sea level has increased over the last 120 years with an acceleration since the 1990s leading to more frequent exceedance of flood threshold levels, increasing the probability of high tide flooding and enhancing the risk of extreme water levels along the coast of Texas and Louisiana. Understanding the changing risk associated with flood threshold exceedance, trends, and seasonality and the mechanisms that lead to increased frequency and magnitude of coastal flooding is of importance to community planners and policymakers. Here, the probability of flood threshold exceedance and the factors contributing to said exceedances are assessed. While sea level-enhanced storm tides represent the greatest risk to life and property, increased frequency of high tide flooding may prove to be a great disruption and cost to locations in the study area. In national assessments, the National Oceanic and Atmospheric Administration (NOAA) uses a common impact flood threshold level to estimate high tide flooding impacts for all U.S. assets. In this study, statistical and spectral analysis of hourly tige gauge data from 1980-2019 and site-specific flood threshold levels are utilized to analyze frequency and duration of high tide flooding and the tidal and non-tidal components that contribute to it. Results indicate an increase in high tide flooding days and hours, particularly since 2010, with the greatest increases at locations with higher tidal ranges, occurring seasonally (September-October) with main contributors from the seasonal mean sea level cycle driven by the annual and semiannual solar constituents and non-tidal residuals associated with storms. The National Hurricane Center Atlantic Hurricane Database and the Louisiana State University Gulf of Mexico Peak Surge Database were updated to include verified data through 2020 to examine trends in peak surge and tropical cyclone activity associated with non-tidal residuals. Return periods, estimated based on changes from the baseline (1930-1960) in frequency and magnitude of storm tides suggest an increase in the 100-year surge event from ~8 to ~10.5 meters. Atlantic tropical storms, hurricanes, and major hurricanes are increasing (Mann Kendall trend test p-value <0.05) and a positive correlation between the Atlantic Multidecadal Oscillation and Atlantic tropical cyclones is verified with Spearman correlation (p-value <0.05). However, results of these tests are not statistically significant to verify trends and correlations in frequency of landfalls and magnitude of surge in Texas and Louisiana. Additionally, the Tropical Hazard Index calculated over 40-year periods beginning in 1901 does not show a consistent increase indicating that relative sea level rise is contributing to increased storm tide magnitude observed in the surge record. A case study in which relative sea level rise scenarios based on probabilistic projections are added to storm tide modeled under current sea level conditions reveals the greatest increase in storm tide inundation risk due to relative sea level rise in the Baton Rouge, LA, area occurs with category 1 hurricanes, while in the Houston-Galveston, TX, area the greatest change in risk is associated with increased inundation from major hurricanes.

4.1 Introduction
4.1.1 Relative Sea Level Rise and Hide Tide Flooding Background

RSLR recorded by National Oceanographic and Atmospheric Administration (NOAA) tide gauges, is of interest to coastal populations and infrastructure because it combines the global sea

level rise (SLR) driven by climate change (e.g., thermal expansion, melting of ice sheet and mountain glaciers) with regional sea level effects driven by climate oscillation interactions at varying timescales, and local vertical land movement (VLM; Sweet and Park, 2014). Coastal locations in Texas and Louisiana experience RSLR rates greater than the global SLR average, by subsidence and thus there is high risk from storm and tide-driven flooding as the climate continues to warm. While coastal flooding from extreme storm tides is the greatest risk for coastal communities, the effects of high tide flooding (HTF), also referred to as nuisance flooding, poses an additional risk to these communities by means of road closures, disruptions to business, and damage to infrastructure (Thompson et al., 2021). HTF event rates, defined as exceedances over local NOAA National Weather Service (NWS) minor flood thresholds, are expected to accelerate on the U.S. East and Gulf coasts as RSLR continues to accelerate (Sweet and Park, 2014). Moreover, the duration of HTF events will extend over more hours and may cluster together for seasons or months causing greater cumulative effects (Thompson et al., 2021). In this study, NOAA NWS flood thresholds that have been determined by the Weather Forecast Offices (WFOs) and local municipal emergency managers and are defined as height above mean higher-high water (MHHW) tidal datum at each gauge station are utilized. Tidal datums are standard elevations, defined by the tides, specific to each NOAA tide gauge station and include mean lower low water (MLLW), mean low water (MLW), mean sea level (MSL), mean high water (MHW), and MHHW. Each station also has a standard datum defined as elevation zero and all datums reference the 1983-2001 national tidal datum epoch (Scherer et al., 2001). Figure 4-1 is an example of a NOAA tide gauge station water level time series with the tidal datum elevations and flood threshold elevation above MHHW. The difference between the flood threshold elevation and MHHW decreases with RSLR.
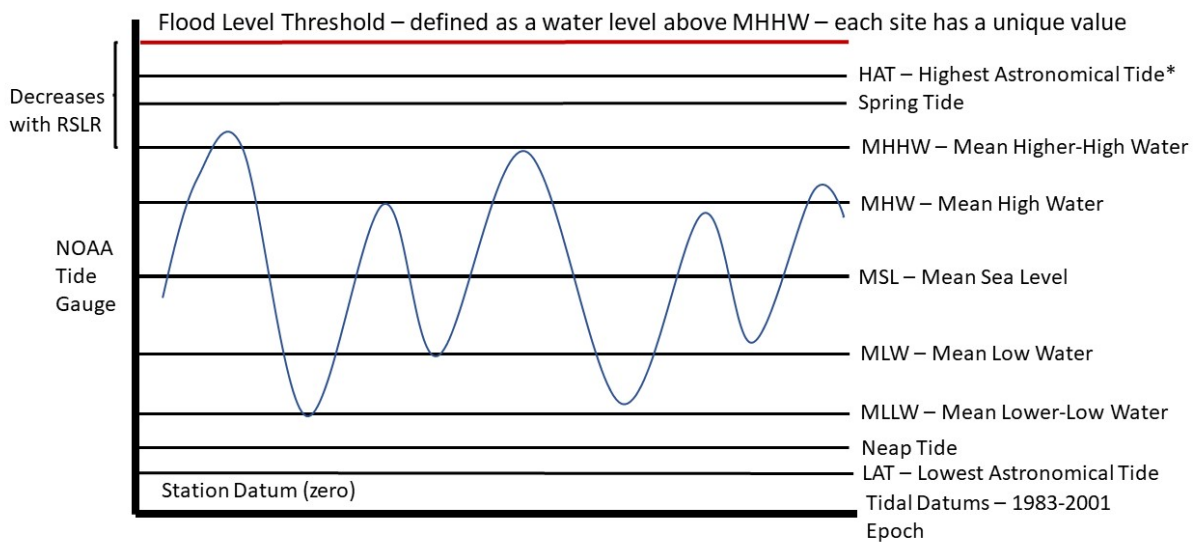
Figure 4- 1. Schematic of NOAA tide gauge water levels, tidal datums, and flood threshold level demonstrating how RSLR reduces the difference between MHHW and the flood threshold level. Figure adapted from Sweet and Park (2014).

Less than half of all NOAA tide gauges have official flood thresholds, therefore NOAA analyzes national HTF events using a common impact threshold or a derived flood threshold that may be greater or less than the official thresholds set by local WFOs (Sweet et al., 2018). HTF days estimated using the common thresholds are made available to the public via NOAA Tides and Currents Inundation Dashboard and are commonly used in risk analysis. In this study, the official flood thresholds determined by local knowledge of infrastructure vulnerabilities, topography, land cover, and existing flood defenses will be used to avoid either an overestimation or underestimation of the impacts of HTF.

At each tide gauge location, observed water levels result from a combination of a seasonal MSL cycle often influenced by variations in climatic forcings linked to El Niño Southern Oscillation (ENSO) and other climate oscillations, the astronomical tide, and a nontidal residual (NTR) associated with ocean and atmospheric forcing. The seasonal MSL component is caused by the combined effects of seasonal changes in atmospheric pressure, winds, ocean temperature and currents, salinity, and river discharge and is often driven by steric density changes of the water due to temperature and salinity (Zervas, 2006). Although annual MSL and HTF at locations along the U.S. West Coast and Northeast Coast have shown connections to ENSO and the North Atlantic Oscillation (NAO), these effects are not seen in the GOM (Sweet et al., 2014). The double peaked seasonal MSL cycle observed along the Texas and Louisiana coasts is lowest in January with a secondary peak in May-June, a secondary low in July-August and a rise to a maximum peak in September-October.

The tidal component of the observed water levels consists of the astronomical, otherwise known as gravitational tides and the shallow water tides known as overtides that are affected by tidal friction between the tide and sea floor. Tidal analysis and prediction are achieved using spectral analysis to decompose the signal into its individual harmonic constituents. These are primarily diurnal and semidiurnal, but also include solar annual and semiannual (Sa and Ssa) constituents as well as the higher frequency overtide constituents (Zervas, 2006). The long-period solar constituents are modulations of the astronomical tides. The annual Sa tide modulation is generated by the yearly varying distance between the earth and sun due to eccentricity of earth's orbit around the sun. The semiannual Ssa tide modulation is due to earth's tilt and the sun's biannual movement away from the equator (Ray et al., 2021). The Sa and Ssa components influence the seasonal MSL cycle. While as many as 37 constituents may exist, analysis of the eight largest astronomical tides (see Table 4-1) will encompass 95% of the full tidal range (Devlin et al., 2018). As sea levels rise, tidal friction rises with an increase in inundation on low-sloping coastlines of Texas and Louisiana, leading to increased amplitude of the overtide constituents and thus are relevant to include in analysis.

Table 4-1. The eight largest tidal constituents and their definitions.

Semidiurnal		*Diurnal*	
Name	**Constituent**	**Name**	**Constituent**
M_2	Principal lunar	K_1	Lunisolar diurnal
S_2	Principal solar	O_1	Lunar diurnal
N_2	Larger lunar elliptic	Q_1	Larger lunar elliptic
K_2	Lunisolar	P_1	Solar diurnal

The NTR component of the observed water levels represents the remainder after the seasonal MSL cycle and astronomical tides are removed. The NTR in the GOM significantly contributes

to high water levels but displays no seasonal variability except for the occasional late-summer/early-fall spike resulting from tropical cyclone activity (Sweet et al., 2014). These peaks in NTR occur concurrent to the maximum peak of the seasonal MSL cycle, exacerbating the effects of storm surges.

Tidal anomaly correlation of tidal and overtidal constituents with MSL variability are negative at gauge stations in the study area, meaning changes in tidal heights oppose MSL fluctuations and rising seas result in negative feedback from the shallow water overtides (Devlin et al., 2018). Thus, the NTR component, dominated by seasonal tropical cyclone activity, is of importance when analyzing HTF and extreme water levels in Texas and Louisiana.

4.1.2 Risk of Increase in Storm Surges by Rise in Tropical Storms Frequency and Magnitude on Regional Sea Level Rise in the GOM

In the following the impact of tropical storms on regional sea level rise is discussed. Tropical cyclones are low pressure, warm-core storms with cyclonic motion and strong winds that form over warm waters in the tropics. Tropical cyclones are categorized using the Saffir-Simpson scale based on sustained wind speeds as seen in Table 4-2. Tropical cyclones are a seasonal phenomenon and the NOAA National Hurricane Center (NHC) "Atlantic hurricane season" begins on June 1 and ends on November 30 with the first named storm typically forming in June, the first hurricane in early to mid-August, and first major hurricane forming in late-August to early-September (NHC, 2021). Note that historically about 70% of Atlantic basin tropical cyclones from 1851 to 2009 occurred in the Gulf of Mexico or the Caribbean Sea (Biasutti et al., 2012). Hurricane frequency is also influenced by year-to-year variations that are common due to climate factors such as El Niño Southern Oscillation (ENSO), Atlantic Multidecadal Oscillation, North Atlantic Oscillation, and other oscillations.

Table 4-2. Saffir-Simpson Scale (Simpson and Riehl, 1981).

Category	m/s	knots	mph	km/h
Tropical Depression	< 17	< 34	< 38	< 62
Tropical Storm	18-32	35-63	39-73	63-118
One	33-42	64-82	74-95	119-153
Two	43-49	83-95	96-110	154-177
Three	50-58	96-112	111-129	178-208
Four	58-70	113-136	130-156	209-251
Five	> 70	> 137	> 157	> 252

Tropical cyclones make landfall on the Texas and Louisiana coast. Favorable conditions for formation of tropical storms are sea surface temperature (SST) greater than ~26.5 °C, latitudes away from the equator, and vertical wind shear of horizontal winds is weak influenced (Emanual, 2008). In the Atlantic Ocean, suitable conditions for tropical storm formation can be also attributed to a shallow disturbance in easterly trade winds also known as easterly wave. While most Atlantic tropical cyclones form from easterly waves, any low-level disturbance with sufficient vorticity and convergence, such as fronts or outflow boundaries can initiate tropical cyclogenesis (Landsea, 1993).

Various arguments have been made suggesting anthropogenic climate change has significant influence on tropical cyclone activity. Recent research suggests a poleward migration of tropical cyclone tracks related to expansion of the Hadley circulation results in decreased distance from

land that the storm reaches maximum intensity and increasing landfalls (Wang and Tuomi, 2021). Hurricane translation speed has also garnered much attention since Hurricane Harvey stalled over Harris County, Texas, in 2017 and caused significant and widespread flooding (Blake and Zelinsky, 2018). Conclusions regarding how global warming affects translation speed are mixed with some studies determining that translation speeds are slowing (Kossin, 2018) while others forecast an increase with warming (Yamaguchi et al., 2020). A region-specific study of steering winds indicates an increase of northward steering winds June through September in Texas by the end of the century that results in faster northern movement of landfalling tropical cyclones (Hassanzadeh et al., 2020). Greater consensus emerges in the discussion of how warming increases the water vapor capacity of the atmosphere resulting in increased precipitation rates globally and increased rain rates at the center of tropical cyclones (Emanuel, 2006; Hartmann et al., 2013). Although some research indicates an increase in tropical cyclone frequency (Emanuel, 2013), Atlantic basin tropical cyclone frequency is projected to decrease slightly while the intensity of the storms will increase and the proportion of category four and five hurricanes will also increase (Hartmann et al., 2013; Knutson et al., 2020).

4.1.3 Risks of Increasing Hurricane and Surge Return Periods

The probabilities of recurrance for storm surges, known as return periods or recurrance intervals, estimate the average time betweeen storm surge of certain magnitudes such as the 100-year and 500-year return periods. Hurricane return periods calculated for the Gulf of Mexico with respect to wind speeds equivalent to the strength of of a category 5 storm (such as e.g. Hurricane Rita or Katrina) can be expected to occur every 21 years somewhere along the Gulf coast from Texas to Alabama (Elsner et al., 2006). Tropical storm, hurricane, and major hurricane return periods calculated from Texas to Maine gives similar results, estimating that a major hurricane should be expected to effect Texas and Louisiana sites every 26-52 years depending on the specific location (Keim et al., 2007). These results are also similar to the NHC's estimated return periods for major hurricanes using data to 2010 as seen in Figure 4-2 (Neuman, 1987).

While hurricane return periods are useful for estimating winds, other factors such as size of the storm, storm track, slope of the coast, tides, and bottom friction that affect the magnitude of the storm surge are not accounted for in these estimations (Harris, 1963). Peak surge return periods for the Gulf of Mexico using the SURGEDAT database developed at Louisiana State University were calculated using data up to 2011 for the 100-, 50-, 25-, and 10-year return periods summarized in Table 4-3 (Needham, 2014).

Table 4-3. Estimated Peak Surge Return Periods for the Gulf of Mexico (Needham, 2014).

Return Period (yrs)	100	50	25	10
Surge Height (m)	8.1	7.15	6.25	4.96
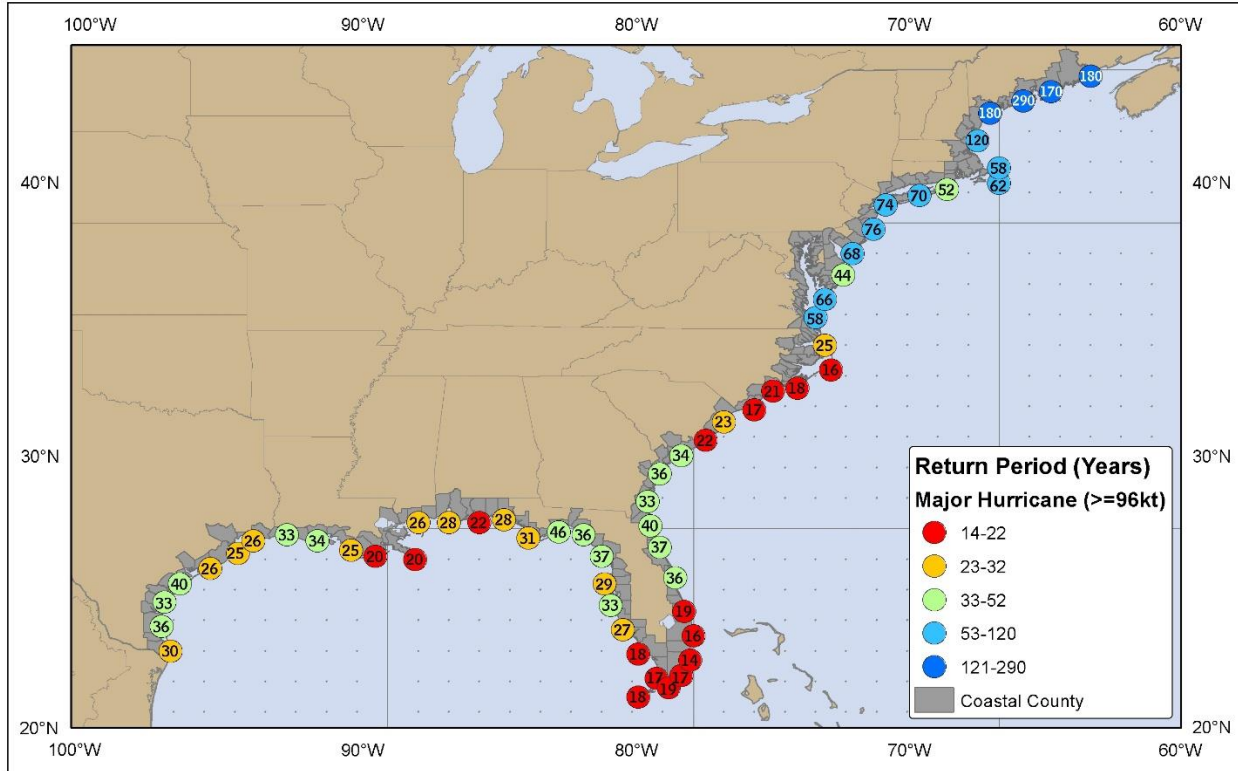
Figure 4- 2. Estimated return periods for major hurricanes (category 3 or above) from Texas to Maine from NOAA National Hurricane Center based on data form 1850-2010 (NHC, 2011).

4.1.4 Coastal Risk from Tidal Surge in the Northern GOM

While HTF in the Gulf of Mexico are gradual increasing, extreme water levels produced by tidal surges represent the most damaging and life-threatening risk in coastal locations. Maximal tidal surges occur when the tropical cyclone or hurricane-produced storm surge is combined with spring high tide. Storm surges are characterized by a combination of a wind-driven onshore current, waves that carry added shoreward momentum, runoff from heavy precipitation, low pressure-driven hydrostatic sea level rise (~1 m SLR per 100 hPa depression of pressure), and a tidal component that can either increase or reduce the strength of the surge (Wallace and Hobbs, 2006). While tidal forecasts are well defined the exact timing when a tropical storm makes landfall remains uncertain (Wahl, 2017). RSLR reduces the gap between MSL and site-specific flood threshold elevations resulting in increased probability that lower magnitude storm tides will increasingly affect flooding over time (Sweet et al., 2014). A storm surge modeling study of southeast Louisiana found that, using hypothetical storms that produce 100-year water levels, in areas of maximum surge the impact of RSLR on surge was largely linear, or equal to the RSLR, while in areas of moderate surge, the impact of RSLR doubles the surge height (Smith et al., 2010). However, analysis of observed data indicates trend differences in MSL and extreme water levels. Hence, an assumption of linearity in these trends could lead to substantial errors in the estimation of storm surge heights. For example, studies utilizing three-dimensional numerical ocean general circulation models (e.g., Arns et al., 2015) suggest that a 0.54 m of mean SLR can produce storm surges that are 0.15 m higher in the shallowest areas.

4.1.5 Climatic Variability and Surge Activity

While it has been shown that ENSO and the NAO have insignificant effects on MSL and HTF in the GOM, these climate variabilities, as well as the Atlantic Multidecadal Oscillation (AMO), do have some effects on tropical cyclone activity in the Atlantic basin (Pielke and Landsea, 1999; Emanuel and Mann, 2006; Colbert and Soden, 2012). ENSO affects the Atlantic basin remotely by changing the atmospheric circulation. During El Niño phases, upper tropospheric westerly winds increase the vertical shear over the basin contributing to a reduction in the number of tropical cyclones during hurricane season. La Niña phases are characterized by low wind shear and a less stable atmosphere that leads to an increase in tropical cyclone activity in the Atlantic (Piekle and Landsea, 1999). The NAO primarily affects the tracks of Atlantic basin tropical cyclones through an enhanced Bermuda High (Azores High) during positive phases that steers tropical cyclones closer to the coast thus enhancing the risk of landfall during that hurricane season (Colbert and Soden, 2012).

The AMO is characterized by SST anomalies in the Atlantic that occur over many decades as warm phases and cold phases that are believed to be due to internal variability of the ocean-atmosphere system (Schlesinger and Ramankutty, 1994). Warm phases of the AMO are characterized by warm tropical Atlantic SSTs linked to enhanced number and intensity of tropical cyclones while cold phases have the opposite effect. Recent studies have concluded that there is no evidence that the AMO is a result of internal oscillations within the climate system but rather a result of competing radiative forcings from anthropogenic greenhouse gases and sulfate aerosols (Emanuel and Mann, 2006; Booth et al., 2012; Cane et al., 2017; Mann et al., 2021). Others have concluded that the AMO is a climate system related oscillation that has been amplified since the industrial era (Moore et al., 2017). Atlantic tropical cyclone activity is linked to a positive phase of the AMO (Saunders and Lea, 2008). A higher occurrence of tropical storms has been attributed to La Niña, a positive NAO, and warm AMO conditions. Trends in future tropical storm frequency attributed to changes in ENSO, the NAO, and the AMO (see IPCC AR5, 2013) remain controversial.

4.2 Objective

This study aims to determine if the probability of high tide flooding is increasing in Texas and Louisiana and assess the factors contributing to flood threshold exceedance. As part of this study, the analysis of the tidal components and site-specific flood threshold levels and their changes will be extended for hourly and daily HTF events (Sweet et al., 2014) from relevant tide gauge stations in Texas and Louisiana for the period from 1980 to 2019. Additionally, this paper intends to determine whether RSLR is the main driver of increased risk from storm tide inundation in this area or not. Furthermore, this study attempts to estimate new peak surge return periods based on changes in frequency and magnitude of storm tides to the historical baseline (1930-1960) and to assess climate oscillations and changes in tropical cyclone climatology. A case study will present the addition of RSLR scenarios to modeled storm surge with the objective of identifying areas of increased risk of inundation from hurricanes by 2100 and locating socially vulnerable populations residing within those areas.

4.3 Methodology
4.3.1 High Tide Flooding

Hourly water level data recorded by NOAA tide gauges was collected for the years 1940, 1960, 1980, 2000, and 2020, or as far in the past as the tide gauge record allows, to capture the

evolution of water levels over the past decades. Tidal datum elevations of mean lower low water (MLLW), mean low water (MLW), mean sea level (MSL), mean high water (MHW), and mean higher high water (MHHW) were obtained from NOAA relative to the 1983-2001 (NAVD88) tidal datum. Flood threshold elevations were acquired from NOAA Advanced Hydrological Prediction Systems (AHPS). The maximum daily water levels were computed from the hourly data and fit to the Generalized Extreme Value (GEV) distribution. The scale, location, and shape parameters of the GEV distribution were estimated using routines in MATLAB. The probability density functions (PDFs; *f(x)*) of the maximum daily water levels were calculated using the equation (eq. 4.1),

$$y = f(x|k, \mu, \sigma) = \left(\tfrac{1}{\sigma}\right) \exp\left\{-\left(1 + k\,\tfrac{(x-\mu)}{\sigma}\right)^{-\tfrac{1}{k}}\right\}\left(1 + k\,\tfrac{(x-\mu)}{\sigma}\right)^{-1-\tfrac{1}{k}} \qquad (4.1)$$

where σ denotes the scale parameter, μ is the location parameter, k is the shape parameter, and x denotes the water level. The PDFs were plotted together with the station's unique flood threshold levels to analyze how water levels have increasingly approached the threshold for high tide flooding over the past decades.

Hourly water levels recorded by NOAA tide gauges relative to the 1983-2001 datum epoch were collected from stations in Texas and Louisiana that had at least 30 years of verified data (Table 4-4). Analysis of HTF hours above the flood threshold was conducted from 1980-2019 to quantify frequency and duration of HTF events. The total number of hours above the threshold were summed for each year of the analysis. HTF days were also calculated to diminish the influence of storms exceeding the threshold for many hours. Annual MSL trends were included to compare trends in HTF to trends in RSL. The results were plotted with NOAA's estimated HTF days calculated using a common impact threshold rather than the station's unique flood threshold.

To investigate the significance of the oceanic processes that lead to HTF events, spectral analysis of hourly tide gauge data was conducted for all locations in Texas and Louisiana over the same 40-year period (1980-2019) used in hourly HTF analysis. Using tidal harmonic analysis functions in MATLAB (Codiga, 2011), the data was decomposed into a seasonal MSL signal (Sa and Ssa tidal constituents) and the eight largest astronomical tides (Table 4-1) after Sa and Ssa are removed. What remained was the NTR component. The 40-year hourly predicted tides, MSL cycle, NTR, and maximum observed water levels were calculated for each calendar day of the year and a 30-day smoothing was imposed to focus on patterns rather than single occurrences. The components were then plotted together with the tide gauge station's unique flood threshold levels to analyze contributions to high tide flooding. While worthy of future investigation, analysis of the overtide constituents is considered beyond the scope of this study.

Table 4-4. NOAA tide gauge locations used in analysis with station name, location, and year established. MSL trends (mm/yr) and NOAA AHPS flood threshold levels (m above MHHW).

NOAA Tide Gauge	Station ID	Latitude	Longitude	Year Established	MSL Trend (mm/yr)	Flood Threshold (m, MHHW)
Port Isabel, TX	8779770	26.065	-97.215	1944	4.25	0.34
Corpus Christi, TX	8775870	27.580	-97.217	1983	5.54	0.40
Rockport, TX	8774770	28.022	-97.047	1937	5.94	0.67
Galveston, TX	8771450	29.310	-94.793	1904	6.62	0.79
Sabine Pass, TX	8770570	29.728	-93.870	1985	6.16	0.58
Grand Isle, LA	8761724	29.263	-89.957	1979	9.18	0.51

4.3.2 Tropical Cyclone and Storm Surge

Tropical cyclone frequency, location, and magnitude from 1851-2015 were obtained from NOAA's Atlantic Hurricane Database (HURDAT2; Landsea et al., 2015) and categorized as Tropical Storms, Hurricanes, and Major Hurricanes (> 50 m/s wind speed) for trend analysis using linear regression and a 10-year moving average. NHC's tropical cyclone reports were used to update the dataset to the most recent verified year of 2020 to include this particularly active year in analysis. Total Atlantic tropical cyclones that made landfall were analyzed as well as those that only made landfall in Texas and Louisiana. The Mann Kendall trend test was utilized to test the null hypothesis that there is no trend in the time series.

Storm surge/tide peak height and location data for 1880-2011 was obtained from Louisiana State University's Gulf of Mexico Peak Surge Database (Needham and Keim, 2012) and updated using NHC's verified tropical cyclone reports for the remaining years to the present using the maximum surge heights for storms that made landfall in Texas and Louisiana.

4.3.3 Climate Variabilities

To qualify connections between trends in Atlantic tropical cyclone activity and climate oscillations, a simple analysis of the number and severity of tropical cyclones was conducted for different phases of said oscillations. The AMO index timeseries was collected from NOAA Physical Science Laboratory (PSL) and categorized into cold phases (1900-1925; 1963-1994) and warm phases (1923-1962; 1995-2020). The number of total tropical storms, hurricanes, and major hurricanes (defined as Saffir-Simpson category 3 or higher) were summed for each time period. The same procedure was used for storms that made landfall in Texas and Louisiana. The AMO index timeseries was plotted with the 10-year moving averages of Atlantic basin tropical storms and hurricanes to further visualize the trends. Correlation between the AMO and Atlantic tropical cyclone activity as well as with landfalling tropical cyclones was calculated using the Spearman correlation coefficient. To analyze the effects of ENSO, the Multivariant ENSO Index (MEI) was obtained from NOAA PSL and categorized into cold (La Niña), neutral, and warm (El Niño) years. The number of tropical storms, hurricanes, and major hurricanes, as well as Texas and Louisiana landfalling storms were summed for each year.

4.3.4 Return Periods

Peak surge return periods were calculated using data from the SURGEDAT Gulf of Mexico database (updated to 2020 using NHC tropical cyclone reports) excluding all data from states besides Texas and Louisiana. All surge values were ranked to construct a partial duration series of peak surge heights of the last 120 years. Data prior to 1900 was excluded due to uncertinty, but data from 1900 to present was used to ensure the Great Galveston Hurricane of 1900 was included. The 120-year series contained the the 120 largest storm surges or storm tides with largest magnitude being 8.53 m from Hurricane Katrina (2005) and the smallest being 0.76 m from Hurricane Edith (1971). Peak surge return periods from the updated record were estimated using logarithmic plotting methods used in many return period studies (Huff and Angel, 1992; Needham, 2010; Needham, 2014). The exceedence probability was determined using the Weibull plotting position following the equation (4.2)

$$Exceedence\ Probability = \frac{Rank}{n+1} \tag{4.2}$$

where n is the number of years in the dataset. Return periods were calculated using equation 4.3

$$Return\ Period = \frac{1}{Exceedence\ Probability} \tag{4.3}$$

and plotted using a log scale with magnitude on the y-axis and return period on the x-axis. A logarithmic regression was performed and resulting equation used to determine the 500-, 100-, 75-yr, 50-yr, 25-yr, and 10-yr return periods.

Changes is frequency and magnitutde of peak surge were evaluated using 30-year averages over the peak surge series beginning with 1900-1930 and ending with 1990-2020. Percent change in frequency and magnitude was calculated using the present 30-year average and the 30-year average from 1930-1960 due to data availability problems asociated with the 1900-1930 time period and possible magnitude bias from the Great Galveston Hurricane of 1900. Percent change calculations were used to adjust return periods relative to the most recent time period to examine what future return periods may estimate following the formulas (eq. 4.4)

$$T_2 = \frac{\lambda_1}{\lambda_2} T_1 \ and \ \eta_2 = \eta_1 \frac{P_2}{P_1} \tag{4.4}$$

where T is the return period, λ is the rate of storm occurrence per year, η is surge magnitude, P is the peak surge height, subscript 1 represents the 1930-1960 averages, and subscript 2 represents the 1990-2020 averages.

To investigate changes in tropical storm return periods from 1900 to 2020, the Tropical Hazard Index (THI; Keim and Muller, 2007) was calculated based on frequency and severity of storms over 40-year periods beginning in 1901 and ending in 2020. The index is derived by the summation of all storms during the time periods where a tropical storm landfall is given two points, category 1-2 hurricanes are given four points, and category 3-5 storms are given eight points. Along with the six tide gauge stations used in this study, two additional sites (Freshwater Canal Locks, LA, and Matagorda City, TX) were chosen to fill out spatial gaps in coverage. Utilizing NOAA's historical hurricane tracks, a search was conducted for each location to determine the number of tropical storms, hurricanes, and major hurricanes that struck each location. Using a conservative assumption of storm size and total swath of winds, tropical storm-

force winds would extend 80 km to the right of the center and 40 km to the left of the track, while hurricane and major hurricane-force winds would extend further from center. Assuming this and following the methodology of Keim and Muller (2007), a 120 km search diameter was used for tropical storms, while a 240 km and 360 km search diameter was used for hurricanes and major hurricanes respectively. The THI was calculated and mapped using graduated pie charts with each slice representing individual categories and the total size of the pie determined by the total THI.

4.3.5 Case Study: Storm tide with RSLR mapping risk for vulnerable populations on Texas and Louisiana coasts.

To visualize storm tide inundation area and height above ground, as well as the risk to vulnerable populations, a case study was conducted in the area just west of the leveed city of New Orleans, LA, west along the Interstate 10 corridor to Baton Rouge, LA, and the Houston/Galveston, TX, area. Although these areas were chosen for the case study, the same methods can be applied to any area along the Gulf coast. Since the latest version of the NHC's National Storm Surge Risk Maps (Version 3, 2022; Zachry et al., 2015) includes all of Louisiana and Texas, the downloadable GIS data for storm tides was utilized. The map layers were developed by NHC using SLOSH model output for tens of thousands of hypothetical tropical cyclones for each basin and storm tides were a composite of Maximum Envelopes of Water (MEOWs) and Maximum of MEOWs (MOMs; see also Chapter 2.1.3). A 10-meter resolution USGS Digital Elevation Model (DEM) and major roads maps were overlaid with the category 1, 3, and 5 storm tidal maps. To identify vulnerable populations within the inundated areas, the Center for Disease Control's (CDC) Social Vulnerability Index (SVI) was included in the study. The SVI 2018 applied 15 variables under four categories at the US census tract level: (1) socioeconomic status, (2) household composition and disability, (3) minority status and language, and (4) housing type and transportation. In this study, tracts that have at least 2500 estimated population in the top 10%, or 90th percentile, for the following variables were utilized to identify tracts with vulnerable populations: (1) below poverty, (2) age 65 or older, (3) age 17 or younger, (4) civilians with disabilities, (5) mobile homes, (6) no vehicle. Tracts were classified as vulnerable if up to 3 variables applied, very vulnerable for 4-5 variables, and extremely vulnerable with >5 variables in the top 10%. To analyze storm tides enhanced by sea level rise, RSLR scenarios (Intermediate: 1.79 m, Intermediate-High: 2.46 m, Extreme: 3.78 m) for 2091-2100 based on probabilistic projections (Chapter 3, Figure 3-9) were applied to the storm tide map layers in GIS using raster calculations of the DEM. The probabilistic scenarios are centered at the midpoint of the 1991-2009 epoch (2000) and are based on representative concentration pathways (RCPs). The intermediate scenario is based on the high end of the *very likely* range under RCP4.5; the intermediate-high scenario is based on the middle of the *likely* range under RCP8.5 and the extreme scenario is consistent with estimates of physically possible worst case (see chapter 3, Table 3-2). The scenarios were chosen based on probability of exceedance of less than 50% established by the work of Kopp et al. (2014; see chapter 3, Table 3-7). While this method assumes a linear relationship between storm tide height and sea level rise that may under- or overestimate the influence of SLR on storm tides, the topography of the region suggests the area of inundation is restricted even under the most extreme RSLR scenarios.

4.4 Results
4.4.1 High Tide Flooding: PDFs
    In this section, HTF based on exceedance of the flood threshold levels and the progression of MSL at the center of the density is presented. The GEV PDFs of hourly water levels of the Galveston Pier 21 tide gauge for specified years (Figure 4-3) demonstrates the evolution of these water levels over the past 80 years relative to the current tidal datums and minor flood threshold elevation. The increase in MSL over time is represented at the centers of density and upper tails include water levels above the great diurnal range defined as the difference between MLLW and MHHW.

Figure 4- 3. PDFs of hourly water levels measured at Galveston Pier 21 NOAA tide gauge station for 1940 (blue), 1960 (green), 1980 (pink), 2000 (magenta), and 2020 (red) plotted with the minor flood threshold elevation (black dashed line).

Figure 4-4 shows PDFs of hourly water levels measured at Rockport, Texas, NOAA tide gauge for 1980, 2000 and 2020 are similar to Figure 4-3. For this location, MSL and extreme water levels approaching or exceeding the flood threshold have been increasing over the past 40 years.

Figure 4- 4. PDFs of hourly water levels measured at Rockport NOAA tide gauge station for 1980 (pink), 2000 (magenta), and 2020 (red) plotted with the minor flood threshold elevation (black dashed line).

The PDFs of hourly water levels for Port Isabel (Figure 4-5) from 1960, 1980, 2000, and 2020 indicate a significant increase in water levels exceeding the flood threshold in the last 60 years. With the center of the density approaching the flood threshold level in 2020, Port Isabel may experience a considerable increase in HTF days in the coming decade. Seen in the PDFs for 1980 for the three locations are the many hours spent above the flood threshold that year due to the influence of category 5 Hurricane Allen that made landfall near Port Isabel. With the center of the density representing MSL, 1980's MSL was lower than the modern day, and this demonstrates the risk of exceeding the flood threshold from hurricane storm surge will certainly increase as MSL increases with RSLR.

While Grand Isle, LA, Sabine Pass, TX, and Corpus Christi, TX, tide gauges did not record hourly data for 1940, 1960, and 1980 and were therefore excluded from PDF analysis, analysis in the coming sections will provide more information on HTF at these locations.
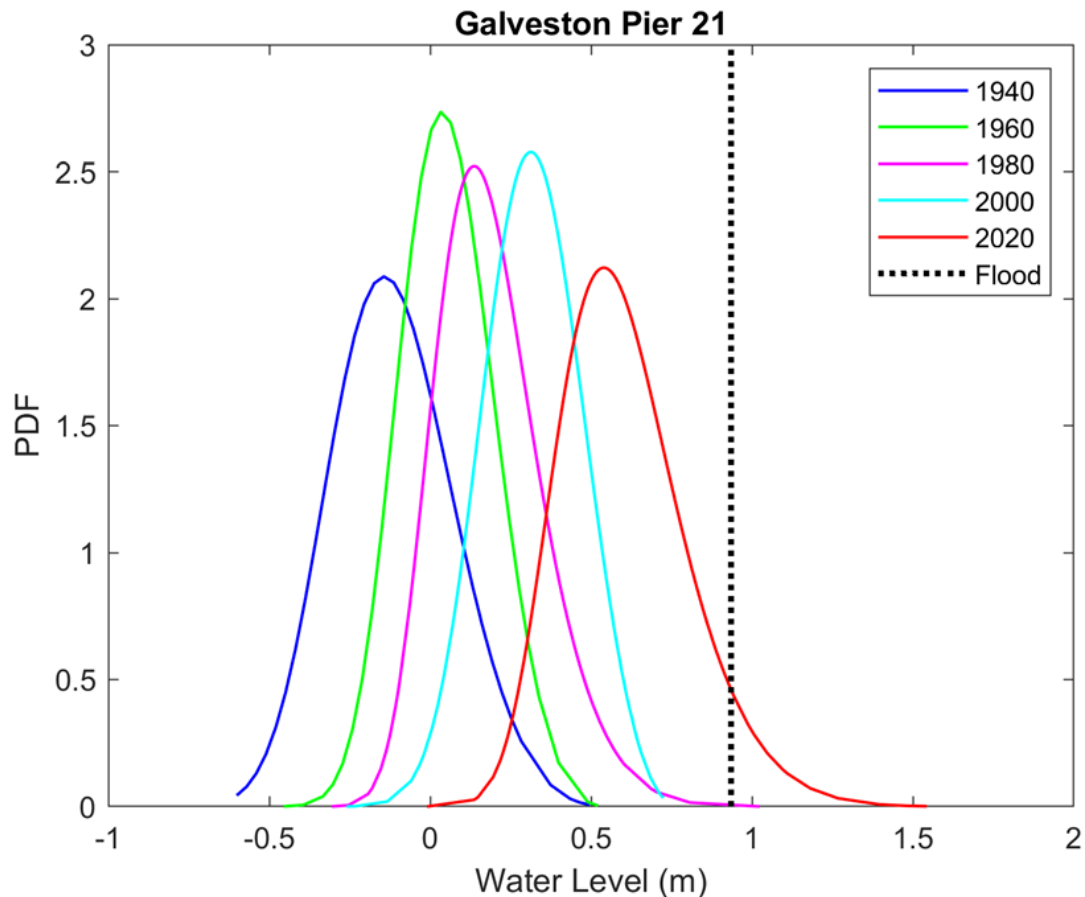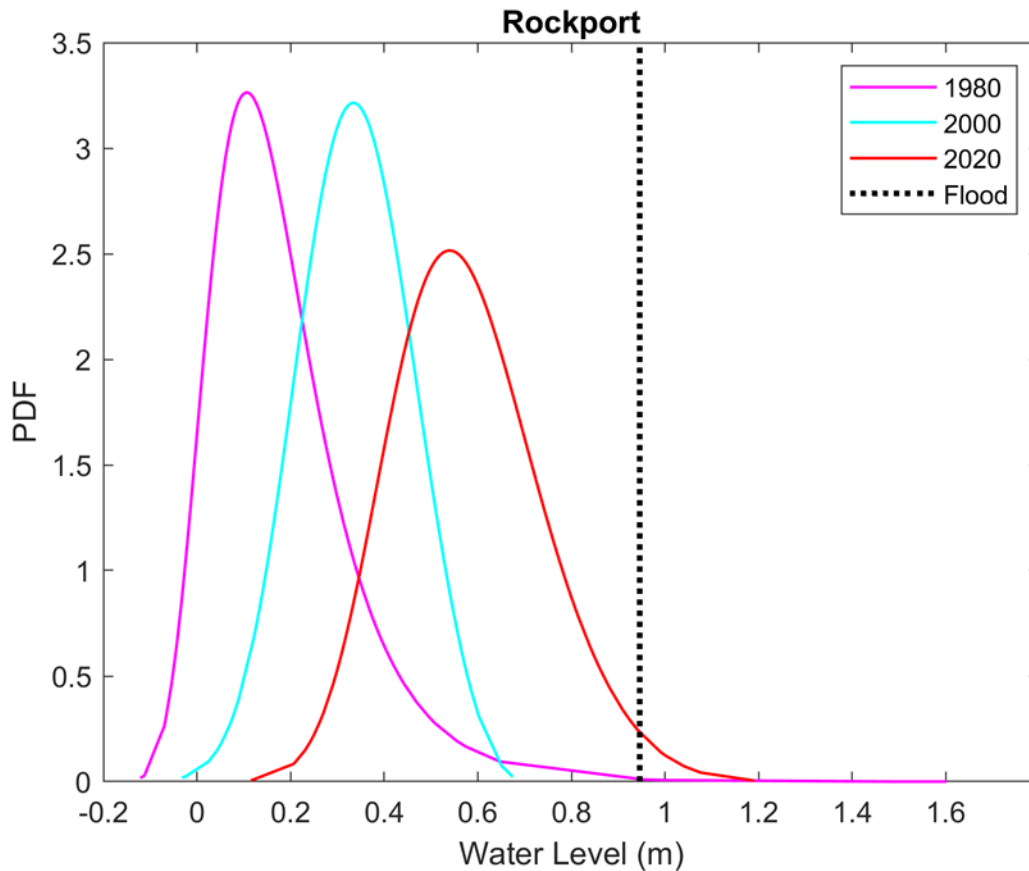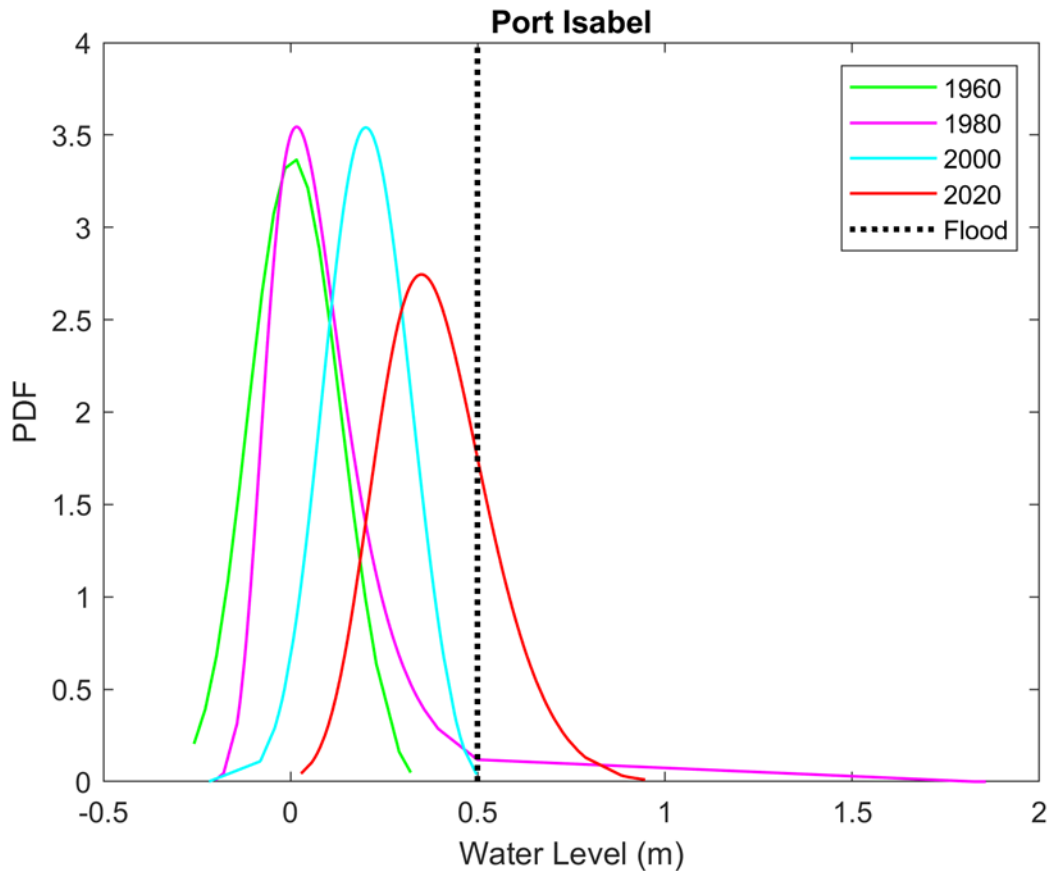
Figure 4- 5. PDFs of hourly water levels measured at Port Isabel NOAA tide gauge station for 1960 (green), 1980 (pink), 2000 (magenta), and 2020 (red) plotted with the minor flood threshold elevation (black dashed line).

4.4.2 High Tide Flooding Days and Hours

To quantify frequency and duration of HTF and analyze oceanic processes that lead to it, in this section, the results of analysis of hourly tide gauge data for HTF days and hours as well as the spectral analysis of processes influencing HTF are presented. The total annual HTF days at selected tide gauge locations that have defined flood threshold levels are presented in Figure 4-6 from 1940, or when measurements began, to present. It is evident from the data that frequency of HTF days is increasing over the past 80 years at most selected locations with an observable acceleration of frequency since the 1990s. Although RSLR rates are fastest at Grand Isle and Galveston due to subsidence, HTF days are defined by exceedance of a unique defined flood threshold at each location which may be significantly different based on topography and tidal range of the location. As listed in Table 4-4, Port Isabel and Corpus Christi have substantially lower flood thresholds (0.34 and 0.4 m above MHHW respectively) than Grand Isle (0.51 m), Sabine Pass (0.58 m), Galveston Pier 21 (0.79 m), and Rockport (0.67 m). With Grand Isle and Rockport's great diurnal tide ranges (0.323 and 0.111 m respectively) being lower than Sabine Pass (0.488 m), Galveston (0.429 m), Corpus Christi (0.499 m), and Port Isabel (0.418 m), fewer exceedance days are recorded at those locations. Therefore, the greatest increase in HTF days since the 1990s are observed at the locations with higher tidal ranges and lower defined flood thresholds such as Corpus Christi and Port Isabel.
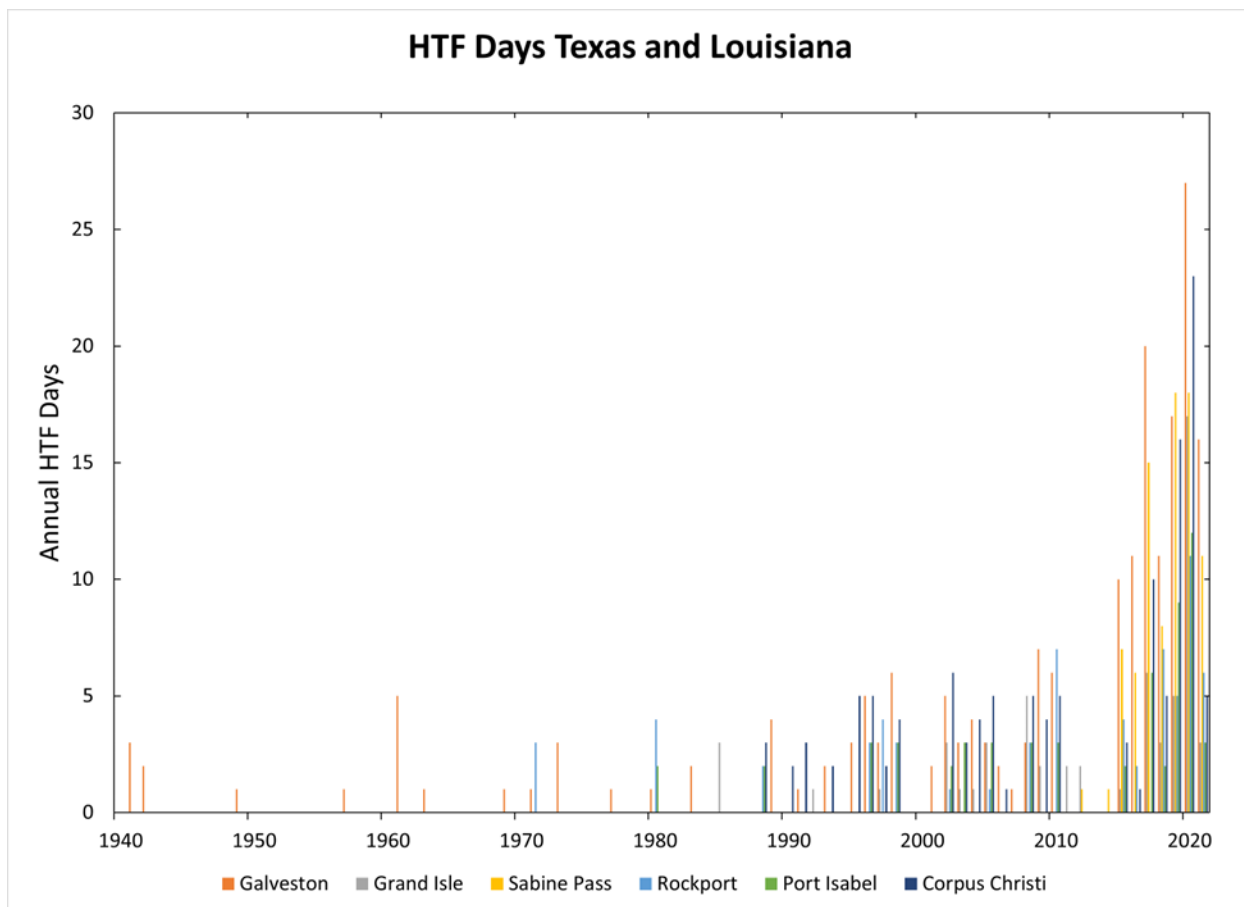
Figure 4- 6. Total number of HTF days (defined as any day with one or more hourly water levels above the flood threshold) per year from 1940 to present at selected tide gauge stations in Texas and Louisiana.

Figure 4-7 displays the analysis of HTF hours and days as well as the MSL trend at the Galveston Pier 21 tide gauge from 1980-2019. The number of hours and days of HTF have increased, particularly over the last decade. The influence of long-lived storms can be seen in the number of hours above threshold in 2017 because of Hurricane Harvey and in 2008 because of Hurricane Ike. While the hours of HTF are biased by these storms, the number of days with at least one hour of levels above threshold show an increasing trend with the increase in RSL observed by the tide gauge. In Galveston, HTF days are estimated by NOAA using a common impact threshold of 0.52 m above MHHW. This value is lower than the flood threshold set by local authorities and WFOs (0.79 m above MHHW), leading to higher HTF events than those calculated using the unique threshold. Note that data from NOAA's Inundation Dashboard (https://tidesandcurrents.noaa.gov/inundationdb) generally exceed the total HTF in days per year compared to this study.

Results of spectral analysis of hourly tide gauge measurements at Galveston Pier 21 presented in Figure 4-8 show the maximum observed water levels for each calendar day of the year deconstructed into a tidal component, the seasonal MSL cycle, and the NTR. The double peaked seasonal MSL cycle is a result of the solar annual and semiannual (Sa and Ssa) tidal constituents
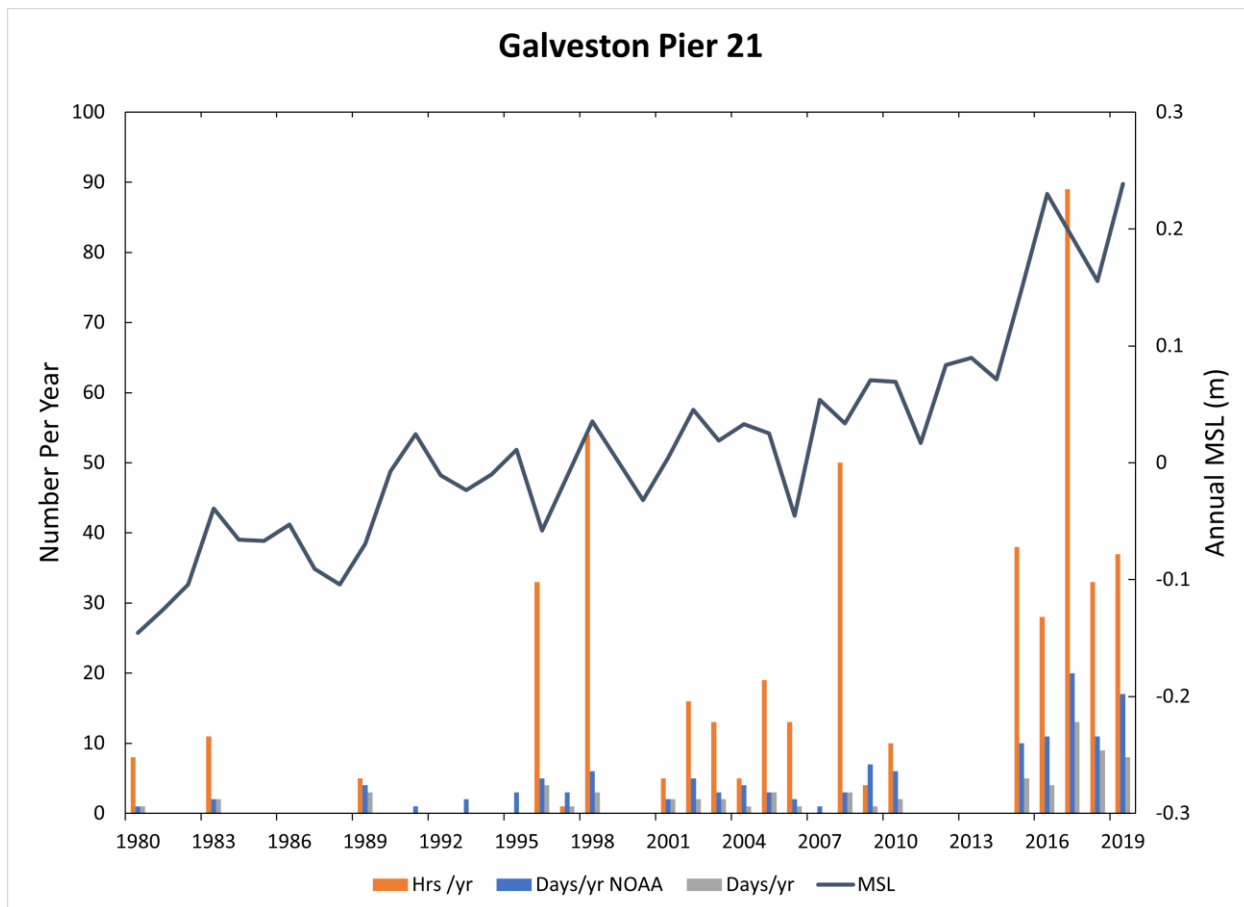
Figure 4- 7. HTF days (gray), HTF days estimated by NOAA (blue), and total hours above flood threshold (orange) with annual MSL for Galveston, Texas from 1980 to 2019.

and the tidal component results from the eight most influential tidal constituents (excluding Sa and Ssa). The season with the highest frequency of HTF in Texas and Louisiana is late-summer/early-fall, coinciding with the peak of hurricane season and exacerbated by the peak in seasonal MSL driven by solar constituents. The tidal component is out of phase with the other spectra, but its diminishing influence is negligible while the NTR, influenced by storms and nearby swells, greatly influences high water levels during this season. Together, the seasonal MSL cycle and the NTR are responsible for the peak in observed maximum water levels in September-October.

All locations in the study area reflect maxima in water levels during September-October. There is minor exceedance of the flood threshold value of smoothed observations from Grand Isle and Rockport's NOAA tide gauge stations (Figures 4-9 and 4-10) that indicate little flood threshold exceedance over the past 40 years, although individual events over the same time period have certainly caused flooding at these locations. This is a result of the smaller tidal ranges at these locations and does not indicate a lower risk of future HTF as the RSLR rates at these locations are higher than average due to subsidence.

Analysis of observed maximum water levels for Port Isabel and Corpus Christi (Figure 4-10) reveal HTF that occurs both in spring and fall with the highest peak in September-
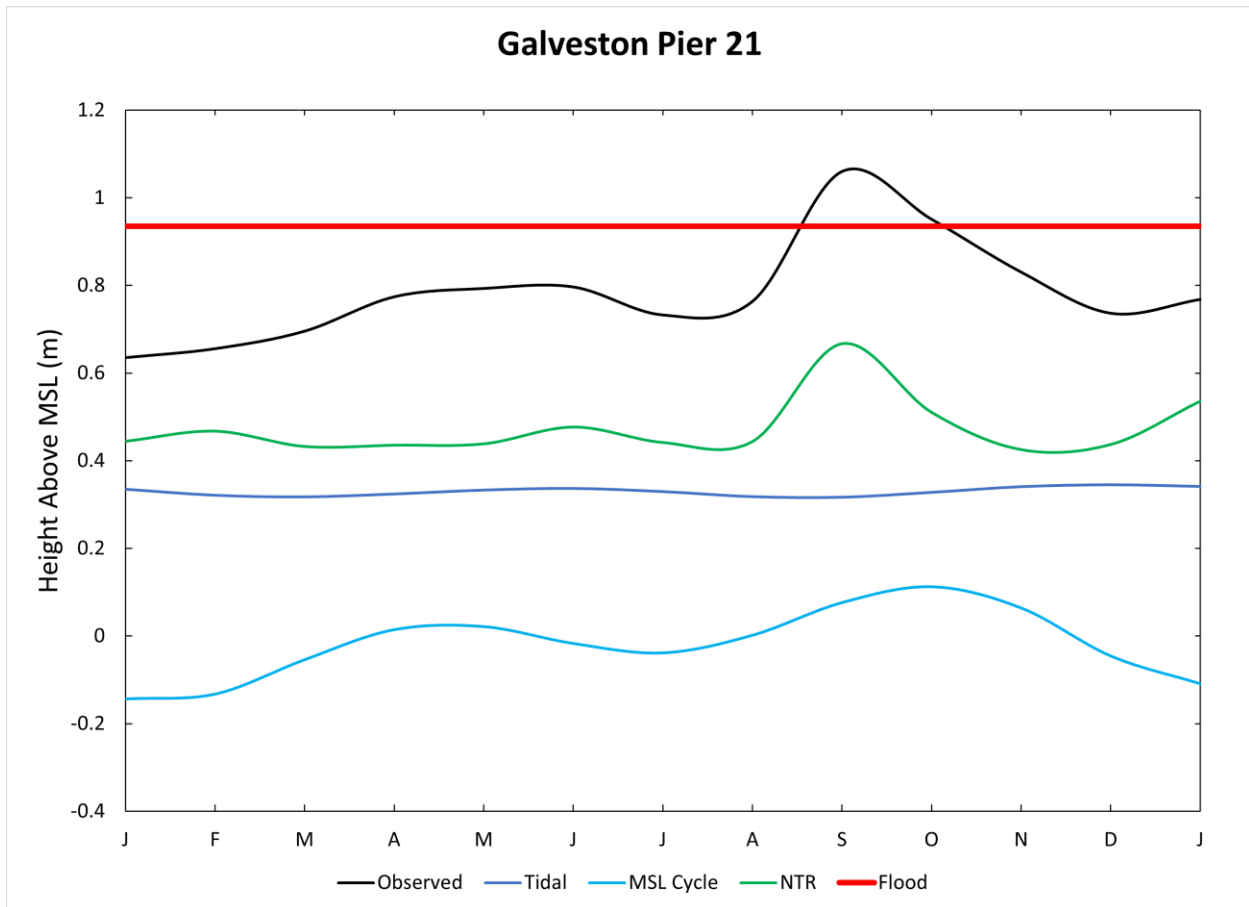
Figure 4- 8. Maximum observed water levels (black) per calendar day from 1980 to 2019 decomposed into the seasonal MSL cycle (teal), the predicted tide without the Sa and Ssa harmonic constituents (blue) and remaining non-tidal residual (NTR; green) plotted with the minor flood threshold (red) for Galveston, TX.

October. Without the influence of the NTR peak in fall, exceedances of the flood threshold in spring are a result of the tidal components and the seasonal MSL cycle being in phase with each other during that season. This is a result of the larger tidal ranges at these locations and represents a present and future risk of HTF with RSLR with little influence from other factors such as NTR.
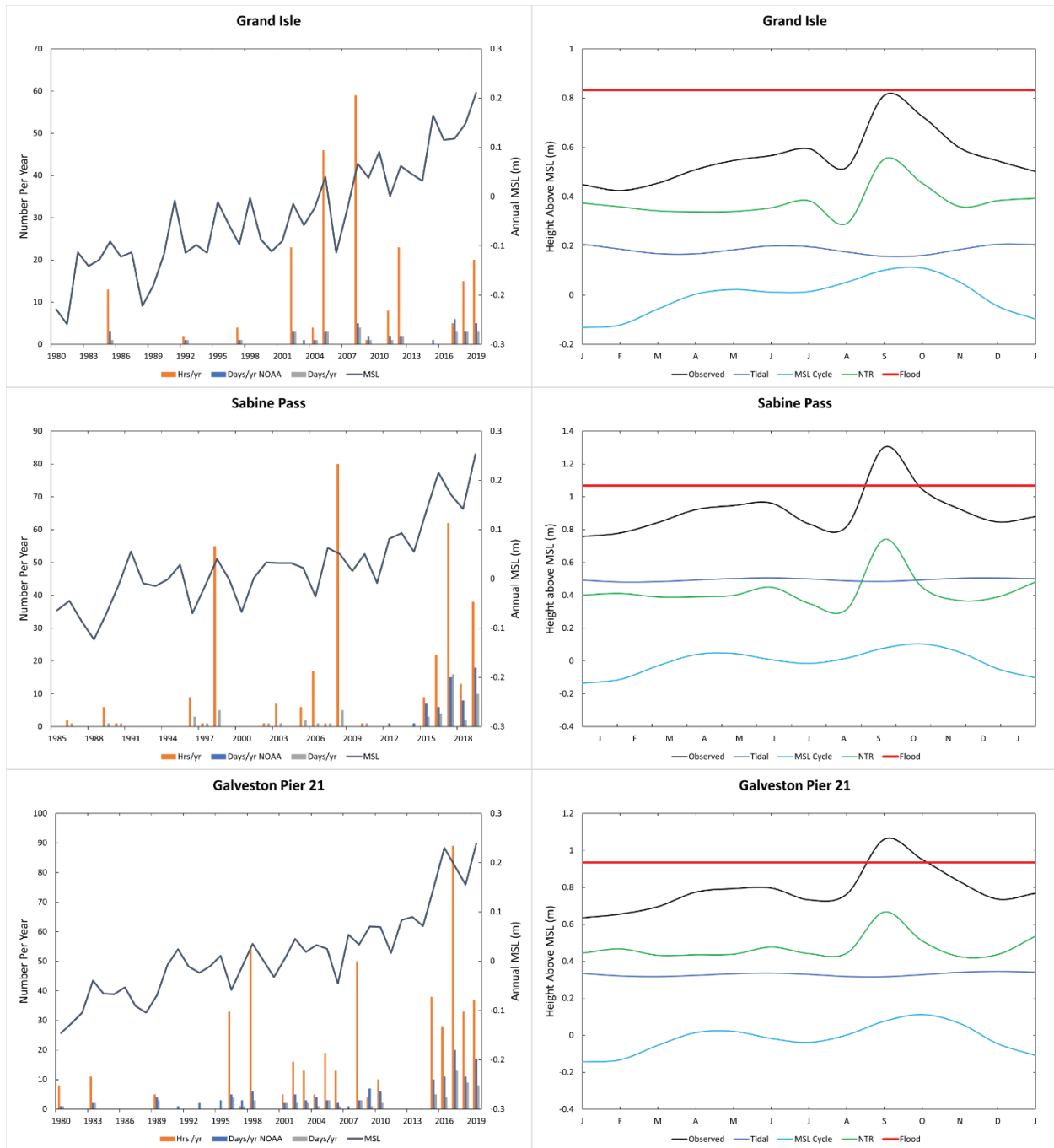
Figure 4- 9. Hourly and daily high tide flooding (left panels) and maximum observed water levels (black) per calendar day from 1980 to 2019 decomposed into the seasonal MSL cycle (teal), the predicted tide without the Sa and Ssa harmonic constituents (blue) and remaining non-tidal residual (NTR; green) plotted with the minor flood threshold (red; right panels) for Grand Isle, Sabine Pass, and Galveston.
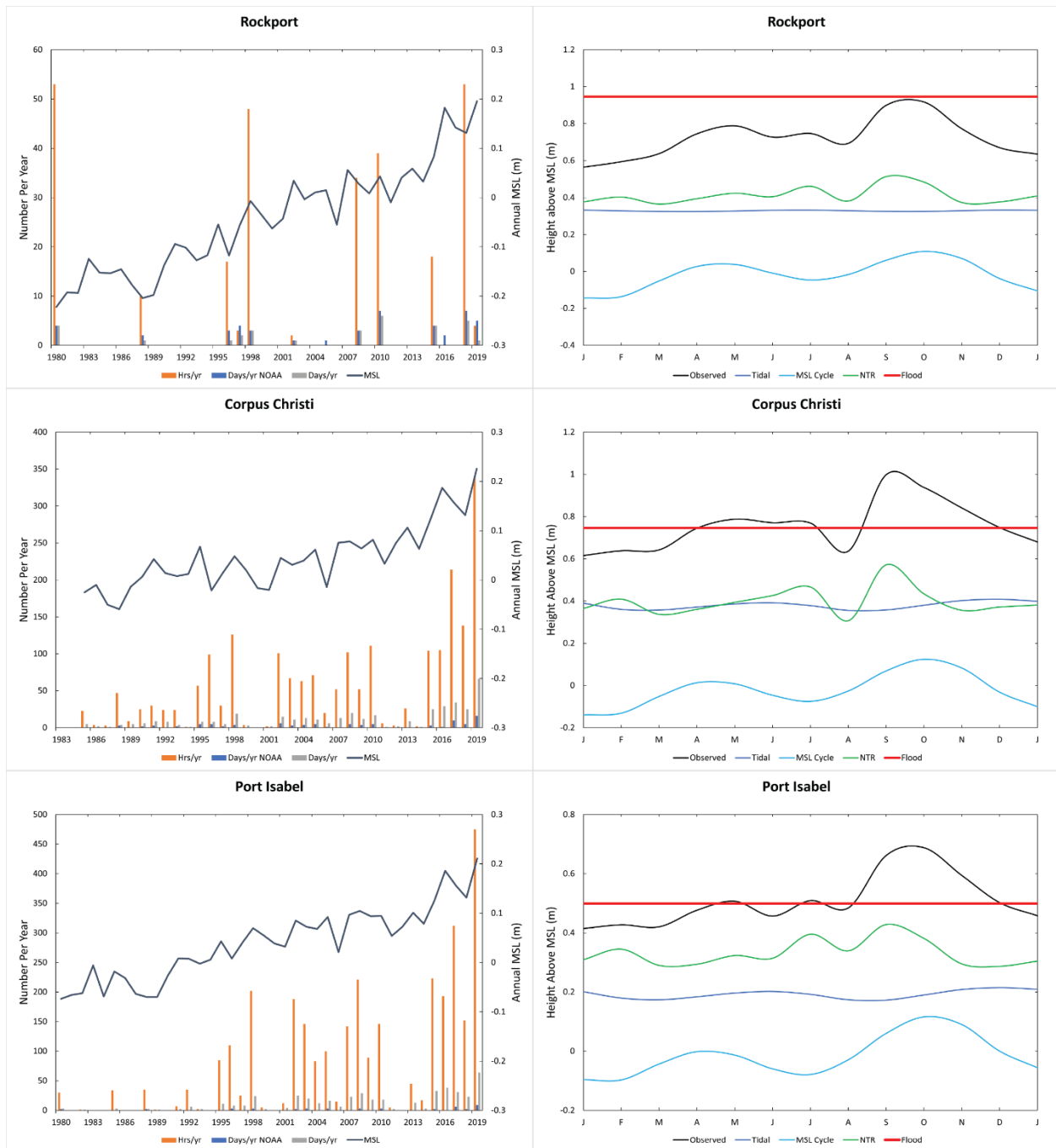
Figure 4- 10. Hourly and daily high tide flooding (left panels) and maximum observed water levels (black) per calendar day from 1980 to 2019 decomposed into the seasonal MSL cycle (teal), the predicted tide without the Sa and Ssa harmonic constituents (blue) and remaining non-tidal residual (NTR; green) plotted with the minor flood threshold (red; right panels) for Rockport, Corpus Christi, and Port Isabel.

The perigean spring tide's influence on HTF is minimal at locations on the GOM compared to other U.S. coastal locations due to their relatively small tidal ranges. No significantly higher tides were observed in the hourly tide gauge records corresponding to perigean spring tides.

4.4.3 Tropical Cyclones and Storm Surge

In this section, tropical cyclone activity and associated storm surge frequency and magnitude is examined for trends that may lead to greater risk of exceeding flood thresholds. Note that the NTR component is driven by swells and surges from storms and is thus highest during hurricane season.

Linear regression of the tropical cyclone data (Figure 4-11) suggests an increase in total tropical storms, hurricanes, and major hurricanes over the historic time-period and moving averages reveal a possible multidecadal trend. The increase observed in linear regression may be an artifact of inadequate data from early in the record as coefficients of determination (R^2) are less than 0.3 for all three categories. A relatively active period is observed beginning in the 1930s and ending in the late 1960s followed by a relatively inactive period from the 1970s to mid-1990s. Since then, the most active period has been observed with 2020 being the most active tropical cyclone season on record. Similar multidecadal trends in landfalls, seen in Figure 4-12 are also observed suggesting that for any given hurricane season, landfalls can be considered proportional to total storms in the basin.
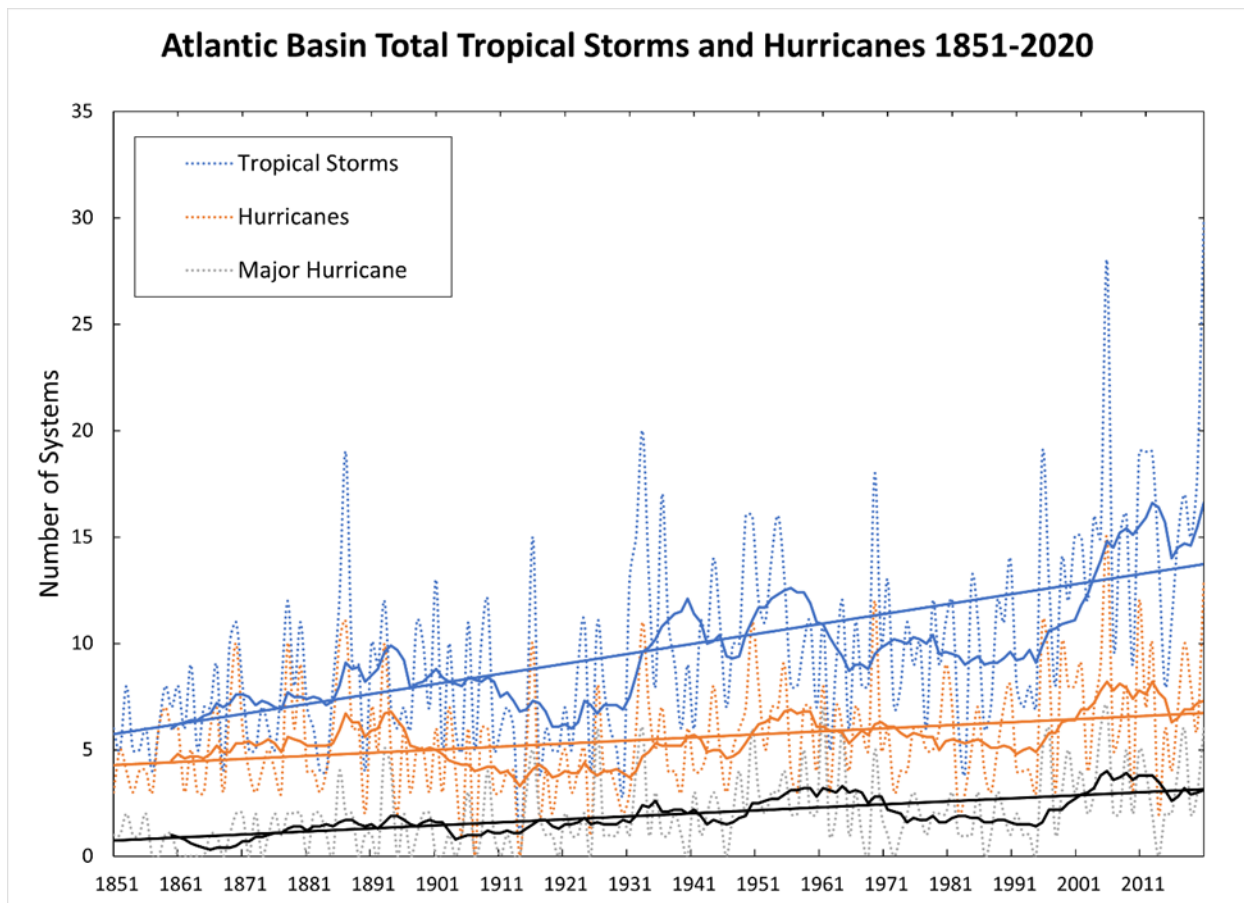
Figure 4- 11. Total tropical storms (blue), hurricanes (orange), and major hurricanes (gray) of the Atlantic basin from 1850-present (HURDAT with updates to 2020). Solid curves are the 10-year moving averages and solid lines are linear trends.
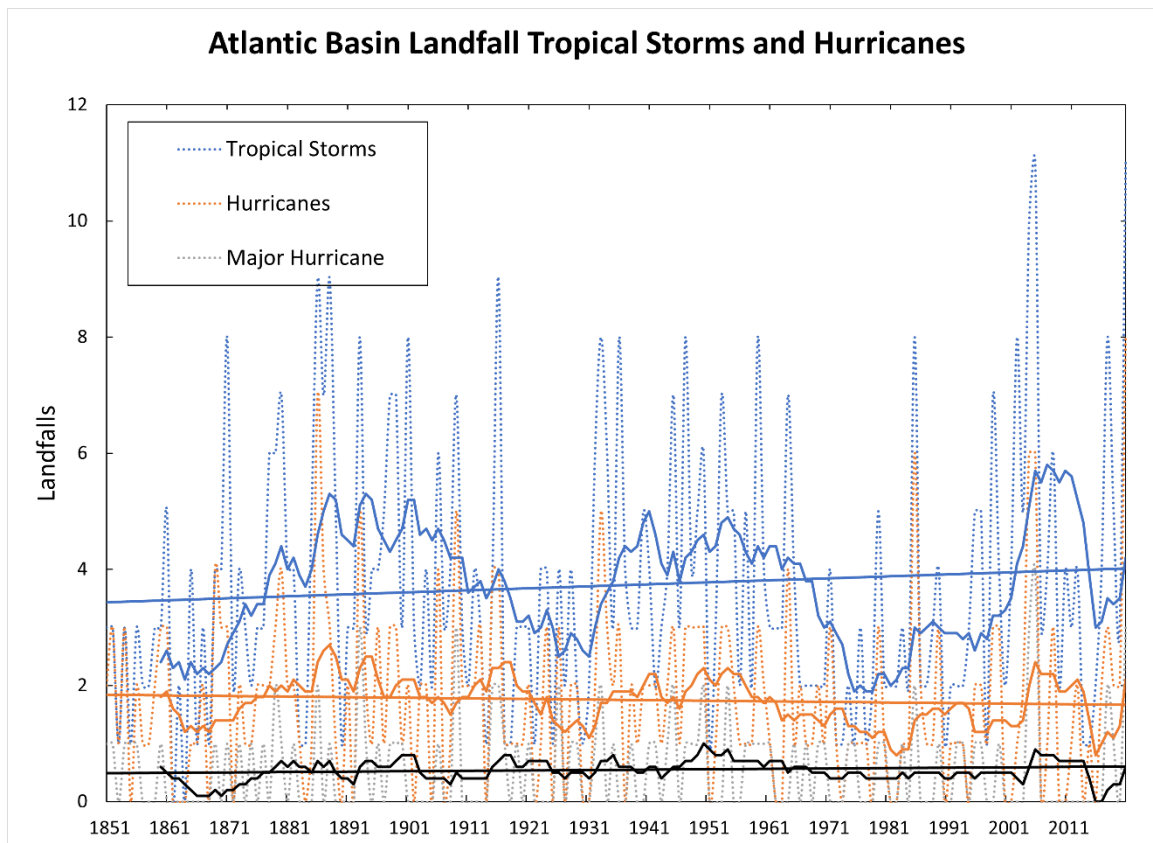
Figure 4- 12. Total landfalling tropical storms (blue), hurricanes (orange), and major hurricanes (gray) of the Atlantic basin from 1850-present (HURDAT with updates to 2020). Solid curves are the 10-year moving averages and solid lines are linear trends.

To investigate the risk associated with major hurricane landfalls in Texas and Louisiana, the 10-year ratio of major hurricanes to total hurricanes (Figure 4-13) from 1860-2020 was calculated and plotted with total annual hurricane landfalls. A lower proportion of hurricanes that made landfall in Texas and Louisiana attained category 3 or higher during the relatively active period in the Atlantic basin between the 1930s and the 1960s. In comparison, a higher proportion of landfalling hurricanes attained major hurricane status from the 1960s to the 1980s. This high proportion is because many individual years during that time saw only one hurricane make landfall and those were major hurricanes. From 1990-2020, Atlantic basin tropical cyclone activity increased as seen in Figure 4-11 while the proportion of major hurricane landfalls in Texas and Louisiana returned to levels similar to pre-1930s, a period of relatively low Atlantic basin activity. This is of interest because historically, relatively high Atlantic basin activity (i.e.,1930s-1960s) is associated with a lower ratio and the opposite is true for low activity (i.e., 1960s-1980s). This indicates that the modern active period (1990s-present) has produced more landfalling major hurricanes in Texas and Louisiana in proportion to total hurricanes compared to previous active periods.
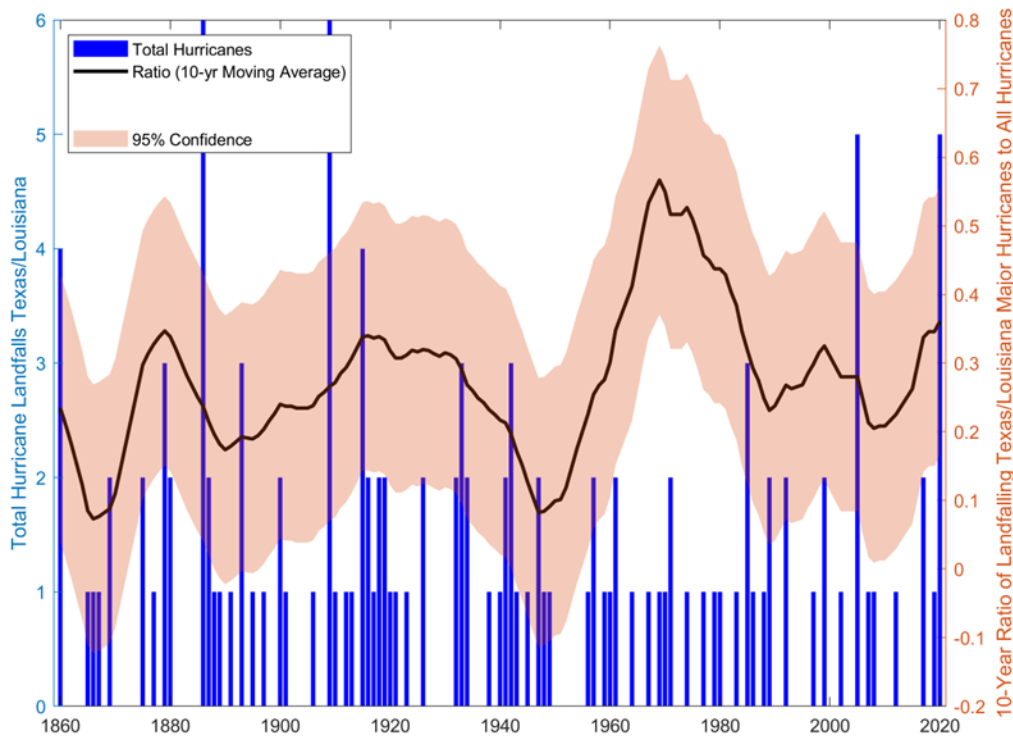
Figure 4- 13. Total landfalling hurricanes (blue) of Texas and Louisiana from 1860-2020 (HURDAT with updates to 2020) and the 10-year ratio (black) and 95% confidence interval of major hurricanes to total hurricanes smoothed with a 10-year moving average.

Table 4-5. Results of the Mann-Kendall trend test for tropical cyclone frequency.

	Increasing Trend?	P-value
Atlantic Tropical Storms	Yes	2.62×10^{-12}
Atlantic Hurricanes (Cat 1-2)	Yes	6.35×10^{-4}
Atlantic Major Hurricanes (Cat 3-4)	Yes	4.57×10^{-8}
Atlantic Tropical Storm Landfalls	No	0.618
Atlantic Hurricane Landfalls	No	0.249
Atlantic Major Hurricane Landfalls	No	0.917
TX/LA Tropical Storm Landfalls	No	0.876
TX/LA Hurricane Landfalls	No	0.507
TX/LA Major Hurricane Landfalls	No	0.895

Results of the Mann-Kendall trend test (Table 4-5) indicate that an increasing trend exists (P-value <0.05) in the Atlantic basin frequency of tropical storms, hurricanes, and major hurricanes over the past 120 years. The test could not reject the null hypothesis of no trend for all landfalling categories, suggesting that Atlantic basin tropical cyclone frequency increases may not dictate an increasing trend in landfalls to a statistically significant degree.
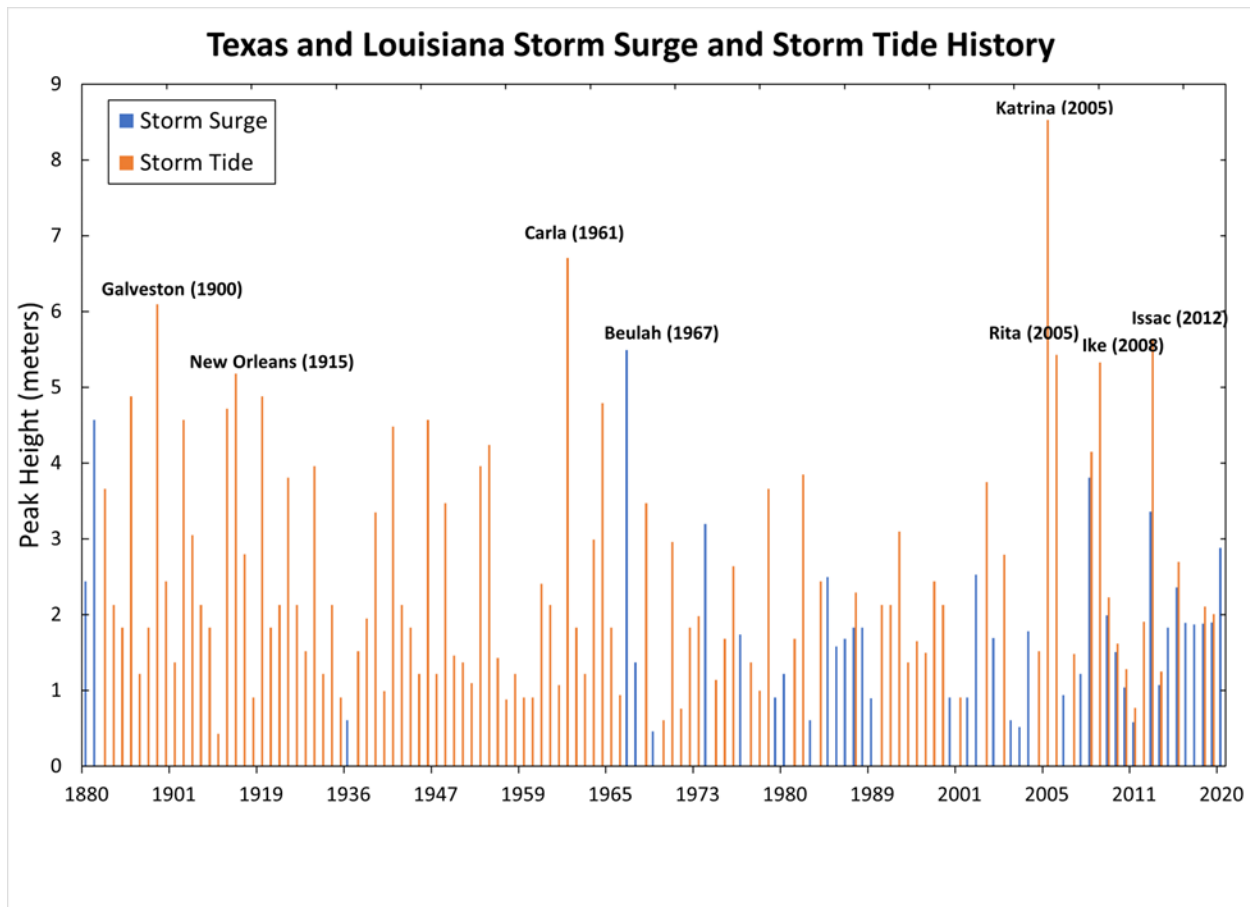
Figure 4- 14. Peak storm surge (blue) and storm tide (orange) height history of Texas and Louisiana (SURGEDAT 1880-2011 with updates to 2020).

The peak surge history of landfalling tropical cyclones in Texas and Louisiana seen in Figure 4-14 suggest that half of the highest measured storm surges/tides have occurred since 2005 with Hurricane Katrina, making landfall as a category 3 hurricane, being the maximum observed in the record. Note, that significant uncertainties in the surge estimates may exist for the Galveston 1900 category 4 hurricane and New Orleans 1915 category 3 hurricane due to a lack of verified data. Hurricane Carla was the strongest tropical cyclone to make landfall in Texas and the last category 4 hurricane to do so on record. More recent storms that made landfall in the GOM are Hurricane Rita (a major category 3 hurricane), Hurricane Ike (a category 2 hurricane), and Hurricane Issac (a category 1 hurricane). Note that even category 1 hurricanes can produce extreme water levels.

4.4.4 Effect of Climate Variations on Risk of Exceeding Floods
In this section, climate variations and associated storm surge frequency and their risk of exceeding flood thresholds are discussed. Tropical cyclones in the GOM and associated surge activity in the GOM are affected by climate variations in both the Atlantic and Pacific Ocean. On the decadal scale, phases of positive Atlantic multidecadal oscillation (AMO) are correlated with active hurricane seasons with higher numbers of major hurricanes, while cool phases have the opposite effect (Goldenberg et al., 2001) and the same correlation applies for positive phases of the Pacific decadal oscillation (Chan and Shi, 1996). Particularly, the AMO influences tropical

76

cyclone development in the main development region of the North Atlantic and Caribbean Sea from 10°N to 20°N (Goldenberg and Shapiro, 1996). It is within this region that most easterly waves propagating from the African coast contribute to tropical cyclone formation which account for 85% of Atlantic basin major hurricanes (Landsea, 1993). The results for the AMO are listed in Table 4-6 and the trend is visualized for trend qualification in Figure 4-15 showing the AMO index timeseries along with the 10-year moving averages of the Atlantic tropical cyclone analysis (from Figure 4-11). While the AMO phase influences Atlantic basin storm frequency and intensity, there is no obvious correlation between landfall of tropical storms in Texas and Louisiana and the AMO index.

Table 4-6. Atlantic basin tropical cyclone occurrence and Texas and Louisiana (TX/LA) landfalling storms in relation to the Atlantic Multidecadal Oscillation (AMO) index. Major hurricanes defined as Saffir-Simpson category 3 or above.

AMO Phase	Total Storms Atlantic	Hurricanes Atlantic	Major Hurricanes Atlantic	Total Landfalls TX/LA	Hurricane Landfalls TX/LA	Major Hurricane Landfalls TX/LA
1900-1925 AMO Cold	7.4	4.0	1.3	1.5	1.1	0.3
1926-1962 AMO Warm	10.9	5.8	2.6	1.6	0.8	0.2
1963-1994 AMO Cold	9.8	5.5	1.8	1.1	0.6	0.3
1995-2020 AMO Warm	26.8	13.3	6.1	2.9	1.3	0.4

Results from the Spearman correlation test (Table 4-7; Figure 4-16) indicate little correlation between the AMO and observed peak storm surge. However, a positive correlation (P-value <0.05) is confirmed between the AMO and Atlantic basin occurrences for tropical storms, hurricanes, and major hurricanes. As a result, one can expect increasing AMO values to correspond with increases in Atlantic tropical cyclone activity. Note, that the AMO is influenced by anthropogenic radiative forcing from GHGs and aerosols, as suggested by Mann et al. (2021). An increase in GHGs and decrease in anthropogenic aerosols may lead to consistently warm SSTs in the area of greatest hurricane formation over the Atlantic and thus favors a more positive AMO index.

Table 4-7. Spearman test results for correlation of AMO with peak surge and tropical cyclone frequency.

	Spearman R	P-value
AMO and Peak Surge	0.1279	0.162
AMO and Atlantic Tropical Storms	0.5579	2.98×10^{-11}
AMO and Atlantic Hurricanes (Cat 1-2)	0.4244	1.23×10^{-6}
AMO and Atlantic Major Hurricanes (Cat 3-4)	0.5079	2.74×10^{-9}
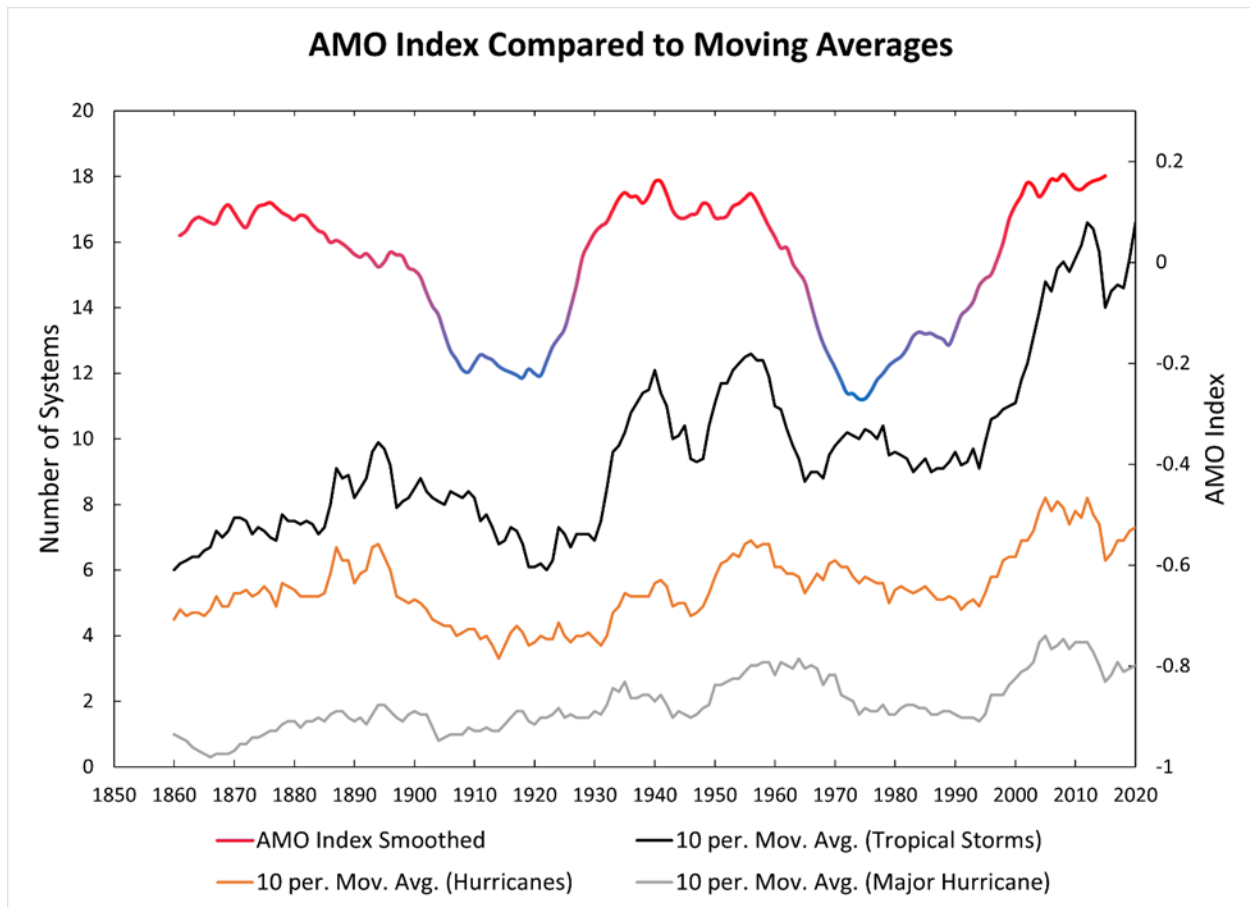
Figure 4- 15. The AMO index (red: warm phase, blue: cold phase) plotted with the 10-year moving averages of tropical storms (black), hurricanes (orange), and major hurricanes (gray) of the Atlantic basin from 1851-2020.

Correlation between the phases of the MEI index and hurricane frequency (Table 4-8) shows a suppression of Atlantic basin tropical cyclone activity and intensity during warm ENSO phases (El Niño) compared to neutral and cold (La Niña) phases (see also Gray, 1984; Bove et al., 1998; Pielke and Landsea, 1999; Elsner et al., 2001). Additionally, there is a higher number of tropical storms, hurricanes, and major hurricanes during cold phases compared to neutral phases. This confirms ENSO's teleconnection to the Atlantic basin hurricane seasonality, but results do not indicate a significant correlation between ENSO and landfalling storms in Texas and Louisiana.
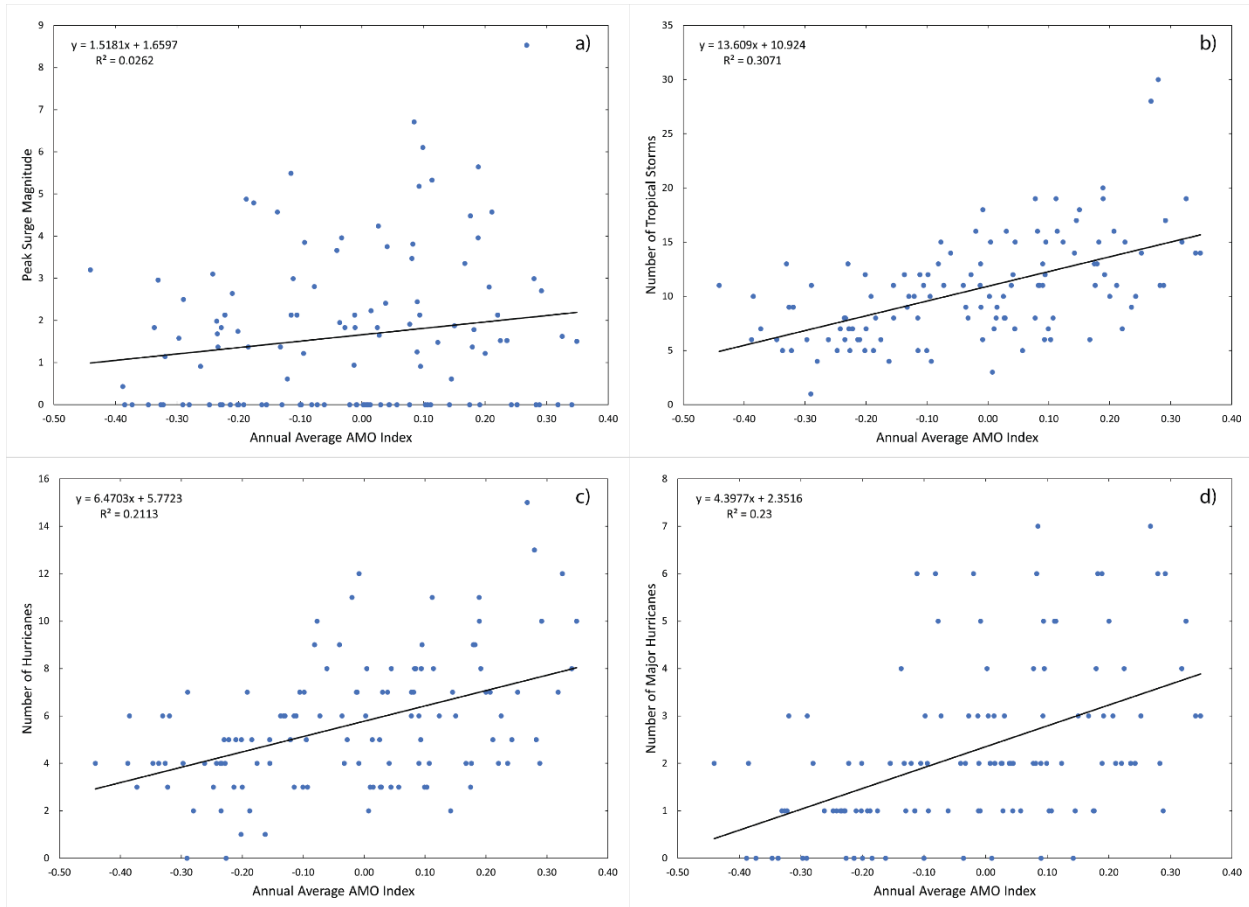
Figure 4- 16. Correlation scatterplots for the annual average AMO index with (a) peak surge values, (b) number of tropical storms, (c) number of hurricanes, and (d) major hurricanes. Corresponding R values are listed in Table 4-7.

Table 4-8. Atlantic basin tropical cyclone occurrence and Texas and Louisiana (TX/LA) landfalling storms in relation to the Multivariant ENSO Index (MEI). Major hurricanes defined as Saffir-Simpson category 3 or above.

MEI Phase	Total Storms Atlantic	Hurricanes Atlantic	Major Hurricanes Atlantic	Total Landfalls TX/LA	Hurricane Landfalls TX/LA	Major Hurricane Landfalls TX/LA
Cold	16.1	8.2	3.9	1.7	0.9	0.3
Neutral	13.0	7.1	2.6	1.4	0.8	0.3
Warm	8.1	3.4	1.1	1.2	0.3	0.0

4.4.5 Return Periods

Return periods based on historic data are commonly used to assess risk and inform design ranges, but recent and future changes to observed historic trends are not accounted for. In this section, historic peak surge return periods for Texas and Louisiana are estimated for 1900-2020 and adjusted for observed percent changes in surge frequency and magnitude to estimate new return periods for use in assessing future risk. Peak surge magnitude and return periods are presented in Figure 4-17 with resulting return periods summarized in Table 4-9. The results are

79

similar to those estimated for the entire Gulf of Mexico (Table 4-3) with slightly lower magnitude surge height estimates corresponding to the 100-yr, 50-yr, 25-yr, and 10-yr periods.

Figure 4- 17. Logarithmic plot of peak storm surge magnitude and return periods for Texas and Louisiana estimated using updated SURGEDAT data from 1900-2020.

Table 4-9. Texas and Louisiana Peak Surge Return Periods.

Return Period (years)	Surge Height (meters)
10	4.37
25	5.79
50	6.86
75	7.48
100	7.93
500	10.42

Averages taken over 30-yr periods from 1900 to 2020 are summarized in Table 4-10 and reveal average annual frequency of peak surge events has increased 40% and magnitude of peak surge increased by ~12% relative to the 1930-1960 baseline.

Table 4-10. 30-Year Averages for Frequency and Magnitude of Peak Surge.

Time Period	Average Frequency	Average Magnitude (m)
1900-1930	0.57	2.96
1930-1960	1.00	2.01
1960-1990	1.27	2.14
1990-2020	1.40	2.14

Accounting for percent changes from the baseline period, Figure 4-18 displays the adjusted return periods for peak surge events in Texas and Louisiana. Results summarized in Table 4-11 reveal an increase of ~2.1 to 2.8m of peak surge magnitudes corresponding to the standard return periods.
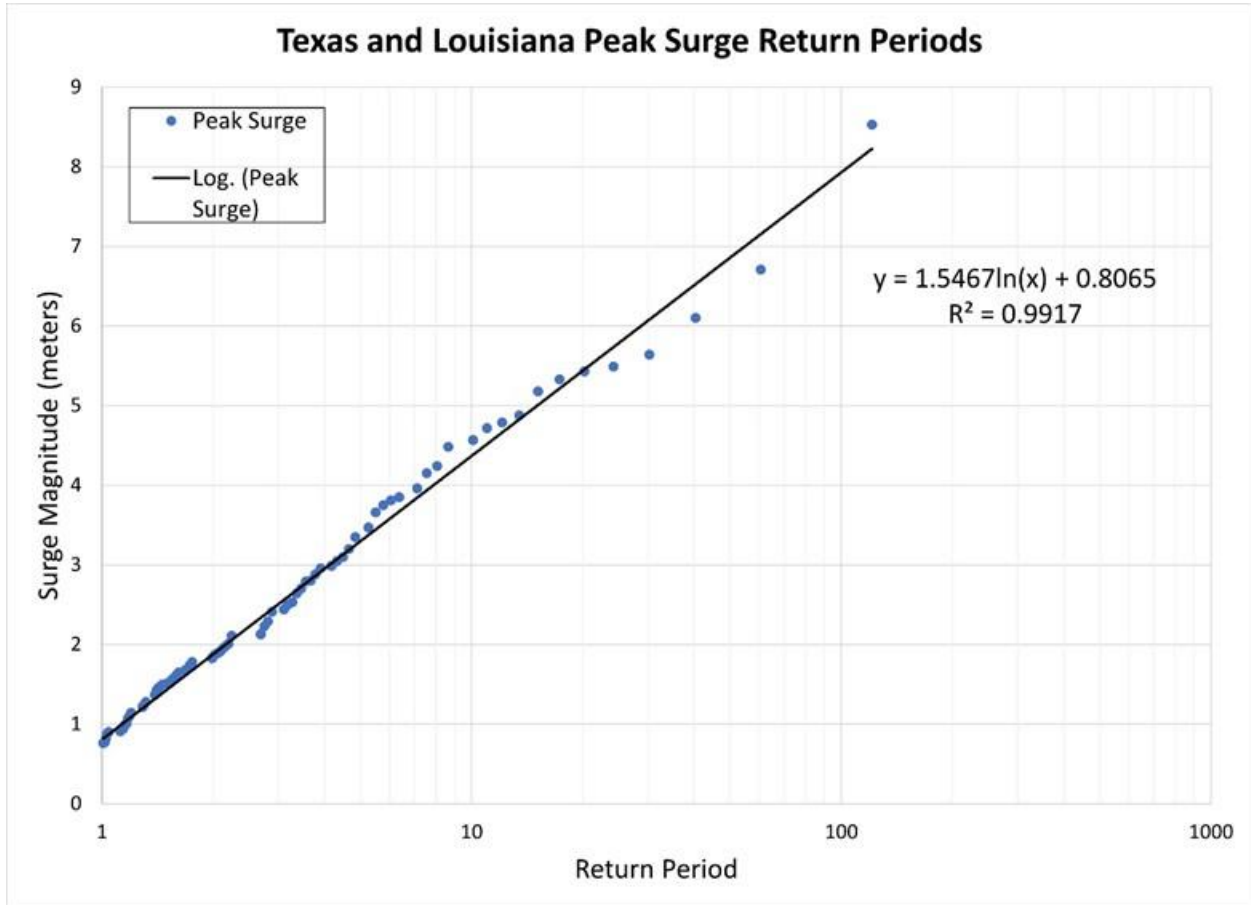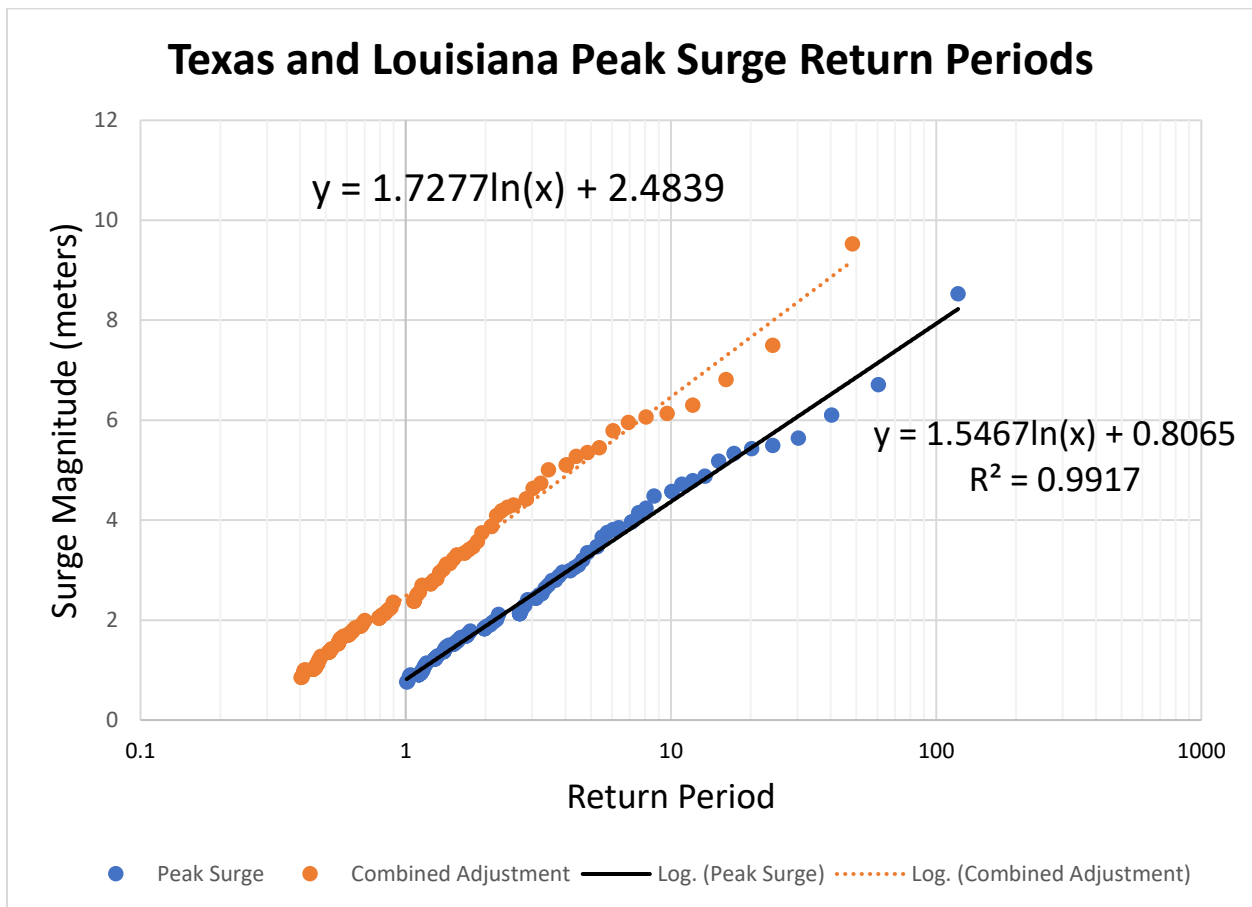

Figure 4- 18. Logarithmic plot of peak storm surge magnitude and return periods for Texas and Louisiana estimated using updated SURGEDAT data from 1900-2020 (blue) and estimated future return periods (orange) based on percent changes in 30-year averages of frequency and magnitude between 1930-1960 and 1990-2020.

Table 4-11. Return periods adjusted for percent change in frequency and magnitude from 1930-1960 to 1990-2020 30-year averages.

Return Period (years)	Calculated Surge Height (meters)	Historical Surge Height (meters)
10	6.46	4.37
25	8.05	5.79
50	9.24	6.86
75	9.94	7.48
100	10.44	7.93
500	13.22	10.42

Calculating the THI for each location over 40-year time periods from 1901 to 2020 allows for investigation of how, and if, tropical cyclone activity at these locations has changed over the past 120 years. Results, summarized in Table 4-12, reveal interesting spaciotemporal patterns in tropical cyclone activity when examining the total THI by location and return period. Locations in South Texas such as Port Isabel, Corpus Christi, and Rockport have THIs below 100 from 1901-1940 and 1981-2020 but have THIs above 100 from 1941-1980. Except for Freshwater Canal from 1941-1980, all other locations have THIs above 100 during all time periods. Matagorda City and Galveston THIs fluctuate very little over the past 120 years and locations from the eastern Texas border east into Louisiana show some changes in total THI over time. Grand Isle has the highest THI from 1901-1940 and 1981-2020 while Sabine Pass had the highest THI during 1941-1980. In general, this indicates the central and eastern portions of the study area (Sabine Pass east to Grand Isle) have historically experienced the greatest hazards from tropical cyclones compared to southern Texas.

Table 4-12. THI by location and return period. Percent contribution from tropical storms (TS), hurricanes (H), major hurricanes (MH) presented with the total (TOT) THI.

Period	1901-1940				1941-1980				1981-2020			
Category	TS	H	MH	TOT	TS	H	MH	TOT	TS	H	MH	TOT
Port Isabel	11	53	36	90	12	11	77	114	9	30	61	66
Corpus Christi	9	48	43	92	15	17	68	118	23	23	55	88
Rockport	7	34	59	82	15	15	70	104	26	21	53	76
Matagorda	9	40	51	110	14	29	57	112	16	40	44	110
Galveston	7	26	67	108	19	27	54	104	21	34	45	106
Sabine Pass	8	28	64	100	17	34	49	130	16	40	44	110
Freshwater Canal	16	25	58	110	19	38	43	94	7	38	55	116
Grand Isle	13	33	53	120	21	36	43	112	16	27	58	180

With only two exceptions during the earliest return period, major hurricanes represent the greatest percent contribution to the weighted index for all locations and times. From 1901-1940, 9 hurricanes of category 3 or higher, the most for that time, impacted Galveston. From 1941-1980, Port Isabel had the most major hurricanes with 11, and from 1981-2020, Grand Isle ranks highest with 13 major hurricanes. This does not indicate any spaciotemporal pattern within the study area of the northern GOM for major hurricane strikes, leaving great uncertainty remaining about how often or where a major hurricane will make landfall in the northern GOM.

Results of the THI are visualized in Figure 4-19 showing the contributions from tropical storms, hurricanes, and major hurricanes along with the total THI for each return period. While the peak surge return periods for the entire area (Figure 4-18) indicate an increasing risk of higher magnitude storm surges occurring more frequently overall, the THI for each location does not indicate any reliable trends or patterns in tropical cyclone activity to confirm this potential change in surge risk.
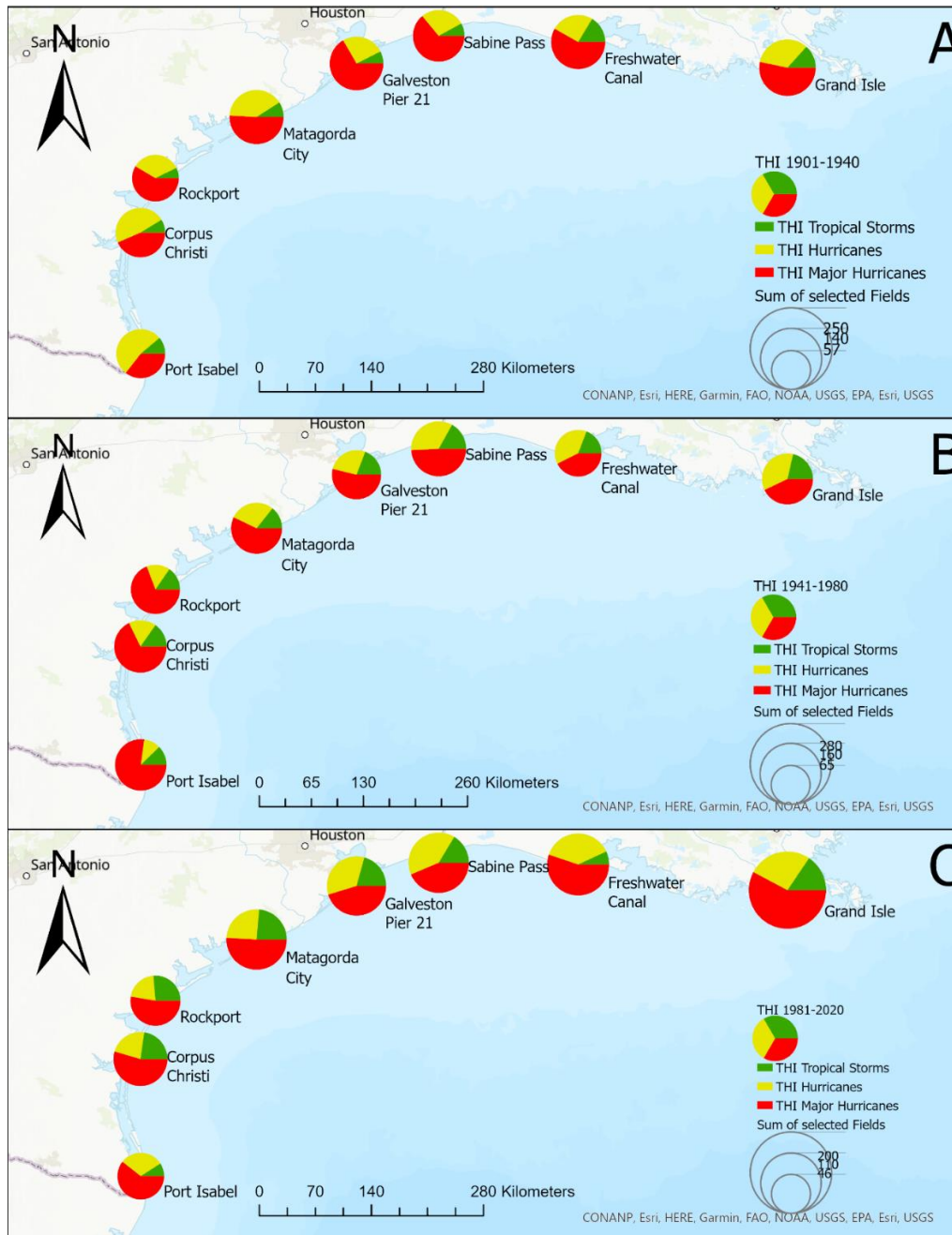

Figure 4- 19. THI by location for (a) 1901-1940, (b) 1941-1980, and (c) 1981-2020. Colors represent the weighted contributions to the total THI from tropical storms (green), hurricanes (yellow), and major hurricanes (red) while the size of the pie represents the total THI.

4.4.6 Case Study: Baton Rouge, LA area

In this section, results of the case study in southeastern Louisiana regarding storm tide risks to vulnerable populations are presented. The study area was chosen for its proximity to the two largest cities in Louisiana by population, New Orleans, and Baton Rouge. The city of New Orleans was not included due to its post-Katrina upgraded levee system. Figure 4-20 displays the study area with major roads and interstates overlaid over the map DEM. Inspection of the DEM reveals lowest elevations exist south of Interstate-12 with rapidly increasing elevation moving north of that highway. The cities of Baton Rouge and Hammond are placed in locations of relatively higher ground than Gonzalez, LaPlace, and New Orleans.
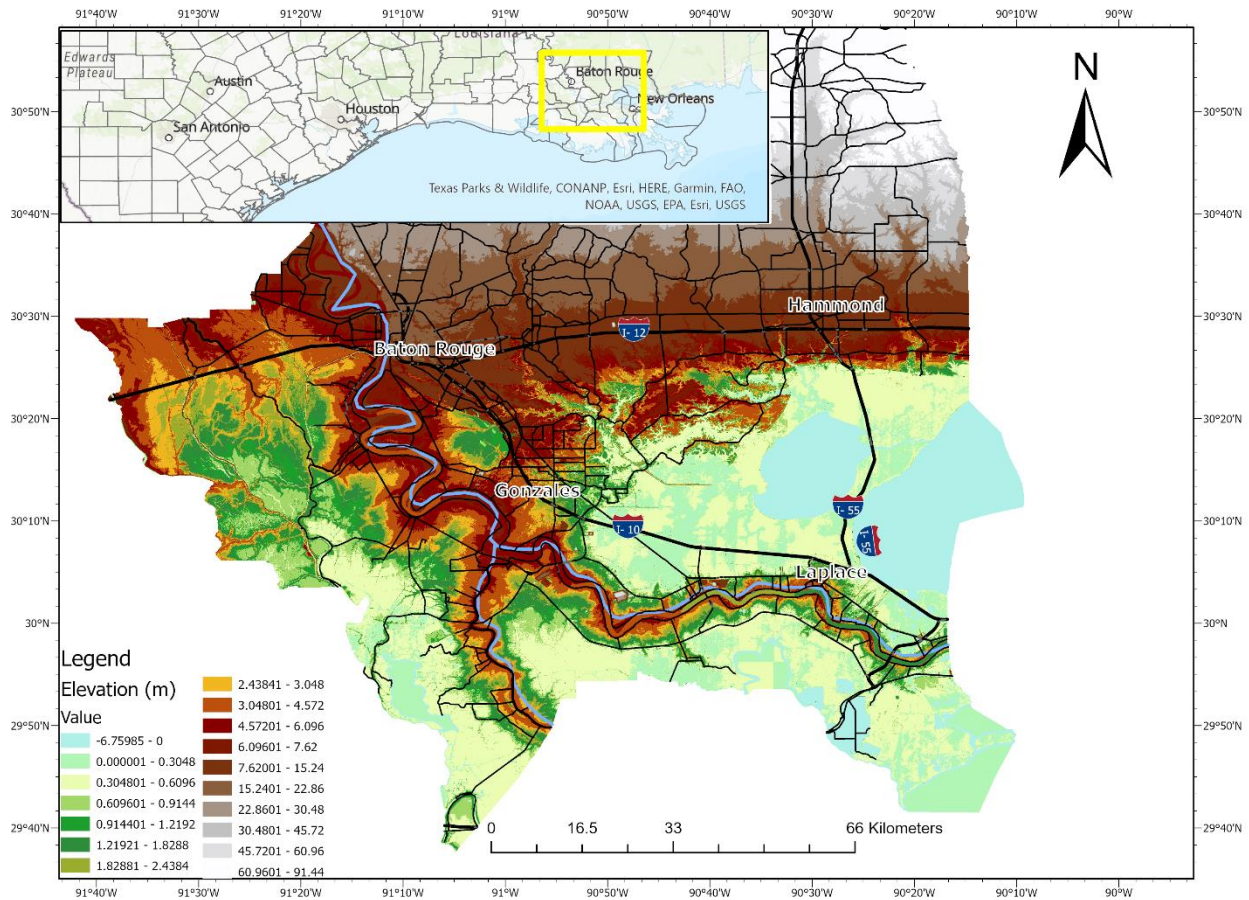
Figure 4- 20. The case study area with locations, major roads and highways overlayed over the map of the 10-meter resolution USGS digital elevation model.

Storm tide inundation maps under current sea level conditions (Figure 4-21) for category 1, 3, and 5 hurricanes reveal extensive inundation in the lower elevations of the study area. Category 1 storm tides result in possible inundation up to 12 feet (~3.6 m) and impact an estimated 380,000 people that live in the inundated area. Category 3 storm tide results in increased area and depth of inundation that affects ~630,000 people with inundation heights of up to over 15 ft (~4.6 m). While the category 5 storm tide inundation area increase from category 3 is modest due to elevation increases moving northward in the study area, the area with inundation heights of over
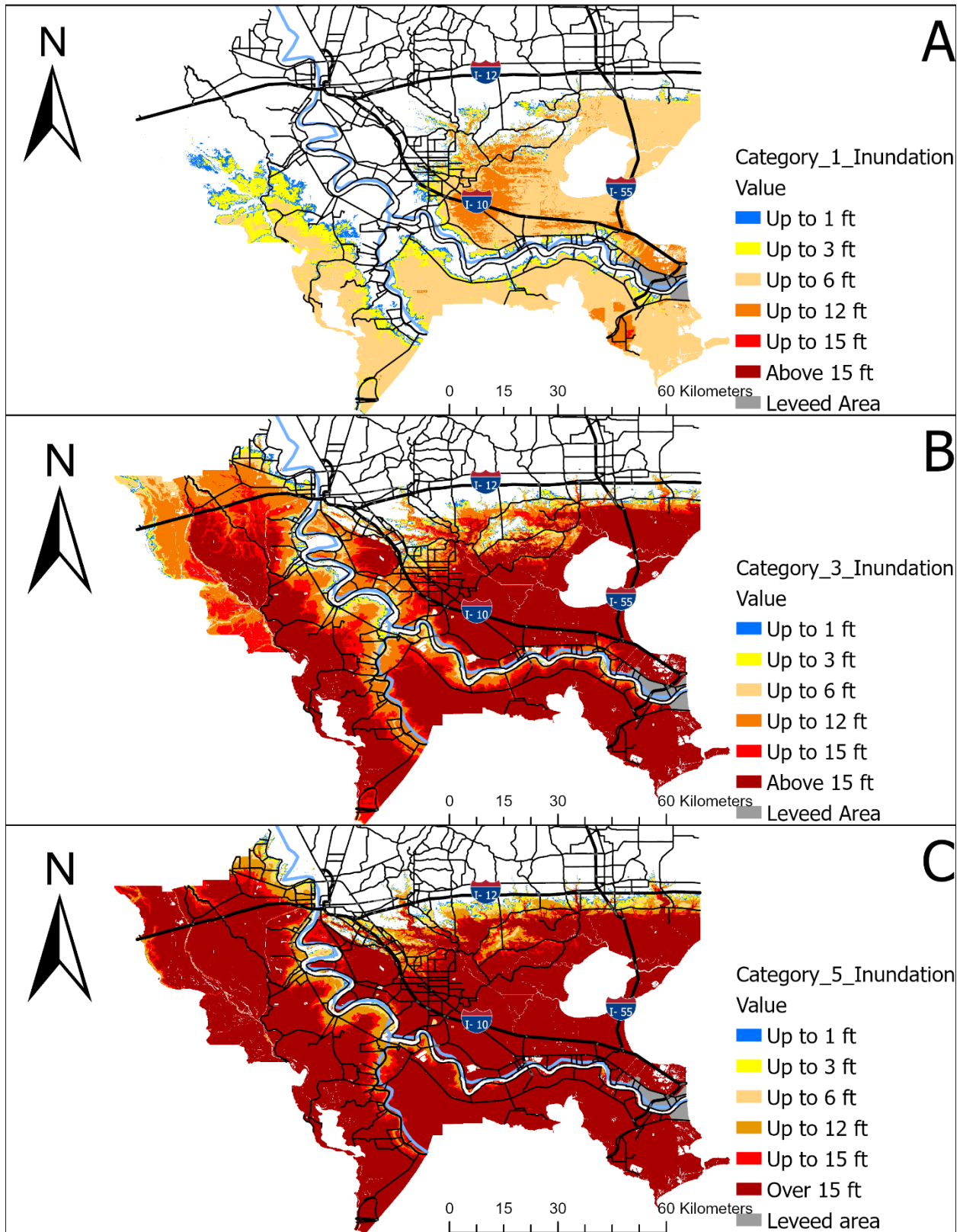
Figure 4- 21. Storm tide inundation map for (a) category 1, (b) category 3, and (c) category 5 hurricane occurring at high tide. Map layers acquired from the National Storm Surge Risk Map Version 3 (NHC).

15 ft (~4.6 m) expand to affect an additional ~40,000 people. As RSLR occurs over time, storm tides will increase in height and will affect a greater area of inundation depending on topography. The maximum area of inundation from storm tides enhanced by the extreme RSLR probabilistic scenario is mapped in Figure 4-22 depicting the areas of inundation for category 1, 3, and 5 as well as the category 5 storm tide under the extreme RSLR scenario. Under this scenario a category 5 hurricane would produce a storm tide that potentially impacts all major highways, including Interstate-12, and populations in the cities of Hammond and Baton Rouge that would not be affected under current sea level conditions. Area of inundation increases significantly between the category 1 and 3 storm tides, but a relatively modest increase in area is observed between category 3 and 5, as well as with the addition of the RSLR scenario. Therefore, the maximum area of inundation under future scenarios is restrained by the topography of the region and RSLR will result in storm tides producing higher inundation above ground in areas currently at risk of flooding and a modest increase in area affected by up to 3 ft (~1 m) inundation. Maps for the three hurricane categories with the addition of the three RSLR scenarios are shown in Figure 4-23 and total population affected by category and scenario are estimated in Figure 4-24.
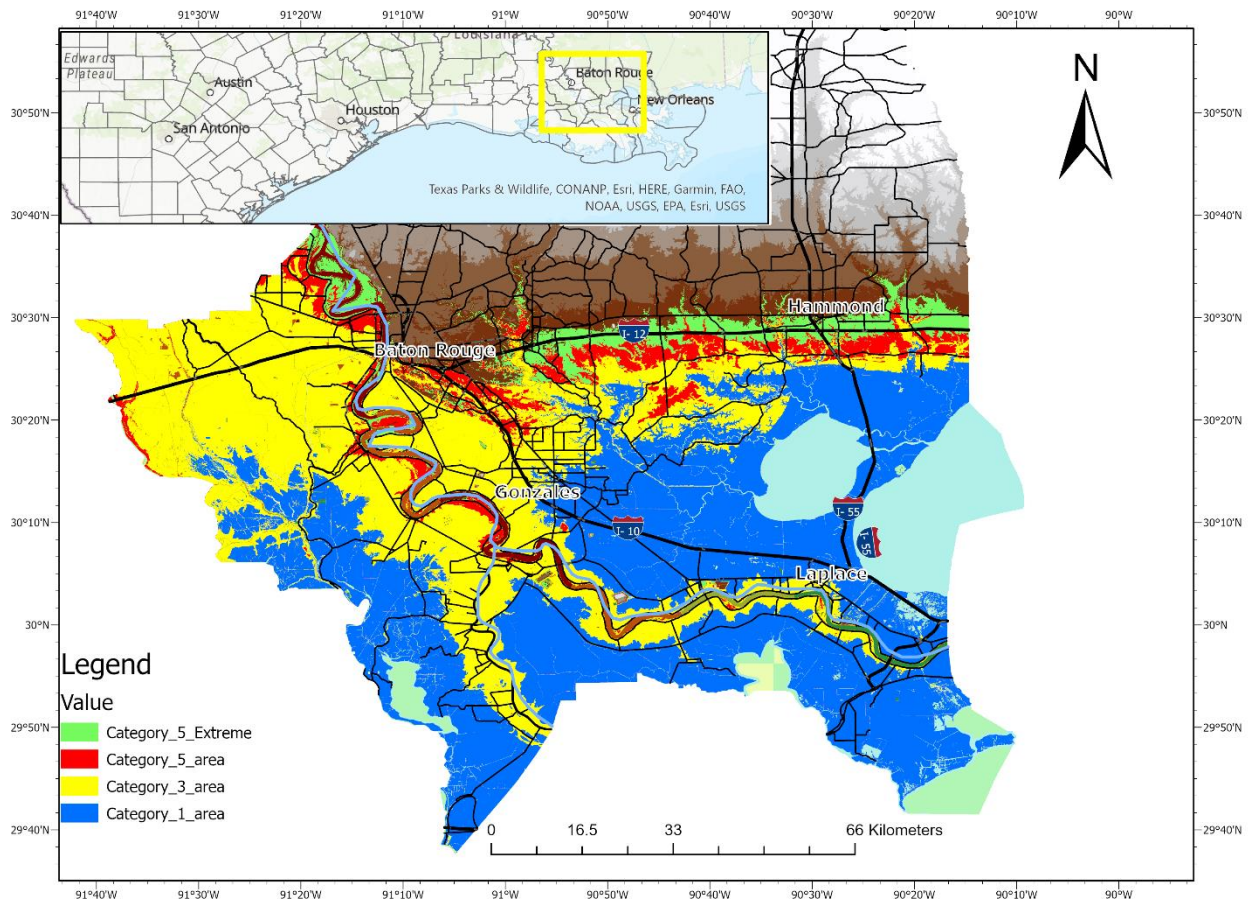
Figure 4- 22 Storm tide inundation area resulting from hurricane category 1 (blue), 3 (yellow), and 5 (red) mapped with the extreme RSLR scenario (bright green) and 10-meter resolution DEM elevation map. Due to higher elevation north of Interstate 12, inundation area increases modestly with extreme sea level rise.
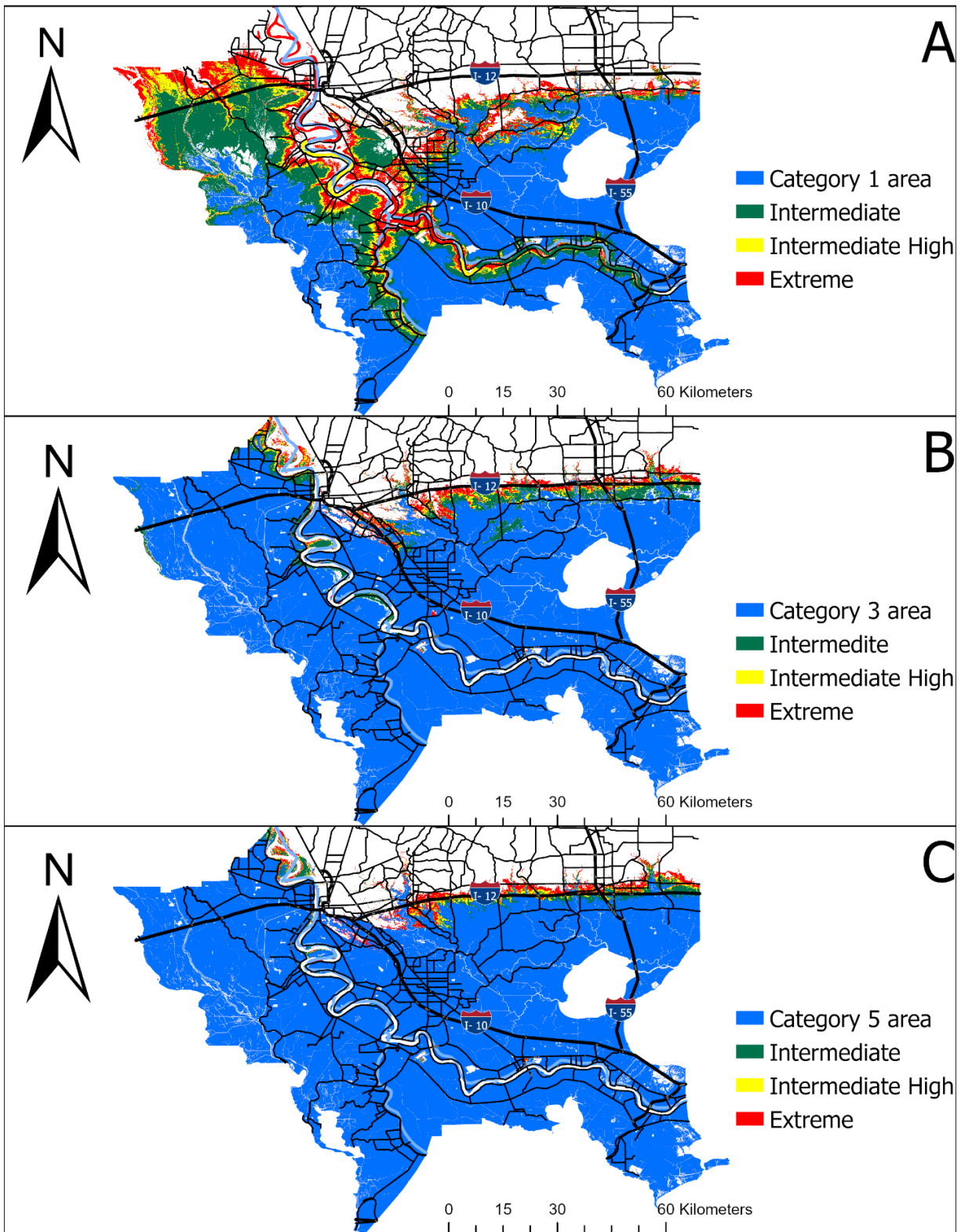
Figure 4- 23. Storm tide inundation map with RSLR projections for 2091-2100 relative to 1991-2009 for (a) category 1, (b) category 3, and (c) category 5 hurricane occurring at mean high tide (MHHW) plotted with RCP-based RSLR scenarios estimating the increase in inundation area for each scenario.

These results indicate that storm tides will impact a greater number of people under RSLR with the largest changes observed in the category 1 storm tide enhanced by RSLR. While the risk of flooding from a major hurricane remains high, these results indicate the greatest change in risk with future RSLR scenarios comes from storm tides produced by lower category storms.

Baton Rouge Area
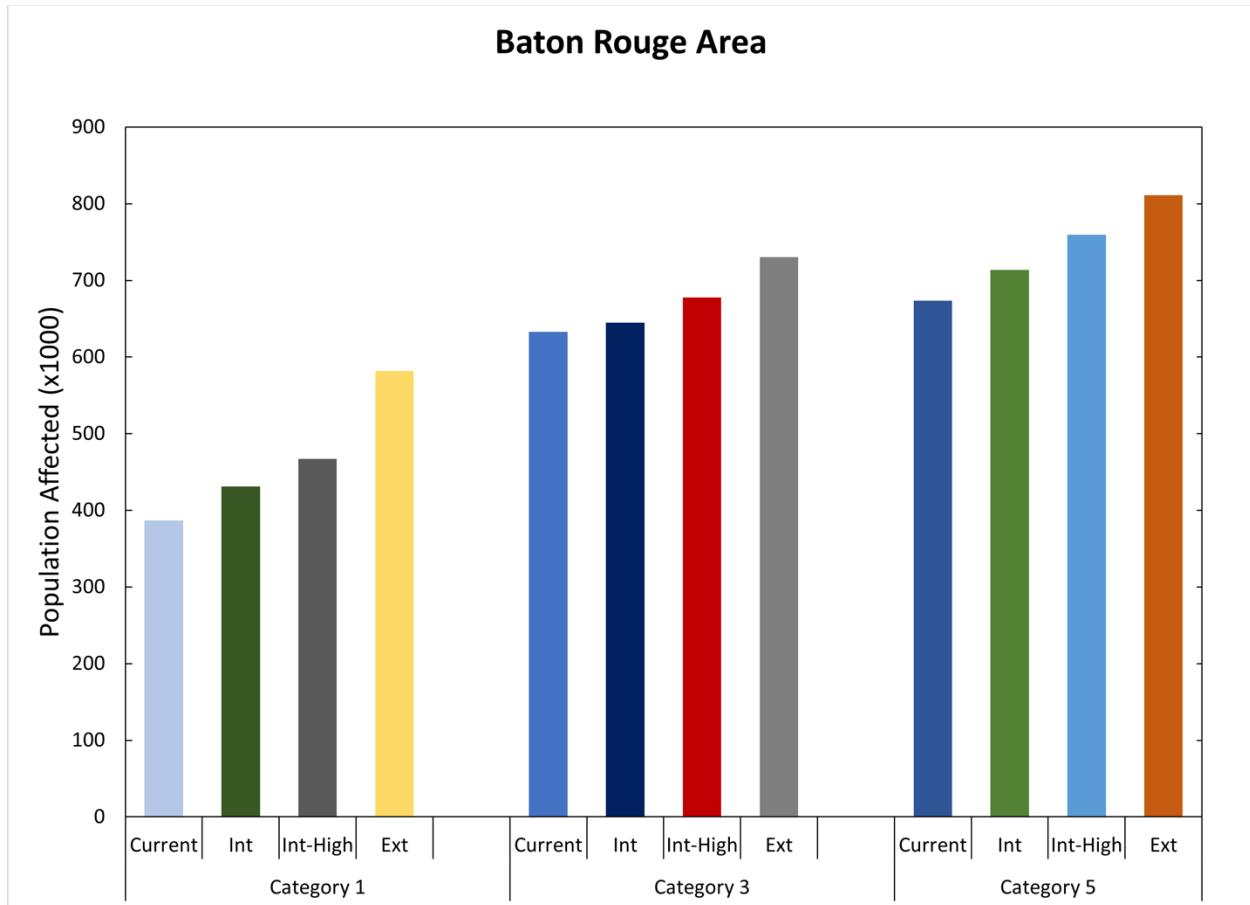
Figure 4- 24. The estimated total population affected by maximum storm tide modeled on category 1, 3, and 5 hurricanes for the case study area (current) plotted with the estimated additional population affected with RSLR scenarios intermediate (Int), intermediate-high, (Int-High), and extreme (Ext). Estimated populations based on SVI 2018 tracts.

SVI tracts have been overlaid with the maximum area of inundation of the extreme RSLR scenario for the three hurricane classes (Figure 4-25) to examine the impacts of the vulnerability and risk of populations to flooding. The three SVI tracts containing the most vulnerable populations, seen in the map as orange and red colors, are located within the city of Baton Rouge at relatively higher elevations than the remaining vulnerable tracts. Of the tracts located in lower elevations, five are in the 90th percentile for mobile homes which are at higher risk of damage from flooding than traditional homes and three of those five are in areas that, under current sea level, can potentially receive up to 12 ft (~3.6 m) of flooding from a category 1 storm tide. The remaining vulnerable tracts are in the 90th percentile for disabilities, and populations above 65 or below 17 years of age. Under the extreme RSLR scenario, category 1 hurricane storm tide affects 10 tracts
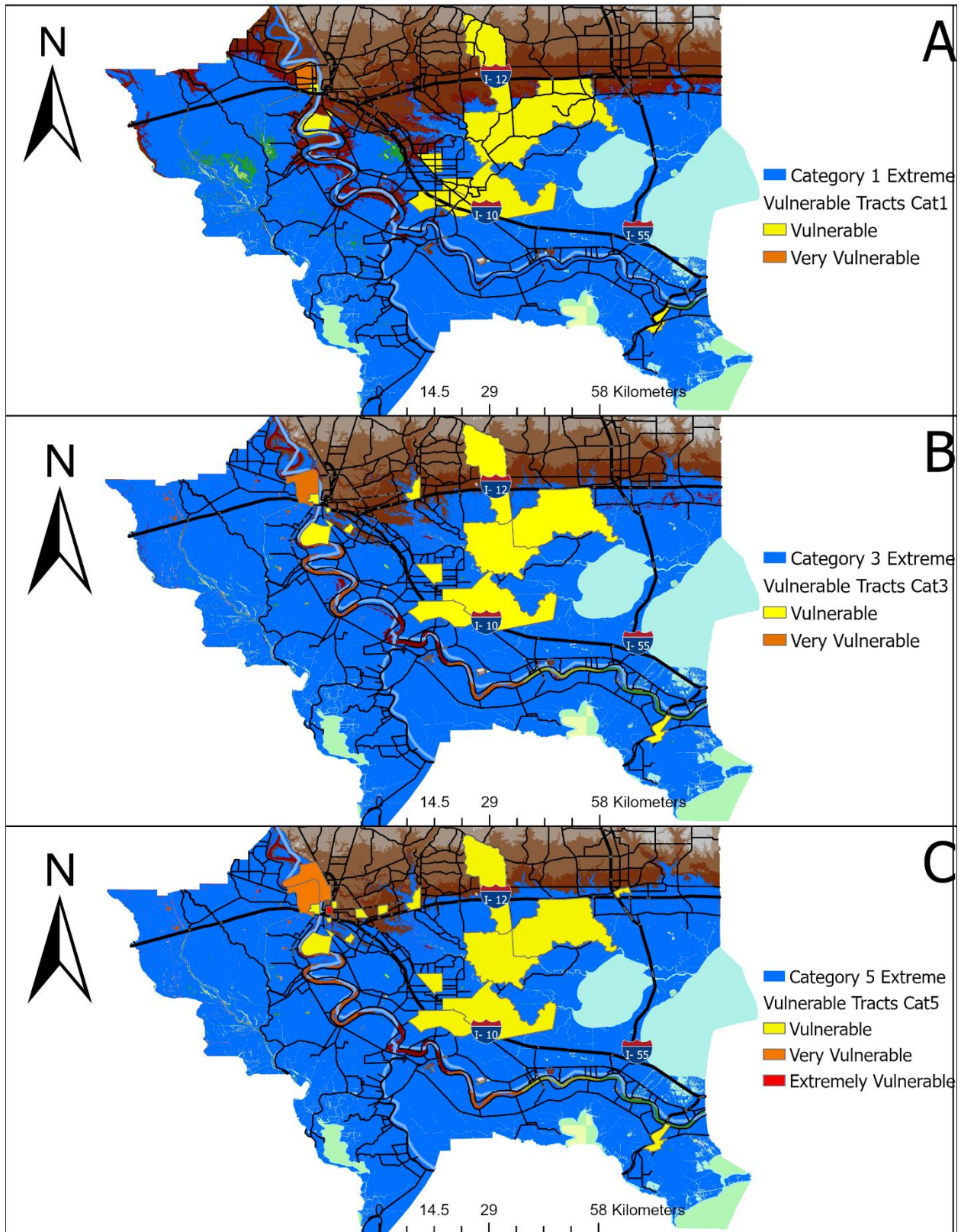
Figure 4- 25. Maps displaying vulnerable tracts based on SVI variables for (a) category 1, (b) category 3, and (c) category 5 hurricane storm tide under the extreme RSLR scenario.

classified as vulnerable, category 3 storm tide affects 13 tracts, and category 5 storm tide affects 19 tracts. Table 4-13 describes the vulnerability classifications based on SVI 2018 variables (see also section 4.3.5).

Table 4-13. Classification of vulnerability based on the 90th percentile of the Social Vulnerability Index variables of (1) below poverty, (2) age 65 or older, (3) age 17 or younger, (4) civilians with disabilities, (5) mobile homes, (6) no vehicle.

Classification	Vulnerable	Very Vulnerable	Extremely Vulnerable
Number of variables in the 90th percentile	1-3	4-5	>5

4.4.7 Case Study: Houston/Galveston, TX Area

The study area was chosen for its high population and coastal proximity as well as the location's history of flooding associated with storm tides. The study area contains two locations at Texas City and the Lake Jackson/Freeport area that were excluded from analysis due to the levees that surround them. Figure 4-26 shows the location of the study area relative to the GOM coast, landmark cities, major roads and interstates, and the DEM. Inspection of the DEM reveals
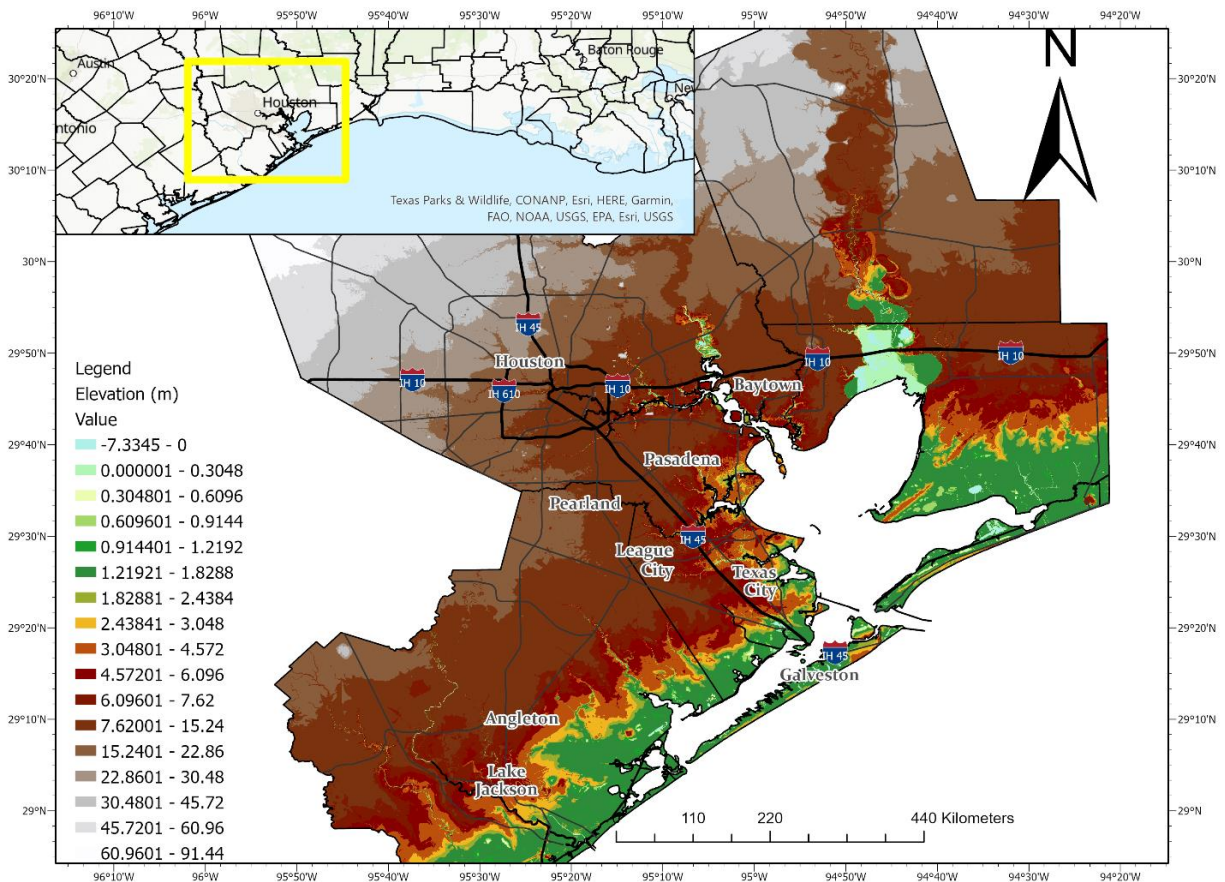
Figure 4- 26. Harris county, Texas, 10-meter resolution USGS digital elevation with major cities, Texas and interstate highways.

the lowest elevations exist directly on the coast with gradual increase in elevation moving north and west from the coast. Houston, the most populated city in Texas, sits on relatively higher ground than coastal locations such as Galveston Island but is hydrologically connected to the bay through a series of rivers and bayous.

The storm tide inundation maps under current sea level (Figure 4-27) show the relative flooding above ground for category 1, 3, and 5 hurricanes. A category 1 storm tide results in inundation up to 6 feet (~1.8 m) affecting ~380,000 people that live in the area directly on the coast while denser populations inland remain unaffected.

Category 3 storm tide results in an increased area of risk representing ~1 million residents who live along the coast as well as the more densely populated cities along the Interstate-45 corridor. The inundation depths for a category 3 storm tide are up to ~12-15 feet (~3.6-4.6 m) closest to the coast, including Galveston and ~6-12 feet (~1.8-3.6 m) in locations directly on the bay. The category 5 storm tide map reveals increased height of inundation up to over 15 feet (~4.6 m) that extends further inland to affect densely populated areas along the Interstate-45 and Interstate-10 corridors as well as the Houston metropolitan area. Storm tides of this magnitude would reverse the drainage of the streams and bayous leading to compound flooding from the intense precipitation of the hurricane. The maximum area of inundation from the three categories of storm tides and the category 5 storm tide enhanced by the extreme RSLR probabilistic scenario is mapped in Figure 4-28. The results indicate an increase in inundation area under the extreme scenario that affects areas of high population density including downtown Houston, eastern Harris County, and major highways. The estimated number of residents affected by a category 5 storm tide by 2100 under this scenario is ~2.4 million if population numbers do not change. In the Houston-Galveston area, elevation increases modestly from the coast resulting in an increase of inundation area with each category storm tide under each RSLR probabilistic scenario (Figure 4-28) rather than the moderate increase in area seen in the Baton Rouge, LA, area (Figure 4-22). Additionally, the results in Figure 4-29 suggest that the Intermediate and Intermediate-High scenarios that are more likely to occur than the extreme, significantly increase the inundation area for category 3 and 5 hurricanes in this region. Total population affected by category and scenario are estimated in Figure 4-30.
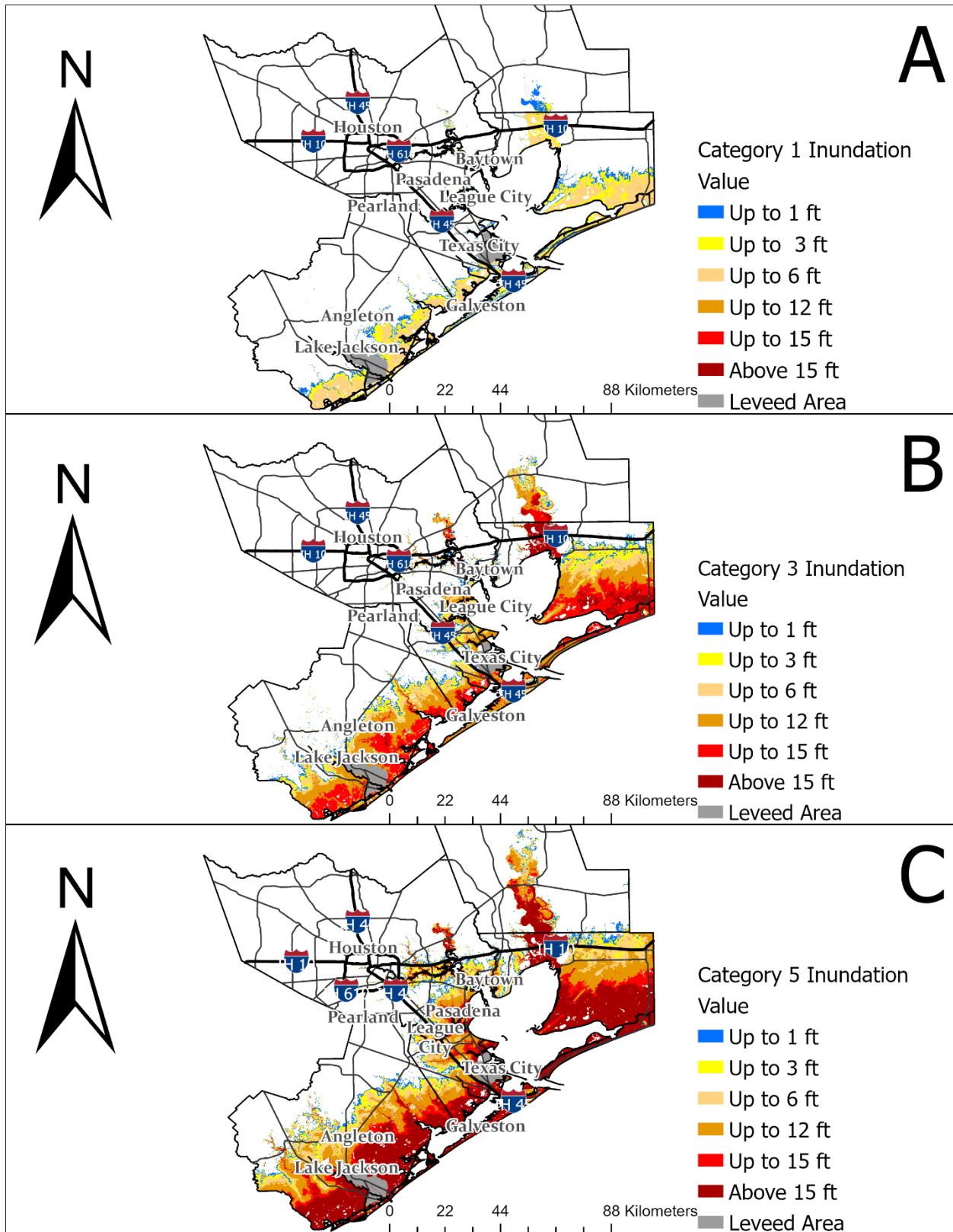
Figure 4- 27. Storm tide inundation map for (a) category 1, (b) category 3, and (c) category 5 hurricane occurring at high tide. Map layers acquired from the National Storm Surge Risk Map Version 3 (NHC).
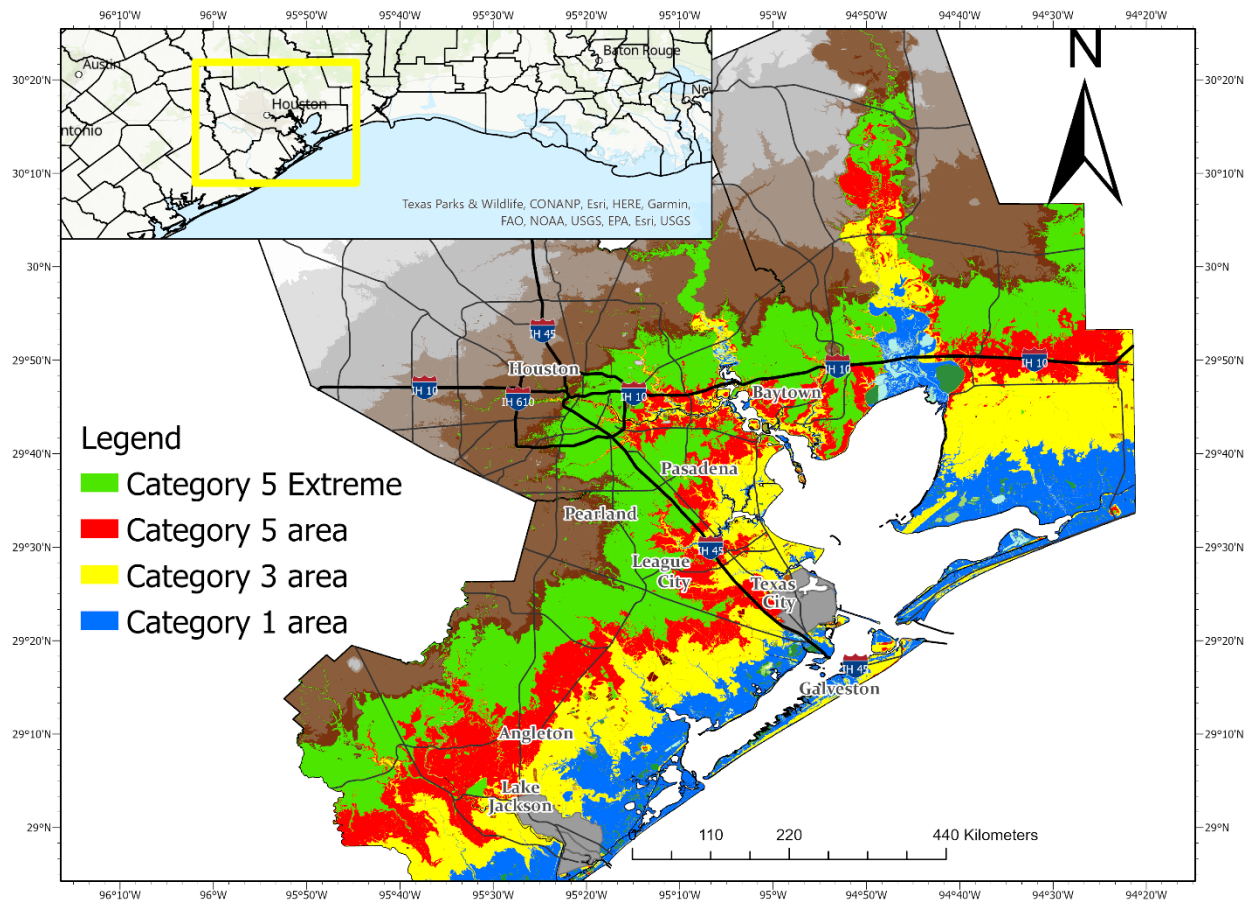
Figure 4- 28. The three categories of storm tide inundation area mapped with the most extreme RSLR hurricane category 5 scenario (bright green), category 5 areal flooding (red), category 3 areal flooding (yellow), category 1 areal flooding (blue), and 10-meter resolution USGS DEM contour shading (brown to light grey). Area of inundation increases significantly with the extreme scenario due to low sloping coastline.
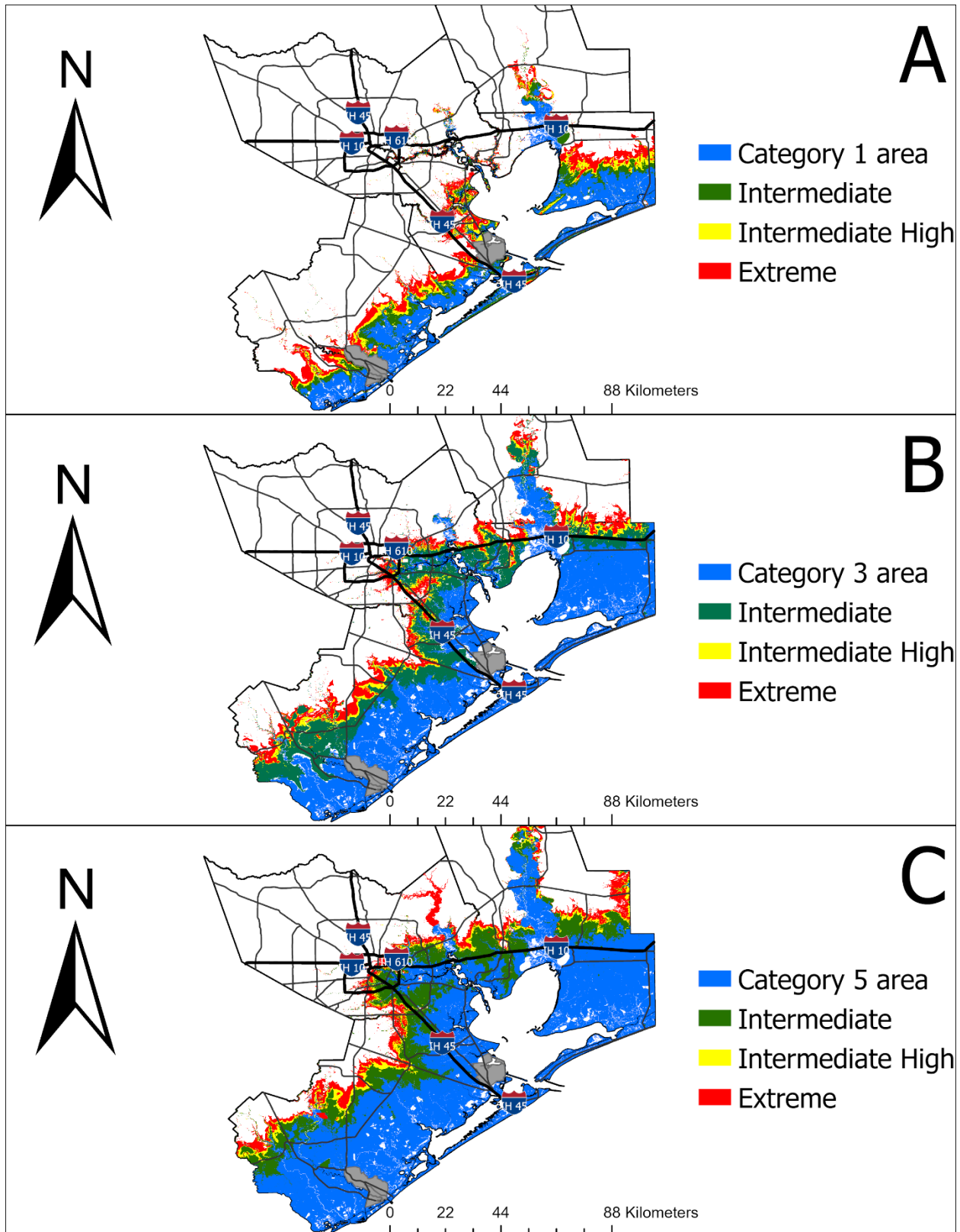
Figure 4- 29. Storm tide inundation map with RSLR projections for a hurricane a) category 1, b) category 3, and c) category 5 occurring at mean high tide (MHHW) plotted with RSLR scenarios estimating the increase in inundation area for each scenario.
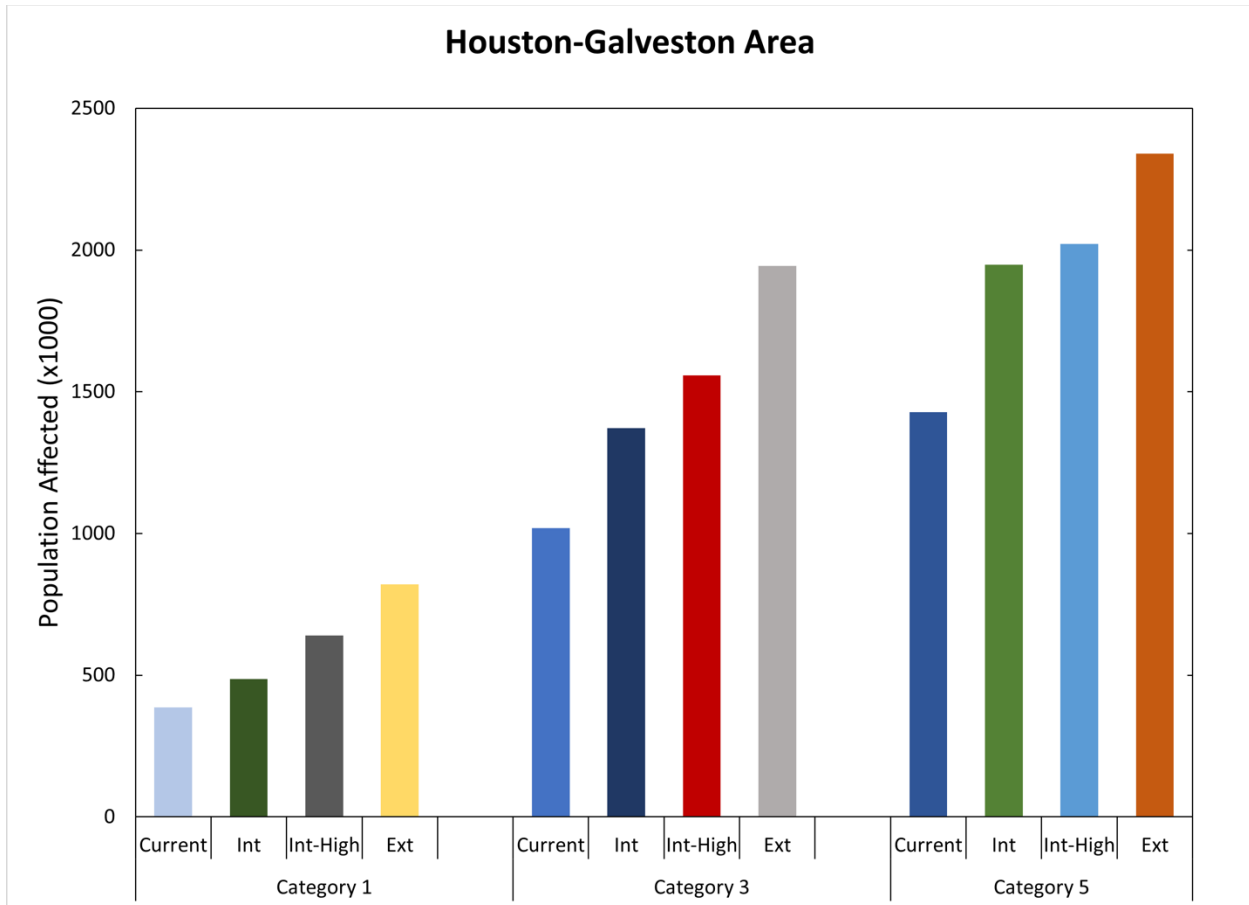
Figure 4- 30. The estimated total population affected by maximum storm tide modeled on category 1, 3, and 5 hurricanes for the case study area (current) plotted with the estimated additional population affected with RSLR scenarios intermediate (Int), intermediate-high, (Int-High), and extreme (Ext). Estimated populations based on SVI 2018 tracts.

Areas of inundation under the extreme RSLR probabilistic scenario for the three categories of storm tides are overlaid with vulnerable populations derived from the SVI in Figure 4-31. The Houston-Galveston area contains many vulnerable tracts as defined in section 4.3.5 including many with multiple variables in the 90th percentile visualized in orange and red colors on the maps. Tracts defined as extremely vulnerable are in the 90th percentile for below poverty, age 65 or older, age 17 or younger, disabilities, mobile homes, and no vehicle as estimated by the SVI (2018). Under the extreme RSLR scenario a category 1 hurricane storm tide affects 30 tracts defined as vulnerable to extremely vulnerable, category 3 affects 73 tracts, and category 5 impacts 94 tracts. U.S. Census tracts are small in densely populated regions, therefore Figure 4-32 details the Houston metropolitan area and Galveston to visualize the number and locations of the vulnerable populations. In Galveston, the most vulnerable tracts are in areas of inundation of 12 to over 15 feet with a storm tide of a hurricane category 5 under recent sea level indicating the need for evacuation during the event. These populations may have a combination of the elderly, the disabled, young people, households with no personal vehicle, and households of modest financial means. Therefore, it is important to identify these tracts and make provisions to aid in the evacuation process.
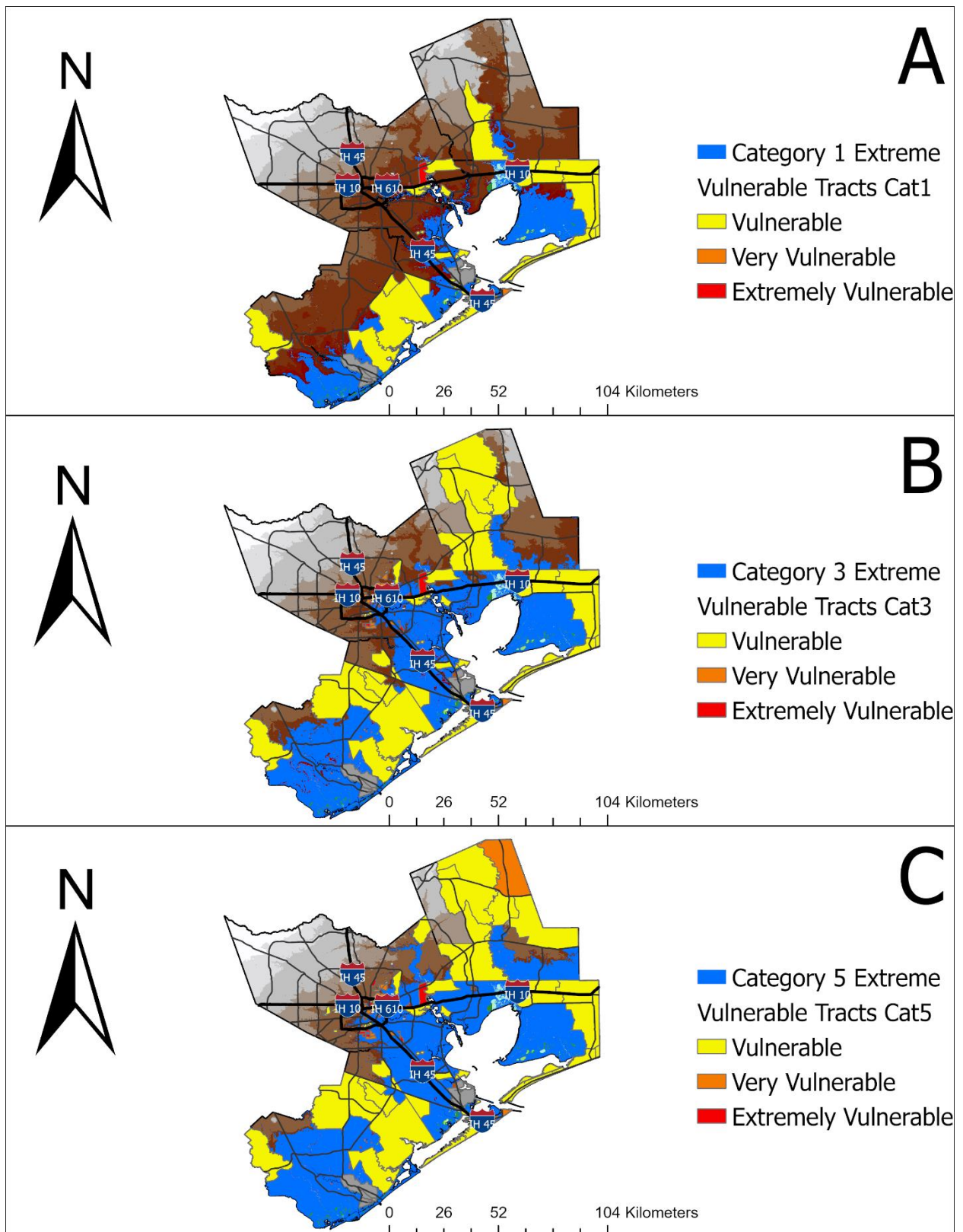
Figure 4- 31. Maps displaying vulnerable tracts based on SVI variables for (a) category 1, (b) category 3, and (c) category 5 hurricane storm tide under the extreme RSLR scenario.

In the Houston area, a large proportion of the most vulnerable tracts are located near the margins of the inundation area under the extreme scenario by 2100 where inundation heights of 1-3 feet (~0.3-1.0 m) would be expected. This suggests action is needed to mitigate flooding in these areas by 2100 to decrease the impacts to the most vulnerable populations and the total population in general.
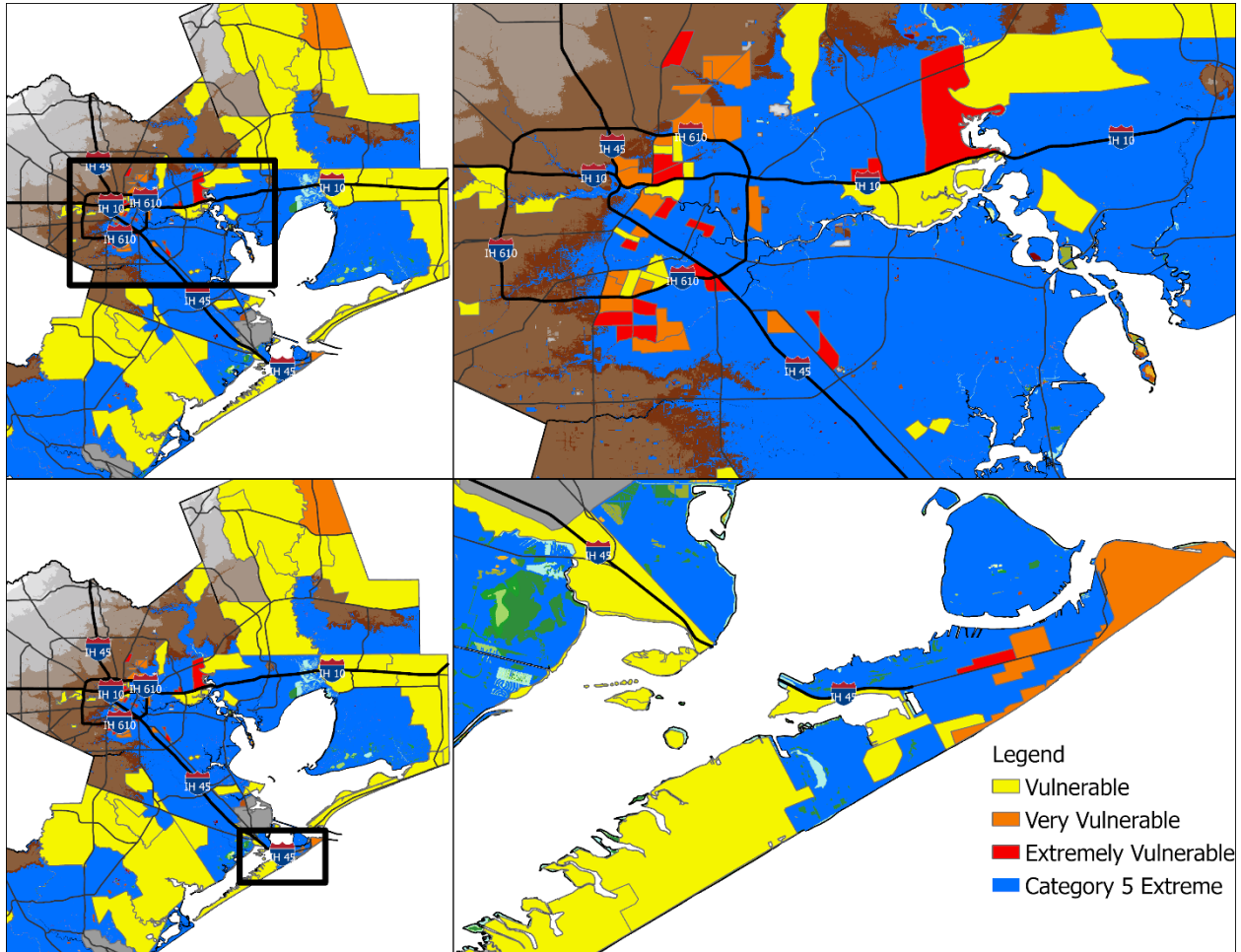
Figure 4- 32. Detailed maps of vulnerable populations affected by a category 5 storm tide under the extreme RSL scenario for Houston (top-right panel) and Galveston (bottom-right panel).

The differences seen in the results of the case studies of the Baton Rouge, LA, area and the Houston/Galveston, TX, area highlight the importance of location-specific analysis as topography plays a significant role in the area and height of inundation from storm tides. While the storm tide layers developed from the SLOSH model cannot be analyzed at the individual parcel level needed, for instance, to develop FEMA flood maps for flood insurance, they are useful on the community/city level for risk assessment and planning. Identifying vulnerable populations by tract at a city or county (parish) scale is the best use of the capabilities of the SLOSH model output.

4.4.7 Summary of Results

The PDFs of annual hourly tide gauge measurements recorded at Galveston, Rockport, and Port Isabel reveal an increasing MSL over the past decades to the present with the upper tails indicative of approaching or exceeding the flood threshold more frequently in modern times. This indication is examined in more detail with the results of daily and hourly HTF at six tide gauge locations with an adequate record. As MSL has increased over the past 40 years, the frequency and duration of HTF events has increased substantially with the greatest increase in locations with higher tidal rages. While these trends are equivalent to those calculated by NOAA using a common impact threshold, using the site-specific flood threshold levels produces more refined HTF days and hours. Spectral analysis results reveal that HTF events in the study area occur seasonally in late-summer to early-fall because of the superimposition of the peak of the seasonal MSL cycle with the peak in NTR resulting from peak hurricane season. This indicates the main influences driving HTF in the study area are RSLR and NTR, with tropical cyclone activity being the main contributor to NTR.

Trend analysis of tropical cyclone activity in the Atlantic basin reveals an increasing trend in tropical storms, hurricanes, and major hurricanes over the historical record. However, no statistically significant trends were found to indicate this increase in activity has led to an increase in landfalls, and therefore surge events, in the Atlantic or the northern GOM. In addition, the Atlantic tropical cyclone activity appears to be positively correlated with warm phases of the AMO. However, correlation between the AMO (and other climate variations) and tropical cyclones making landfall in the western GOM appears to be less obvious. Peak surge history does reveal that 4 of the 8 largest storm tides recorded in the study have occurred since 2005 with Hurricane Katrina recording the highest water levels corresponding to a greater than 100-year surge event.

Accounting for percent changes in storm surge frequency and magnitude from the 1930-1960 baseline, adjusted return periods show that a surge of equal magnitude to Hurricane Katrina would correspond to a 25-50-year surge event if the trends of increasing frequency and magnitude continue. Investigating these trends regarding tropical cyclone activity, the THI results do not show significant trends that indicate an increase in hazards directly from tropical cyclone activity, but they do indicate total THI has been consistently higher in the central to eastern portions of the study area (Sabine Pass east to Grand Isle) over the last 120 years. Considering the changes observed in the peak surge history and lack of strong evidence to prove otherwise, the increase in RSL must be the main contributing factor to the increase in frequency and magnitude of surge events.

While case study results will vary depending on the topography, infrastructure, and existing flood defenses in the chosen area of interest, mapping the addition of RSLR scenarios to storm tides modeled under current sea level provides a method of identifying areas of potentially increased vulnerability over time as the RSL rises. The results for the Baton Rouge, LA, area indicate the greatest increase in inundation area from RSLR and storm tide arises from lower category hurricanes, while major hurricanes represent an increased height of flooding equal to the RSLR of maximum surge and a minimal increase in inundation area due to topographical restraints. Results for the Houston-Galveston area indicate the risk of inland inundation from major hurricanes increases under all RSLR scenarios to include densely populated areas. The topography of the Houston-Galveston area does not restrict inundation area, therefore as RSL rises, the area of inundation increases proportionately. The results of mapping storm surge with vulnerable populations reveal those populations at greatest risk of flooding from storms now and

into the future with increasing RSL. These vulnerable populations will be disproportionally affected by major flooding events and may require more assistance to evacuate prior to the event, making it important to identify these areas and plan actions necessary to evacuate the area, protect the area with flood defenses, or eventually relocate the population.

4.5 Discussion

Trends in frequency and magnitude of tropical cyclone activity are biased by the fact that satellite records of cyclones exist since 1961 while tide gauges have recorded data for up to 100 years and provide a spatially incomplete record. Hence, multidecadal trends in tropical cyclone activity may not be completely captured by the record. Efforts in paleoclimatology have been made to observe tropical cyclone activity in the geologic record dating as far back as 10,000 years, however dating of sedimentary layers remain uncertain due to bioturbation. On the Gulf coast, sediment cores of near-shore freshwater lakes revealed layers of coarse sediment, the most recent of which correspond to known category 4 and 5 storms (Liu and Fearn, 1993). When these storms track over the lakes, ocean water intrudes leaving these coarse sediments behind in episodic layers (Emanuel, 2006). Analysis of cores from four sites along the Northern Gulf coast established that, at these locations, the probability of a landfalling category 4 or 5 hurricane is 0.1% from 5000 to 3800 years ago and during the past 1000 years (Liu, 2007). Additionally, it was determined that from 3800 to 1000 years ago, that probability was 0.5%, suggesting a 2800-year period of much higher major hurricane activity in the area compared to the modern millennium (Liu, 2007). It is hypothesized that this period of increased hurricane activity was due to a southwesterly shift in the location of the Bermuda High resulting in more storms being channeled into the Gulf of Mexico during that time. A longer time series and high-resolution modeling may provide more insights in such a relationship.

Increase in hurricane frequency during La Niña could have influenced more extreme water levels in the GOM over the last 150 years. However, the dominant ENSO phase appears to be out of phase with the Atlantic hurricane season (Kennedy et al., 2007). Analysis of the relationship between ENSO and GOM hurricanes is limited because the number of storms in the record are too few to confirm ENSO-related variability and further study is required to determine what, if any, influence ENSO has on flooding in the study area. It is also worth noting that research suggests ENSO has little influence on HTF events in the region (Sweet et al., 2014), therefore analysis of ENSO in this study is limited to its influence on the number and intensity of Atlantic basin tropical cyclones.

Elevated precipitation and tsunamis may also cause flooding along the Texas and Louisiana coasts. According to the USGS and the National Tsunami Hazard Mitigation Program, tsunamis are rare in the GOM with three small tsunami events recorded by tide gauges over the last 120 years (ten Brink et al., 2009). Tsunami events, triggered by subduction-induced earthquakes, local submarine landslides or disturbances by the Caribbean microplates could be a potential tsunami hazard in the GOM. Submarine landslides can occur due to many factors including rapid soil sediment deposition, weak soil layers, wave loading on bottom sediments by storms, and others, however research indicates earthquakes are the main trigger for a submarine landslide to produce a tsunami (Pampell-Manis et al., 2016). Although resulting submarine landslides are rare and were most active prior to 7000 years ago during a period of large sediment deposition, they are considered a potential flood hazard in the GOM with an estimated return period of 5000-8000 years (Pampell-Manis et al., 2016).

An increase in global surface air temperature due to anthropogenic-induced climate change causes an increase in thermal expansion of seawater of up to 2 m by the year 2100 (Rahmstorf, 2010). Additionally, increased global mean temperature results in an increase of the water-holding capacity of the atmosphere (Trenberth et al., 2003). Globally averaged, the increase in atmospheric water-holding capacity will lead to heavier precipitation when it rains and increases the risk of extreme rainfall, thus increasing the risk of flooding from precipitation events not necessarily associated with tropical cyclones. With the global hydrological cycle being balanced through the conservation of mass, an increase in heavy precipitation events implies a reduction of light/moderate rain events and/or a decrease in the overall frequency of rain events as found by Hennessey et al. (1997). Studies using a coupled atmospheric-ocean general circulation model showed that doubling the atmospheric carbon dioxide in model simulations resulted in a decrease in the frequency of rainfall intensities less than the 85th percentile while heavy precipitation events increased (Allen and Ingram, 2002). Future climate studies suggest that precipitation in Texas may increase by a 7% increase in the 100-year rainfall amount from 1960. This corresponds to an increase of 30% in the frequency of heavy precipitation exceeding the 100-year threshold with projections to 2036 of an additional 6%-10% compared to 1950-1999 (Nielson-Gammon, et al., 2021). According to the study, these changes would equate to a 30%-50% increase in the probability of extreme precipitation in all of Texas compared to 1950-1999 and thus raises the risk of flooding of coastal plains.

4.6 Conclusion

This study demonstrates that an increasing risk of exceeding flood threshold levels resulting in HTF due to the combination of the astronomical tides, RSLR, and storm-related non-tidal residuals in coastal locations of Texas and Louisiana exist. Additionally, this study aimed to establish RSLR as the main driver of increased risk of tropical cyclone-induced storm tide inundation in the study area and to investigate changes in tropical cyclone climatology that lead to an increasing threat of major hurricanes. RSL has increased since 1980, HTF days and cumulative hours above the flood threshold have increased, particularly at locations with higher tidal ranges, with an acceleration in the most recent decade. Spectral analysis of tidal components indicates that threshold exceedance is seasonal, peaking in the height of Atlantic hurricane season, due to the combination of the peak of the seasonal MSL cycle and the storm driven NTR. The results extend the analysis of Sweet et al. (2014) and demonstrate a clear acceleration of HTF by including the most recent data and improve the accuracy in estimations of total HTF days and hours by using site-specific flood threshold levels rather than a common impact threshold (Sweet et al., 2018).

Warm phases of AMO and La Niña events appear to favor tropical storm formation in the Atlantic Ocean but correlation to storm frequency and estimated tidal return periods in the western GOM appears to be more ambiguous. While tropical cyclone activity may be increasing globally, the western GOM is more influenced by RSLR.

A steady increase in RSLR resulting in HTF over the coming decades will be likely more substantial than historic "nuisance" flooding. Flooding events will become more frequent, last longer, and cluster more together. Storm tides that currently represent the greatest flooding risk to life and property, will be higher in magnitude and affect a larger area as RSLR continues. This will be particularly evident as lower category storms that occur more frequently than major hurricanes will produce storm tides enhanced by RSLR with magnitudes like a major hurricane under current sea level conditions.

References

Allen, M. R., and Ingram, W. J. (2002). Constraints on future changes in climate and the hydrologic cycle. *Nature, 419*(6903), 228-232.

Arns, A., Wahl, T., Dangendorf, S., and Jensen, J. (2015). The impact of sea level rise on storm surge water levels in the northern part of the German Bight. *Coastal Engineering*, *96*, 118-131.

Biasutti, M., Sobel, A. H., Camargo, S. J., and Creyts, T. T. (2012). Projected changes in the physical climate of the Gulf Coast and Caribbean. *Climatic change*, *112*(3), 819-845.

Blake E. S., and Zelinsky, D. A. (2018). National Hurricane Center Tropical Cyclone Report: Hurricane Harvey. Publication AL092017. National Hurricane Center, Miami, FL, 3-12.

Booth, B. B., Dunstone, N. J., Halloran, P. R., Andrews, T., and Bellouin, N. (2012). Aerosols implicated as a prime driver of twentieth-century North Atlantic climate variability. *Nature, 484*(7393), 228-232.

Bove, M. C., Elsner, J. B., Landsea, C. W., Niu, X., and O'Brien, J. J. (1998). Effect of El Niño on US landfalling hurricanes, revisited. *Bulletin of the American Meteorological Society, 79*(11), 2477-2482.

Cane, M. A., Clement, A. C., Murphy, L. N., and Bellomo, K. (2017). Low-pass filtering, heat flux, and Atlantic multidecadal variability. *Journal of Climate, 30*(18), 7529-7553.

Chan, J. C., and Shi, J. E. (1996). Long-term trends and interannual variability in tropical cyclone activity over the western North Pacific. *Geophys. Res. Lett., 23*(20), 2765-2767.

Colbert, A. J., and Soden, B. J. (2012). Climatological variations in North Atlantic tropical cyclone tracks. *Journal of climate*, *25*(2), 657-673.

Devlin, A. T., Pan, J., and Lin, H. (2019). Extended spectral analysis of tidal variability in the North Atlantic Ocean. *Journal of Geophysical Research: Oceans*, *124*(1), 506-526.

Elsner, J. B., Bossak, B. H., and Niu, X. F. (2001). Secular changes to the ENSO-US hurricane relationship. *Geophy. Res. Lett., 28*(21), 4123-4126.

Elsner, J. B., Jagger, T. H., and Tsonis, A. A. (2006). Estimated return periods for Hurricane Katrina. *Geophys. Res. Lett.*, *33*(8).

Emanuel, K. (2006). Anthropogenic effects on tropical cyclone activity. *Position Paper, Program in Atmospheres Oceans and Climate: MIT*.

Emanuel, K., Sundararajan, R., and Williams, J. (2008). Hurricanes and global warming: Results from downscaling IPCC AR4 simulations. *Bulletin of the American Meteorological Society*, *89*(3), 347-368.

Emanuel, K. A. (2013). Downscaling CMIP5 climate models shows increased tropical cyclone activity over the 21st century. *Proceedings of the National Academy of Sciences*, *110*(30), 12219-12224.

Goldenberg, S. B., and Shapiro, L. J. (1996). Physical mechanisms for the association of El Niño and West African rainfall with Atlantic major hurricane activity. *Journal of Climate, 9*(6), 1169-1187.

Goldenberg, S. B., Landsea, C. W., Mestas-Nuñez, A. M., and Gray, W. M. (2001). The recent increase in Atlantic hurricane activity: Causes and implications. *Science, 293*(5529), 474-479.

Gray, W. M. (1984). Atlantic seasonal hurricane frequency. Part I: El Niño and 30 mb quasi-biennial oscillation influences. *Monthly weather review, 112*(9), 1649-1668.

Harris, D. L. (1963). *Characteristics of the hurricane storm surge* (No. 48). Department of Commerce, Weather Bureau, 1-19.

Hartmann, D. L., Tank, A. M. K., Rusticucci, M., Alexander, L. V., Brönnimann, S., Charabi, Y. A. R., Dentener, F. J., Dlugokencky, E. J., Easterling, D. R., Kaplan, A., Soden, B. J., Thorne, P. W., Wild, M., and Zhai, P. (2013). Observations: atmosphere and surface. *In Climate change 2013 the physical science basis: Working group I contribution to the fifth assessment report of the intergovernmental panel on climate change* (pp. 159-254). Cambridge University Press.

Hassanzadeh, P., Lee, C. Y., Nabizadeh, E., Camargo, S. J., Ma, D., and Yeung, L. Y. (2020). Effects of climate change on the movement of future landfalling Texas tropical cyclones. *Nature communications*, *11*(1), 1-9.

Hennessy, K. J., Gregory, J. M., and Mitchell, J. F. B. (1997). Changes in daily precipitation under enhanced greenhouse conditions. *Climate Dynamics, 13*(9), 667-680.

Huff, F. A., and Angel, J. R. (1992). Rainfall frequency atlas of the Midwest. *Bulletin (Illinois State Water Survey) no. 71*.

Keim, B. D., Muller, R. A., and Stone, G. W. (2007). Spatiotemporal patterns and return periods of tropical storm and hurricane strikes from Texas to Maine. *Journal of climate*, *20*(14), 3498-3509.

Kennedy, A. J., Griffin, M. L., Morey, S. L., Smith, S. R., and O'Brien, J. J. (2007). Effects of El Niño–Southern Oscillation on sea level anomalies along the Gulf of Mexico coast. *Journal of Geophysical Research: Oceans*, *112*(C5).

Knutson, T., Camargo, S. J., Chan, J. C., Emanuel, K., Ho, C. H., Kossin, J., Mohapatra, M., Satoh, M., Sugi, M., Walsh, K., and Wu, L. (2020). Tropical cyclones and climate change assessment: Part II: Projected response to anthropogenic warming. *Bulletin of the American Meteorological Society*, *101*(3), E303-E322.

Kossin, J. P. (2018). A global slowdown of tropical-cyclone translation speed. *Nature*, *558*(7708), 104-107.

Landsea, C. W. (1993). A climatology of intense (or major) Atlantic hurricanes. *Monthly weather review, 121*(6), 1703-1713.

Liu, K. B., and Fearn, M. L. (1993). Lake-sediment record of late Holocene hurricane activities from coastal Alabama. *Geology*, *21*(9), 793-796.

Liu, K. B. (2007). Uncovering Prehistoric Hurricane Activity: Examination of the geological record reveals some surprising long-term trends. *American Scientist*, *95*(2), 126-133.

Mann, M. E., and Emanuel, K. A. (2006). Atlantic hurricane trends linked to climate change. *Eos, Transactions American Geophysical Union, 87*(24), 233-241.

Mann, M. E., Steinman, B. A., Brouillette, D. J., and Miller, S. K. (2021). Multidecadal climate oscillations during the past millennium driven by volcanic forcing. *Science*, *371*(6533), 1014-1019.

Moore, G. W. K., Halfar, J., Majeed, H., Adey, W., and Kronz, A. (2017). Amplification of the Atlantic Multidecadal Oscillation associated with the onset of the industrial-era warming. *Scientific Reports, 7*(1), 1-10.

Needham, H. (2010). Identifying historic storm surges and calculating storm surge return periods for the Gulf of Mexico coast.

Needham, H. F., & Keim, B. D. (2012). A storm surge database for the US Gulf Coast. *International Journal of Climatology, 32*(14), 2108-2123.

Needham, H. F. (2014). A Data-Driven Storm Surge Analysis for the US Gulf Coast.

Nielsen-Gammon, J., Escobedo, J., Ott, C., Dedrick, J., and Van Fleet, A. (2020). *Assessment of historic and future trends of extreme weather in Texas, 1900-2036*.

Neumann, C. J. (1987). The national hurricane center risk analysis program (HURISK). NOAA Tech. Mem. NWS NHC 38. National Hurricane Center, Coral Gables, FL. 56 pp.

Pampell-Manis, A., Horrillo, J., Shigihara, Y., and Parambath, L. (2016). Probabilistic assessment of landslide tsunami hazard for the northern Gulf of Mexico. *Journal of Geophysical Research: Oceans*, *121*(1), 1009-1027.

Pielke Jr, R. A., and Landsea, C. N. (1999). La Nina, El Nino, and Atlantic hurricane damages in the United States. *Bulletin of the American Meteorological Society, 80*(10), 2027-2034.

Rahmstorf, S. (2010). A new view on sea level rise. *Nature Climate Change, 1*(1004), 44-45.

Ray, R. D., Loomis, B. D., and Zlotnicki, V. (2021). The mean seasonal cycle in relative sea level from satellite altimetry and gravimetry. *Journal of Geodesy, 95*(7), 1-21.

Saunders, M. A., and Lea, A. S. (2008). Large contribution of sea surface warming to recent increase in Atlantic hurricane activity. *Nature, 451*(7178), 557-560.

Scherer, W., Stoney, W. M., Mero, T. N., O′ Hargan, M., Gibson, W. M., Hubbard, J. R., Weiss, M. I., Varmer, O., Via, B., Frilot, D. M., and Tronvig, K. A. (2001). Tidal Datums and Their Applications. NOAA Special Publication, CO-OPS 1. National Oceanic and Atmospheric Administration, National Ocean Service, Silver Spring, MD 112 pp.

Schlesinger, M. E., and Ramankutty, N. (1994). An oscillation in the global climate system of period 65–70 years. *Nature, 367*(6465), 723-726.

Smith, J. M., Cialone, M. A., Wamsley, T. V., and McAlpin, T. O. (2010). Potential impact of sea level rise on coastal surges in southeast Louisiana. *Ocean Engineering*, *37*(1), 37-47.

Sweet, W., Park, J., Marra, J., Zervas, C., and Gill, S. (2014). Sea level rise and nuisance flood frequency changes around the United States. NOAA Tech. Rep. NOS CO-OPS 073. National Oceanic and Atmospheric Administration, National Ocean Service, Silver Spring, MD. 58 pp.

Sweet, W. V., and Park, J. (2014). From the extreme to the mean: Acceleration and tipping points of coastal inundation from sea level rise. *Earth's Future, 2*(12), 579-600.

Sweet, W. V., Dusek, G., Obeysekera, J. B., and Marra, J. J. (2018). Patterns and projections of high tide flooding along the US coastline using a common impact threshold. NOAA Tech. Rep. NOS CO-OPS 086. National   Oceanic and Atmospheric Administration, National Ocean Service, Silver Spring, MD. 44 pp.

Ten Brink, U., Twichell, D., Lynett, P., Geist, E., Chaytor, J., Lee, H., Buczkowski, B., and Flores, C. (2009). Regional assessment of tsunami potential in the Gulf of Mexico, US Geological Survey Administrative Report.

Thompson, P. R., Widlansky, M. J., Hamlington, B. D., Merrifield, M. A., Marra, J. J., Mitchum, G. T., and Sweet, W. (2021). Rapid increases and extreme months in projections of United States high-tide flooding. *Nature Climate Change, 11*(7), 584-590.

Trenberth, K. E., Dai, A., Rasmussen, R. M., and Parsons, D. B. (2003). The changing character of precipitation. *Bulletin of the American Meteorological Society*, *84*(9), 1205-1218.

Wahl, T. (2017). Sea-level rise and storm surges, relationship status: complicated!. *Environmental Research Letters, 12*(11).

Wallace, J. M., and Hobbs, P. V. (2006). *Atmospheric science: an introductory survey* (Vol. 92). Elsevier, 366-370.

Wang, S., and Toumi, R. (2021). Recent migration of tropical cyclones toward coasts. *Science, 371*(6528), 514-517.

Yamaguchi, M., Chan, J. C., Moon, I. J., Yoshida, K., and Mizuta, R. (2020). Global warming changes tropical cyclone translation speed. *Nature communications*, *11*(1), 1-7.

Zachry, B. C., Booth, W. J., Rhome, J. R., and Sharon, T. M. (2015). A national view of storm surge risk and inundation. *Weather, climate, and society*, *7*(2), 109-117.

Zervas, C. E. (2009). Sea level variations of the United States, 1854-2006. NOAA Tech. Rep. NOS CO-OPS 053. National Oceanic and Atmospheric Administration, National Ocean Service, Silver Spring, MD. 76 pp.

Chapter 5: Concluding Remarks and Future Perspective

5.1 Summary and Conclusion

This dissertation addressed the hypothesis that sea level rise is increasing the frequency, magnitude, and duration of coastal flooding events in Texas and Louisiana representing an increasing risk to currently vulnerable locations and a future risk expanding to areas not historically affected. This was achieved through analysis of historical observations of water levels and tropical cyclones with associated storm surges, as well as storm surge model output and future projections of relative sea level rise and trends in tropical cyclone climatology.

Water levels recorded by tide gauges since the early 20th century were utilized to quantify the rate of relative sea level rise, the number and duration of high tide flooding events from 1980-2019, the evolution of mean sea level and the probability of flood threshold exceedance. Spectral analysis of hourly tide gauge data was employed to examine the tidal components that contribute to water levels above flood thresholds. Records of tropical cyclone activity, landfalls, and peak surge were updated with verified data to 2020 and used to detect trends in the record, examine correlations with climate oscillations, estimate peak surge return periods, and calculate the tropical hazard index. The National Weather Service's SLOSH model provided maximum envelopes of water that were utilized to produce storm tide inundation maps to identify areas susceptible to flooding due to storm tides produced by varying categories of hurricanes. A seasonal autoregressive integrated moving average (SARIMA) model was applied to forecast relative sea level and results were compared to probabilistic projections based on published literature to determine what method of forecasting provides results most useful in risk assessment. Projections of relative sea level rise under six RCP-based scenarios from 2000 to 2100 were used to develop inundation maps used to identify areas at future risk from flooding due to high tide as well as sea level-enhanced storm tides.

This study assessed the flood vulnerability risk for Harris County, Texas, and reviewed recent papers that addressed sea level rise, storm surge, and extreme precipitation to better understand the mechanisms of flooding. This assessment identified US Census block groups that are vulnerable to flooding by extreme precipitation using the 100- and 500-year FEMA floodplains and storm tide enhanced by the maximum projected global mean sea level rise scenario of ~2.5 meters by 2100 based on published literature. Additionally, the study utilized transit data and U.S. Census demographics to identify transit-dependent populations vulnerable to flooding with the objective of improving evacuation procedures that led to poor outcomes during Hurricane Harvey in 2017.

Planners and policymakers at the state, city, and community level require location-specific sea level projections over varying time periods (e.g., over the coming 30 years) to analyze risk and assess flood defense infrastructure. To address these needs, this study evaluated relative sea level rise and methods of forecasting that could provide a range of localized temporal projections to better constrain the risk of coastal flooding in the western GOM. Relative sea level rise based on monthly mean sea levels recorded at tide gauge stations was found to be rising faster than the global average rate (~3.0 mm/yr) due to subsidence. Thus, relative sea level rise projections were required to provide location-specific rates. While SARIMA modeling was able to provide 5- and 10-year forecasts of relative sea level that captured the seasonality and linear trend of the observations within a 95% confidence interval, it did not project possible acceleration and uncertainty in the model was highly dependent on the length and consistency of the tige gauge time series. Probabilistic projections based on global climate model projections imposed on a

background subsidence rate did include acceleration scenarios, but multiple scenarios needed to be included to account for various contributors to uncertainty. The probabilistic projections were used to map relative sea level rise mean high tide inundation risk to infrastructure under three RCP-based scenarios over 20-year increments to 2100. This method was determined to be most useful for planners and policymakers as it incorporated local relative sea level rise rates with multiple acceleration scenarios that can be applied over time and space as exemplified by the cases studies of New Orleans, LA, and Galveston, TX.

To account for all possible coastal flood risks, the final chapter of this study examined hourly tide gauge data for flood threshold exceedance from 1980-2019 and determined the various factors contributing to said exceedances. Spectral analysis of astronomical tides, seasonal sea level cycles, and non-tidal residuals revealed that relative sea level rise is contributing to an increase in frequency and duration of high tide flooding events. Additionally, flood threshold exceedances occurred due to non-tidal residuals associated with the peak of tropical cyclone activity and the seasonal mean sea level cycle in September. Thus, trends in tropical cyclone activity and associated storm surge were examined to determine if changes in tropical cyclone climatology and associated climate oscillations represent an additional increasing risk to coastal Texas and Louisiana.

The Mann-Kendall trend test detected a statistically significant increasing trend in frequency of Atlantic basin tropical storms, hurricanes, and major hurricanes. However, correlation between the Atlantic Multidecadal Oscillation or La Niña events and frequency of tropical storms that made landfall in western GOM was more ambiguous. Estimated peak surge return periods based on 30-year averages from 1900-2020 suggest an increase in frequency and magnitude of storm surge/tide resulting in an increase to the 100-year peak surge of ~2.5 meters. However, calculation of the Tropical Hazard Index for specific locations within the study area over 40-year periods from 1901-2020 revealed no spaciotemporal patterns for major hurricane strikes nor did it indicate any reliable trends or patterns to confirm the potential change in surge risk. Thus, relative sea level rise appears to be the main increasing risk for coastal inundation in Texas and Louisiana. Case studies were conducted in which relative sea level rise scenarios based on probabilistic projections were added to modeled storm surge under current conditions to examine the changing inundation risk by 2100 in the Baton Rouge, LA, and Houston-Galveston, TX, areas.

In conclusion, the work presented herein enhances the understanding of the various flood mechanisms that represent a future risk of coastal flooding in Texas and Louisiana. With this enhanced understanding comes the capability to improve upon risk assessment methods to include the combined natural and anthropogenic induced sea level extremes for the future. Thus, coastal adaptation and resilience measures can be developed for vulnerable areas and planners and policy makers can modify emergency response procedures appropriately. While this dissertation focused specifically on Texas and Louisiana due to high rates of relative sea level rise, the methods presented herein can be applied to any coastal region for which appropriate data is available.

5.2 Future Perspective

As the understanding of the mechanisms causing sea level rise improves, new projection scenarios emerge such as those released by the IPCC sixth assessment report (AR6) in 2021 based on CMIP6 climate models that include improved ice sheet modeling. In addition to new global scenarios, methods of analyzing future extreme sea levels are being improved, for

example, to include a wave setup/run-up component (Arns et al., 2017; Vousdoukas et al., 2018). These periodic updates require risk assessments and associated adaptation strategies be regularly scrutinized and, if needed, updated to integrate new scenarios and/or methods. The publication of new results and methods, however, should not nullify previous assessments. Future assessments should include a high-end scenario associated with low probability and high risk, and monitoring to know if observations begin to deviate from the projections (Hinkel et al., 2019; Ranger et al., 2013). Ideally, new projections would be included in a monitoring plan and only when new information suggests a major change should adaptation strategies be reassessed. However, this requires knowledge of how much sea level rise scenarios would have to change to invalidate previous assessments. This topic needs to be explored further to include a methodology for integrating new sea level knowledge beyond simply suggesting flexibility in adaptation measures (Nicholls et al., 2021). The research presented in this dissertation can be extended to consider such a methodology. One can propose that when a new scenario's median value exceeds the uncertainty bounds of the previous scenario, adapting the assessment should be considered. However, further statistical analysis is required to propose a more thorough methodology.

This study utilized a combination of the data from the National Weather Service including sea, lake, and overland surges from hurricanes (SLOSH) model of simulated storms and relative sea level rise projections (linearly added to the model output) to explore future risk of coastal inundation. SLOSH is a two-dimensional storm surge prediction model differed from the shallow water equations with a structured mesh grid. Additionally, SLOSH does not predict waves that are superimposed on the storm tide. Although SLOSH is used commonly to model storm surge due to its highly efficient computational cost and has adequately predicted the costal inundation (Lin et al., 2012), three -dimensional ocean general circulation models (OGCM) on the basis of the full Navier Stokes Equations may be a more adequate to predict coastal flooding under a changing climate. An example is the Advanced Circulation (ADCIRC) model, developed at the University of North Carolina, that has been applied to develop FEMA flood insurance rate maps in coastal regions and to simulate tropical storms, equivalent to the magnitude of Hurricane Katrina, to construct a more hurricane-resistant levee system for the city of New Orleans, LA. ADCIRC uses a time dependent, variable (unstructured), mesh grid which provides higher resolution along the coast (including high-resolution bathymetry) and is often coupled with the simulating waves nearshore (SWAN) model to predict the combined effect of waves and storm tides (Dietrich et al., 2011; Sebastian et al., 2014). ADCIRC has also successfully been coupled with high resolution (<5 m) urban inundation models to accurately model the extent and depth of flooding from storm surge (Yin et al., 2016). Additionally, mean sea level can be adjusted to add RSLR projections directly into the model (Smith et al., 2010). The application of ADCIRC to the study presented herein may improve the accuracy of the inundation mapping results by (1) allowing for non-linear effects of RSLR projections, (2) increasing the coastal resolution, (3) including the effects of waves, and (4) allowing for coupling with high resolution urban inundation models. One could suggest that an improved inundation forecast for highly complex urban areas, such as Harris County, TX, can be achieved if an OGCM like ADCIRC is applied. Note that storm surges are often accompanied by extreme rainfall that can have compounding effects on flooding. One could propose the use of an Earth System Model, like Community Earth System Model (CESM3), with similar features of ADCIRC and SWAN and flood-dependent varying runoff to predict more reliable coastal flooding. CESM3, run at high-resolution, and incorporating features of the Weather Research and Forecasting Model (WRF), can simulate regional sea level, coastal flooding, and hurricane forecasts. Similarly, the newly developed

Regional Community Earth System Model (R-CESM) includes the Regional Ocean Modeling System (ROMS) as an additional ocean component while incorporating WRF for the atmosphere and can be used for both global and regional modeling (Fu et al., 2021).

References

Arns, A., Dangendorf, S., Jensen, J., Talke, S., Bender, J., and Pattiaratchi, C. (2017). Sea-level rise induced amplification of coastal protection design heights. *Scientific reports, 7*(1), 1-9.

Dietrich, J. C., Zijlema, M., Westerink, J. J., Holthuijsen, L. H., Dawson, C., Luettich Jr, R. A., Jenson, R. E., Smith, J. M., Stelling, G. S., and Stone, G. W. (2011). Modeling hurricane waves and storm surge using integrally-coupled, scalable computations. *Coastal Engineering, 58*(1), 45-65.

Fu, D., Small, J., Kurian, J., Liu, Y., Kauffman, B., Gopal, A., Ramachandran, S., Shang, Z., Chang, P., Danabasoglu, G., Thayer-Calder, K., Vertenstein, M., Ma, X., Yao, H., Li, M., Xu, Z., Lin, X., Zhang, S., and Wu, L. (2021). Introducing the New Regional Community Earth System Model, R-CESM. *Bulletin of the American Meteorological Society, 102*(9), E1821-E1843.

Hinkel, J., Church, J. A., Gregory, J. M., Lambert, E., Le Cozannet, G., Lowe, J., McInnes, K. L., Nicholls, R. J., van der Pol, T. D., and van de Wal, R. (2019). Meeting user needs for sea level rise information: a decision analysis perspective. *Earth's Future, 7*(3), 320-337.

Lin, N., Emanuel, K., Oppenheimer, M., and Vanmarcke, E. (2012). Physically based assessment of hurricane surge threat under climate change. *Nature Climate Change, 2*(6), 462-467.

Nicholls, R. J., Hanson, S. E., Lowe, J. A., Slangen, A. B., Wahl, T., Hinkel, J., and Long, A. J. (2021). Integrating new sea-level scenarios into coastal risk and adaptation assessments: An ongoing process. Wiley Interdisciplinary Reviews: *Climate Change, 12*(3), e706.

Ranger, N., Reeder, T., and Lowe, J. (2013). Addressing 'deep' uncertainty over long-term climate in major infrastructure projects: four innovations of the Thames Estuary 2100 Project. *EURO Journal on Decision Processes*, *1*(3-4), 233-262.

Sebastian, A., Proft, J., Dietrich, J. C., Du, W., Bedient, P. B., and Dawson, C. N. (2014). Characterizing hurricane storm surge behavior in Galveston Bay using the SWAN+ ADCIRC model. *Coastal Engineering, 88*, 171-181.

Smith, J. M., Cialone, M. A., Wamsley, T. V., and McAlpin, T. O. (2010). Potential impact of sea level rise on coastal surges in southeast Louisiana. *Ocean Engineering*, *37*(1), 37-47.

Vousdoukas, M. I., Mentaschi, L., Voukouvalas, E., Verlaan, M., Jevrejeva, S., Jackson, L. P., and Feyen, L. (2018). Global probabilistic projections of extreme sea levels show intensification of coastal flood hazard. *Nature communications, 9*(1), 1-12.

Yin, J., Lin, N., and Yu, D. (2016). Coupled modeling of storm surge and coastal inundation: A case study in New York City during Hurricane Sandy. *Water Resources Research, 52*(11), 8685-8699.